A Statistical Approach to Quantifying Impact of Multiple Pulse Resistance Spot Welding Schedules on Liquid Metal Embrittlement Cracking

by

Erica Wintjes

A thesis
presented to the University of Waterloo
in fulfillment of the
thesis requirement for the degree of
Master of Applied Science
in
Mechanical Engineering

Waterloo, Ontario, Canada, 2019

AUTHOR'S DECLARATION

This thesis consists of material all of which I authored or co-authored: see Statement of Contributions included in the thesis. This is a true copy of the thesis, including any required final revisions, as accepted by my examiners.

I understand that my thesis may be made electronically available to the public.

Statement of Contributions

This thesis was solely written by the candidate. Professors N. Zhou and E. Biro contributed to editing the entire thesis and the papers which form the basis of Chapters 4 and 5. Additional contributions were made in some areas by other members of the Center for Advanced Materials Joining research group. Specific contributions to this work, other than those already noted, are listed below.

Chapter 4 of this thesis is based on the results from a conference paper:

> E. Wintjes, A. Macwan, E. Biro, Y. Zhou, "Effect of Multi-Pulse Welding on LME Severity in RSW Joints." Sheet Metal Welding Conference XVII, 2018.

The experimental design, analysis, and writing were conducted by the candidate. The paper was also co-authored by Prof. E. Biro, Prof. N. Zhou, and Dr. A. Macwan from ArcelorMittal Dofasco, who contributed through technical discussions of the results and assisted with editing the manuscript.

Chapter 5 of this thesis is based on a journal paper which has been published in *Welding in the World*:

> E. Wintjes, C. DiGiovanni, L. He, E. Biro, Y. Zhou, "Quantifying the Link Between Crack Distribution and Resistance Spot Weld Strength Reduction in Liquid Metal Embrittlement Susceptible Steels." Welding in the World, 2019.

The experimental design, analysis, and writing were again conducted solely by the candidate. The paper was co-authored by the candidate, Mr. C. DiGiovanni, Mr. L. He, Prof. E. Biro and Prof. N. Zhou. Mr. DiGiovanni and Mr. He each provided several data points (tensile testing data and cracking distribution), which were used to demonstrate the relationship between liquid metal embrittlement cracking and weld strength loss. Mr. DiGiovanni also helped develop the methodology. Prof. Biro and Prof. Zhou again participated in technical discussions and editing the manuscript.

Section 6.1.2 also contains co-authored content. The thermo-mechanical model, which was used to investigate the temperatures and stresses in the weld, was developed by Mr. C. DiGiovanni. Mr. DiGiovanni performed the modelling using the parameters specified by the candidate. The model output was analyzed by the candidate. Mr. L. He operated the SEM for elemental analysis. The SEM generated data was processed and analyzed by the candidate.

Abstract

Advanced high strength steels (AHSS) are advantageous for automotive applications due to their excellent strength and ductility. However, when coated with zinc for corrosion protection, these steels are susceptible to liquid metal embrittlement (LME) during welding. In this work, a new metric was developed to quantify LME severity and this metric was used to study the influence of multiple pulse weld schedules on LME cracking in resistance spot welds.

Several conflicting reports have been released about the effect of LME on mechanical performance of resistance spot welds. In this work, a new method of LME crack quantification called a "Crack Index" was developed to link LME crack distributions in resistance spot welds to weld performance. The crack index is calculated by multiplying the lognormal median crack length by the number of cracks per weld and dividing by the sheet thickness. Because studies have established both crack size and location as vital factors affecting weld strength, both of these factors must be taken into account when characterizing LME severity. Lognormal median crack length is used as the parameter for crack size because the crack lengths measured in LME affected welds were observed to fit a lognormal distribution. Number of cracks is used to account for the probability that a crack may be found in a critical location and sheet thickness is used as a normalization factor. The crack index has a linear relationship with weld strength loss.

The crack index analysis method was used to study the influence of multiple pulse welding schedules on LME severity. Pulsing was applied using two different methodologies: pulsing during the welding current to manage heat generation and a pre-pulse before the welding current to remove the zinc coating. All welds made using a double-pulse welding schedule exhibited less severe LME cracking than those made with a single pulse schedule with a similar nugget diameter. A double-pulse schedule with two equal length pulses showed the least severe LME cracking and a schedule consisting of a short pulse followed by a long pulse resulted in the most severe LME. This is due to both a difference in the amount of free zinc available for LME and the different thermal and stress profiles of the pulsing conditions. The majority of pre-pulse welding schedules caused an increase in LME cracking due to the additional heat introduced into the weld. However, a 4 kA pre-pulse (low current), applied for 3 cy (low time) was able to reduce LME cracking in TRIP1100, a LME crack susceptible alloy, by almost 30%. The 4 kA, 3 cy pre-pulse reduced the amount of free zinc for LME, without introducing too much additional heat into the weld.

Acknowledgements

I would first like to thank my supervisors, Prof. Norman Zhou and Prof. Elliot Biro, for all of the time, knowledge, and advice they have shared with me over the past two years.

Secondly, I would like to express my gratitude to the industry collaborators for this project, specifically Dr. Andrew Macwan from ArcelorMittal Dofasco and Dr. Frank Goodwin from the International Zinc Association. This research would not have been possible without their support.

I would also like to thank Mr. Mark Griffett for his time and assistance in gathering the tensile testing data that became the basis of Chapter 5 of this thesis.

I also wish to acknowledge my colleagues in the CAMJ research group, especially Chris DiGiovanni, Xu Han, James Choi, and Josh He. Thank you for the many hours of discussion about unexpected results, help in the lab, and all the lunchtime debates.

Finally, I would like to thank my friends and family for all of their support and encouragement over the past two years. I couldn't have done it without you.

Table of Contents

AUTHOR'S DECLARATION ii
Statement of Contributions iii
Abstract iv
Acknowledgements v
Table of Contents vi
List of Figures ix
List of Tables xii
List of Abbreviations xiii
List of Symbols xiv
Chapter 1 Introduction 1
1.1 Background 1
1.2 Objectives 2
1.3 Criteria and Constraints 2
1.4 Thesis Outline 2
Chapter 2 Literature Review 4
2.1 Advanced High Strength Steel (AHSS) 4
2.1.1 Dual Phase (DP) Steel 5
2.1.2 Transformation Induced Plasticity (TRIP) Steel 6
2.2 Zinc Coatings 7
2.2.1 Hot-Dip Galvanization 7
2.2.2 Electrogalvanization 7
2.3 Resistance Spot Welding (RSW) 7
2.3.1 RSW Fundamentals 8
2.3.2 Welding Parameters 11
2.4 Liquid Metal Embrittlement (LME) 13
2.4.1 Effect of Temperature 13
2.4.2 Effect of Strain Rate 15
2.4.3 Effect of Composition of Liquid Metal 15
2.4.4 Effect of Solid Metal Microstructure 17
2.4.5 Possible Mechanisms 17
2.5 LME in RSW of AHSS 18

2.5.1 Characteristics of LME Cracking in Resistance Spot Welds 19
2.5.2 Effect of Welding Parameters on LME 20
2.5.3 Effect of LME on Weld Mechanical Performance 21
2.5.4 Quantifying LME Severity 21
2.5.5 Methods for LME Reduction in RSW 22
Chapter 3 Methodology 24
3.1 Materials 24
3.2 Welding 25
3.2.1 Pulsed Welding Schedules 27
3.2.2 Pre-pulse Welding Schedules 28
3.3 Crack Analysis 29
3.4 Tensile Testing 30
3.5 Nugget Diameter Measurements 31
3.6 Statistical Analysis 32
3.6.1 Error Calculations 32
3.6.2 Significance Testing 33
3.6.3 Linear Regression Analysis 34
Chapter 4 Effect of Multiple Pulse Weld Schedules on LME Severity 35
4.1 Effect of Pulsed Welding Schedules 35
4.1.1 Single vs. Double Pulse Welds 35
4.1.2 Effect of Changing Pulse Lengths 39
4.2 Effect of Pre-Pulse Welding Schedules 43
4.2.1 Effect of Pre-Pulse on LME Cracking 43
4.3 Summary and Further Work 48
Chapter 5 LME Quantification and Relationship with Weld Performance 49
5.1 Crack Analysis 49
5.2 Tensile Lap Shear Testing 52
5.3 Crack Population Distributions 55
5.4 Crack Index 57
5.5 Alternative Crack Indices 58
5.5.1 Crack Index with Normal Median 58
5.5.2 Crack Index with Different Percentile Crack Lengths 59

5.6 Summary and Further Work 62
Chapter 6 Applying the Crack Index to Analyze Impact of Multiple Pulse Welding Schedules on LME Severity 63
6.1 Effect of Pulsed Welding Schedules 63
6.1.1 Single vs. Double Pulse Welds 63
6.1.2 Effect of Changing Pulse Lengths 64
6.2 Effect of Pre-Pulse Welding Schedules 72
6.3 Summary 76
Chapter 7 Conclusions and Recommendations 77
7.1 LME Quantification and Relationship to Weld Performance 77
7.2 Effect of Multiple Pulse Welding Schedules on LME Severity 77
7.3 Recommended Future Work 78
References 80
Appendix A MATLAB Implementation of the Bootstrap Method for Calculating Standard Deviation of 95^{th} Percentile Crack Length 89
Appendix B ANOVA Tables for Linear Regression Analysis 90

List of Figures

Figure 2.1 Steel strength-ductility diagram illustrating the range of properties available from AHSS [20]. 4
Figure 2.2 Two distinct regions of the automotive structure [21]. 5
Figure 2.3 Schematic of DP steel microstructure [20]. 6
Figure 2.4 Schematic of TRIP steel microstructure [20]. 6
Figure 2.5 Steps of the resistance spot welding process. 8
Figure 2.6 Schematic of the resistances present in RSW [30]. 9
Figure 2.7 Theoretical dynamic resistance during RSW. 10
Figure 2.8 Weld lob curve for RSW [28]. 12
Figure 2.9 Stress-strain curves for Fe22Mn0.6C steel at a) 600°C and b) 800°C [55]. 14
Figure 2.10 Ductility trough for Fe22Mn0.6C steel [55]. 14
Figure 2.11 Effect of strain rate on ductility trough for Fe22Mn0.6C steel [15]. 15
Figure 2.12 Effect of Bi-Pb alloy composition on a) tensile properties of copper and b) interfacial energy between copper and Bi-Pb at 350°C [60]. 16
Figure 2.13 Classification of RSW crack locations [13]. 19
Figure 2.14 a) Temperature and b) stress in center surface (where Type A cracks form) during RSW simulated by SORPAS [13]. 21
Figure 3.1 a) MFDC pedestal welder and b) FANUC 2000iC robot with Type-C welding gun. 26
Figure 3.2 Schematics of resistance spot welds made using a) 3-sheet dissimilar and b) 2-sheet similar weld geometries. 27
Figure 3.3 a) Selection of cross-section plane using visible surface cracks and b) measurement of LME crack lengths [90]. 30
Figure 3.4 Tensile lap shear coupon geometry [90]. 31
Figure 3.5 Instron Model 4206 tensile tester. 31
Figure 3.6 Measurement of nugget diameter. 32
Figure 4.1 Comparison of a) mean crack length, b) number of cracks per weld, and c) 95th percentile crack length for DP980 welded with different pulsing conditions. 36
Figure 4.2 Histograms for all crack lengths measured in the range of a) 0 - 100 µm and b) 0 - 500 µm for DP980 welded with different pulsing conditions. 38
Figure 4.3 Comparison of a) mean crack length, b) number of cracks per weld, and c) 95th percentile crack length for TRIP1100 welded with different pulsing conditions. 40

Figure 4.4 Histograms for all crack lengths measured in the range of a) 0 - 100 μm and b) 0 - 1000 μm for TRIP1100 welded with different pulsing conditions. 42
Figure 4.5 Comparison of a) mean crack length, b) number of cracks per weld, and c) 95th percentile crack length for TRIP1100 welded with 6 cy pre-pulses of different currents. 44
Figure 4.6 a) Surface cracks and b) average surface crack length in TRIP1100 welded with 17 kA pre-pulses of different lengths. 45
Figure 4.7 Comparison of a) mean crack length, b) number of cracks per weld, and c) 95th percentile crack length for TRIP1100 welded with and without 17 kA, 1 cy pre-pulse. 46
Figure 4.8 Comparison of a) mean crack length, b) number of cracks per weld, and c) 95th percentile crack length for TRIP1100 welded with 4 kA pre-pulses of different lengths. 47
Figure 5.1 Micrographs of resistance spot welds of DP980 (a, b), TRIP690 (c, d), TRIP1100 (e, f), and TRIP1200 (g, h) welded at I_{max}+10%. LME cracks are circled [90]. 50
Figure 5.2 Comparison of a) mean crack length, b) number of cracks per weld, and c) 95th percentile crack length in samples of AHSS welded at I_{max}+10% [90]. 51
Figure 5.3 Comparison of peak load for coated vs. uncoated AHSS welded at I_{max}+10% [90]. 53
Figure 5.4 Relationship between a) mean crack length, b) number of cracks per weld, and c) 95th percentile crack length and weld strength loss for resistance spot welded AHSS [90]. 54
Figure 5.5 Histograms of LME cracks observed in TRIP1200 welded at I_{max}+10% fitted with a) a normal distribution and b) a lognormal distribution [90]. 55
Figure 5.6 a) Lognormal mean and b) lognormal median of samples welded at I_{max}+10%. Relationship between c) lognormal mean and strength loss and d) lognormal median and strength loss in resistance spot welded AHSS [90]. 56
Figure 5.7 a) Crack index for AHSS welded at I_{max}+10%. b) Relationship between crack index and strength loss for AHSS [90]. 58
Figure 5.8 a) Comparison of normal and lognormal median. b) Relationship between crack index calculated with normal median and strength loss [90]. 59
Figure 5.9 Correlation coefficient (R^2) for crack indices calculated with different percentile crack lengths. 60
Figure 5.10 Relationship between crack index and strength loss for crack index calculated using a) 20th, b) 60th, and c) 95th percentile crack length. 61
Figure 5.11 Correlation coefficient (R^2) for crack indices calculated with different percentile crack lengths with outlier removed. 62

Figure 6.1 Comparison of crack index for DP980 welded with different pulsing conditions. 64
Figure 6.2 Comparison of crack index for TRIP1100 welded with different pulsing conditions. 65
Figure 6.3 Iron-zinc phase diagram [24]. 67
Figure 6.4 a) EDS line scan of zinc coating remaining on TRIP1100 after a 12 cy pulse. Iron is shown in red, zinc is in green, and aluminum is in blue. b) Measurement of peak heights. c) Determination of peak half heights. d) Measurement of zinc coating thickness. 68
Figure 6.5 Method for determining amount of iron in the remaining zinc coating for a sample of TRIP1100 welded with a 12 cy pulse. 69
Figure 6.6 Average thickness and composition of zinc coating remaining after the first pulse. 70
Figure 6.7 a) Temperature and b) maximum principle stress in the weld shoulder of TRIP1100 welded with different pulsing conditions. 71
Figure 6.8 Comparison of crack index for TRIP1100 welded with 6 cy pre-pulses of different currents. . 72
Figure 6.9 Comparison of crack index for TRIP1100 welded with and without 17 kA, 1 cy pre-pulse..... 73
Figure 6.10 Comparison of crack index for TRIP1100 welded with 4 kA pre-pulse of different lengths. . 74
Figure 6.11 Average thickness and composition of zinc coating remaining after a 4 kA pre-pulse..... 75

List of Tables

Table 3.1 Compositions of LME susceptible AHSS. 24
Table 3.2 Mechanical Properties of AHSS. 25
Table 3.3 Welding parameters recommended by AWS D8.9 [19]. 26
Table 3.4 Pulsed welding schedules and associated nugget diameters for DP980 and TRIP1100. 28
Table 3.5 Pre-pulse welding schedules. 29
Table 4.1 LME cracking measurements and LSD for DP980 welded with different pulsing conditions. .. 37
Table 4.2 LME cracking measurements and LSD for TRIP1100 welded with different pulsing conditions. 41
Table 4.3 LME cracking measurements and LSD for TRIP1100 welded with 6 cy pre-pulses of different currents. 44
Table 4.4 LME cracking measurements and LSD for TRIP1100 welded with 4 kA pre-pulses of different lengths. 47
Table 5.1 LME cracking measurements and LSD for AHSS welded at I_{max}+10%. 52
Table 5.2 Comparison of nugget diameters for coated vs. uncoated AHSS welded at I_{max}+10% 53
Table 5.3 Significance testing for differences in crack index in AHSS welded at I_{max}+10%. 58
Table 6.1 Crack index and LSD for DP980 welded with different pulsing conditions. 64
Table 6.2 Crack index and LSD for TRIP1100 welded with different pulsing conditions. 65
Table 6.3 Crack index and LSD for TRIP1100 welded with 4 kA pre-pulses of different lengths. 74
Table 6.4 Nugget diameter for TRIP1100 welded with 4 kA pre-pulses of different lengths. 76

List of Abbreviations

AC	Alternating current
AHSS	Advanced high strength steel
ANOVA	Analysis of variance
AWS	American Welding Society
DP	Dual phase
EDS	Energy dispersive x-ray spectroscopy
EG	Electrogalvanized
FB	Ferritic-bainitic
GA	Hot-dip galvannealed
GI	Hot-dip galvanized
HDGA	Hot-dip galvannealed
HDGI	Hot-dip galvanized
HSLA	High strength-low alloy
IF	Interstitial free
LME	Liquid metal embrittlement
LSD	Least significant difference
MFDC	Medium frequency direct current
MWS	Minimum weld size
RSW	Resistance spot welding
SEM	Scanning electron microscope
TRIP	Transformation induced plasticity
TWIP	Twinning induced plasticity
UTS	Ultimate tensile strength
YS	Yield strength

List of Symbols

α	Statistical significance level
α'	Overall significance for significance testing with multiple means
c	Number of comparisons for significance testing with multiple means
DF	Degrees of freedom
F	Maximum load measured by tensile test
I	Current
I_{max}	Expulsion current
L	Crack length
μ	Mean (normal distribution); location parameter (lognormal distribution)
N	Number of measurements
n	Number of cracks
Q	Heat
R^2	Correlation coefficient
R	Resistance
R_c	Sheet-sheet contact resistance
R_e	Bulk resistance of electrode
R_{ew}	Electrode-sheet contact resistance
R_w	Bulk resistance of sheet
σ	Standard deviation (normal distribution); shape parameter (lognormal distribution)
t	Sheet thickness
$t_{DF, \alpha/2}$	Value of the t-distribution with DF degrees of freedom and significance level α
t_{dur}	Time

Chapter 1
Introduction

1.1 Background

Global automobile ownership has increased substantially in recent years, with the number of vehicles on the road nearly doubling from 670 million in 1996 to 1.32 billion at the end of 2016 [1]. This growth presents many challenges in terms of environmental sustainability. The Intergovernmental Panel on Climate Change warns that to limit global warming to less than 2°C, greenhouse gas emissions must be reduced by at least 40% between 2010 and 2050, and emissions levels near zero must be achieved by 2100 [2]. Greenhouse gas emissions have already caused catastrophic damage to the environment; global temperatures have risen, ocean acidity has increased, arctic sea ice mass has decreased, and sea levels have risen [2]. Without significant action, warming will continue and long-lasting changes in the climate will increase the likelihood of severe, pervasive, and irreversible impacts for people and ecosystems [2,3]. The transport sector is of particular importance for climate change reduction efforts [2,4]. According to the U.S. Department of Energy, transportation accounted for approximately 28% of energy consumption and 71% of petroleum usage in the United States in 2010 [5]. 80% of transportation energy is consumed by highway vehicles, including cars, trucks, and buses, while the remainder is used by non-highway vehicles, including military vehicles and air, water, and rail travel [5].

Since the invention of the internal combustion engine, great strides have been made in improving its efficiency. For instance, a small-block engine in a 1955 Chevrolet produced up to 195 hp at a volumetric efficiency of 45 hp/L, while a small-block engine today can produce up to 400 hp at an efficiency of approximately 70 hp/L [6]. Unfortunately, the greatest energy loss is from the combustion process itself, resulting in a maximum thermal efficiency of approximately 30% for gasoline powered engines [6]. Thus, researchers have turned to vehicle mass reduction as a potential avenue to reduce vehicle fuel consumption and greenhouse gas emissions [4–6]. In a mid-sized family vehicle with a weight of approximately 1450 kg, a 10% reduction in weight may improve fuel economy by 6% [6]. One method being explored to reduce vehicle weight is replacing traditional steel with lightweight materials.

Advanced high strength steels (AHSS) are an excellent candidate to replace conventional steel in automotive body manufacturing. Their high strength and ductility allows components to be made of

thinner sheets to reduce vehicle weight [7]. AHSS also offer engineers an increased degree of flexibility, as the strength and stiffness are highly customizable for different applications [7]. However, there are also significant challenges associated with the use of AHSS, such as increased complexity in manufacturing and difficulties with joining [8]. These steels are often coated with zinc for corrosion protection.

A common method of joining AHSS in automotive manufacturing is resistance spot welding (RSW), a welding process where an electrical current is passed through the sheets of metal to be joined and Joule heating causes melting at the interface [9]. The steel surface in contact with the water-cooled electrodes remain solid during welding, while the zinc coating melts. This molten zinc may penetrate into the grain boundaries of the solid steel in a process known as liquid metal embrittlement (LME) [10–13]. LME weakens the grain boundaries, nucleating surface cracks, which can propagate as stresses from welding cause the cracks to open up [10,14,15]. This is a safety concern, as in several recent studies, LME cracks were shown to reduce mechanical performance of RSW joined AHSS [16–18].

1.2 Objectives

The objective of this thesis is to investigate the occurrence of LME during RSW of AHSS with a particular emphasis on reducing LME cracking. The specific objectives are as follows:

1. Reduce severity of LME cracking in RSW of AHSS by altering the welding schedule.
2. Correlate LME severity with mechanical performance of RSW joints.

1.3 Criteria and Constraints

RSW parameters were selected using AWS D8.9 as a guide [19]. Details of the standard welding schedule and the modifications made to reduce LME may be found in Chapter 3. Mechanical performance of the welds was assessed using tensile lap shear testing. The mechanical testing methods and other characterization methods are also detailed in Chapter 3. This thesis work is limited to the investigation of LME in RSW of four grades of AHSS (DP980, TRIP690, TRIP1100, and TRIP1200) due to availability of material and interest from industry.

1.4 Thesis Outline

This thesis has been organized into seven chapters, which are detailed in the following paragraphs.

Chapter 1 gives an introduction to the thesis, including background, objectives, and constraints of the thesis work.

Chapter 2 summarizes published literature on topics relevant to the thesis: AHSS, RSW, and LME. It also demonstrates gaps in the literature that the thesis work is intended to fill.

Chapter 3 details the materials, welding procedures, and characterization methods used in the experimental work.

Chapter 4 describes the effect of using a pulsed welding schedule on the occurrence of LME in RSW using methods of LME quantification found in literature. It concludes that these commonly used methods of LME quantification are not sufficient to describe LME severity.

Chapter 5 explores alternative methods of quantifying LME and their relationship to weld performance. It concludes with the development of the crack index to link LME cracking to loss in tensile lap shear strength.

Chapter 6 re-analyzes the pulsed welding schedule data from Chapter 4 using the crack index analysis method. It also explores the mechanisms behind the observed effects.

Chapter 7 summarizes the main findings of this work and proposes avenues for future study.

Chapter 2
Literature Review

2.1 Advanced High Strength Steel (AHSS)

Advanced high strength steels (AHSS) are a family of steels with unique microstructures, which use complex deformation and phase transformation processes to achieve very high strength. Previously, steels with an ultimate tensile strength (UTS) greater than 550 MPa were categorized as AHSS. However, AHSS are now considered to be steel grades containing significant alloying and multiple phases [20]. Different types of AHSS can achieve different combinations of strength and ductility, as demonstrated in Figure 2.1. The AHSS studied in this thesis are dual phase (DP) and transformation induced plasticity (TRIP) steels, due to interest from industry. The characteristics of DP and TRIP steels will be discussed in Sections 2.1.1 and 2.1.2.

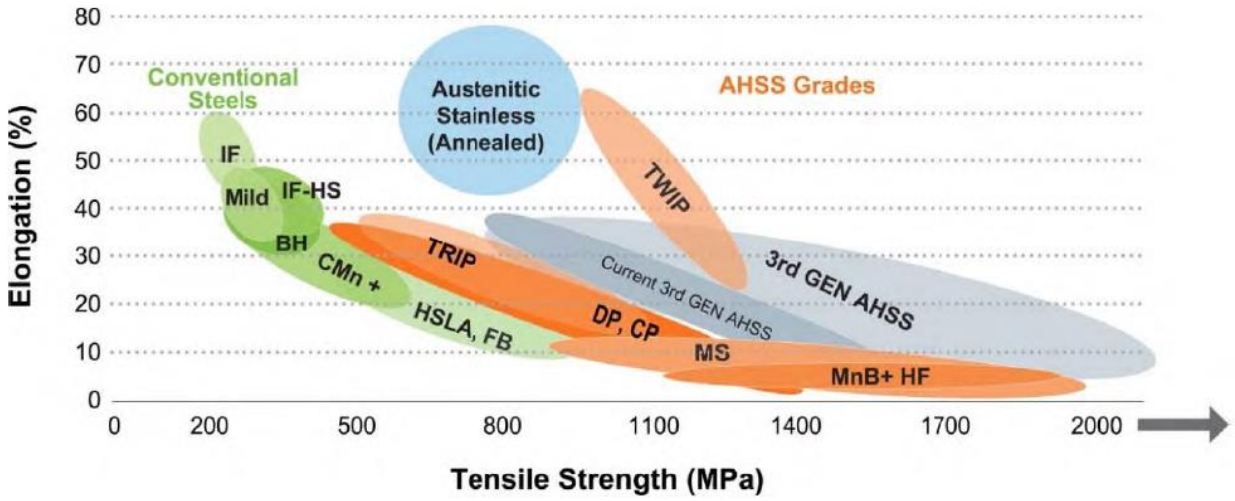

Figure 2.1 Steel strength-ductility diagram illustrating the range of properties available from AHSS [20].

Passenger vehicles are comprised of two distinct regions with different safety requirements (Figure 2.2). The front and rear ends of the vehicle, or "crumple zones," are designed to absorb as much energy as possible to cushion the impact and preserve the structure of the passenger compartment in the event of a front or rear end collision. DP and TRIP steels are ideal for this application as they exhibit high work hardening, strength, and ductility [8,20–22]. The second region is the passenger compartment, which is enclosed in a rigid "safety cage" designed to resist any deformation or intrusion that may

impinge on the space around the passengers. Complex-phase, martensitic, and hot-formed steels (not discussed in this thesis) are used for this application because they exhibit very high yield strengths [8,20–22].

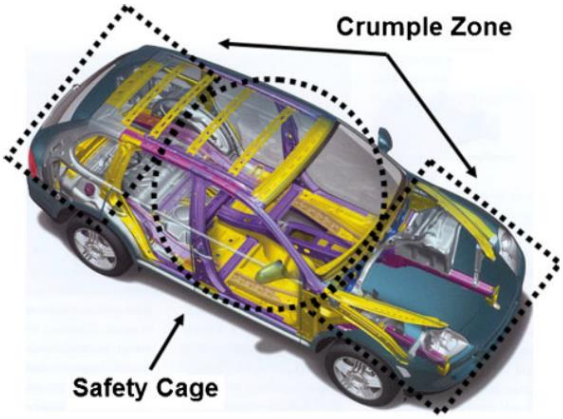

Figure 2.2 Two distinct regions of the automotive structure [21].

2.1.1 Dual Phase (DP) Steel

DP steel is composed of a ferrite matrix with 10 – 40% of martensite or martensite-austenite islands (Figure 2.3) [7,20]. Ferrite is a ductile phase of steel, composed of a solid solution of carbon in body centered cubic iron [23]. Martensite is a supersaturated solution of carbon in iron; the very high carbon content distorts the lattice, resulting in a microstructure that is strong but brittle [23]. In DP steel, the martensite islands give high strength while the continuous ferrite matrix gives the steel ductility. DP steels are produced by inter-critical annealing to produce a partially austenitic microstructure, followed by quenching to transform the austenite to martensite [7,20]. They typically have a UTS of 500 – 1200 MPa and a high initial work hardening rate [7,20]. DP steels exhibit greater elongation than conventional high strength-low alloy (HSLA) steel with a comparable UTS [20]. DP steels may also be strengthened by bake hardening [7,20].

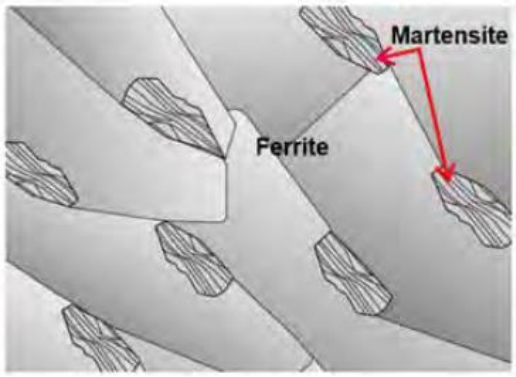

Figure 2.3 Schematic of DP steel microstructure [20].

2.1.2 Transformation Induced Plasticity (TRIP) Steel

TRIP steels contain a matrix of ferrite, with hard phases of martensite and bainite present in varying amounts and at least 5 vol% of retained austenite (Figure 2.4) [20]. Similar to DP steels, the hard phases dispersed in the ferrite matrix create a high initial work hardening rate. In TRIP steels the retained austenite transforms into martensite with strain, increasing the work hardening rate at higher strain as well [7,20]. This results in a higher ductility for TRIP steels than for DP steels with approximately the same UTS. TRIP steel is produced by a slow cooling from the austenite region to an intermediate temperature above room temperature, producing a partially ferritic microstructure. This is followed by an isothermal hold to produce bainite and then it is quenched to room temperature [7,20]. After quenching, some austenite remains untransformed because of the high concentrations of austenite stabilizers (carbon, manganese), while the remainder is transformed to martensite [7,20].

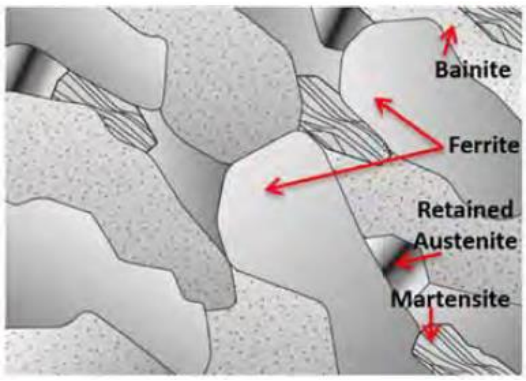

Figure 2.4 Schematic of TRIP steel microstructure [20].

2.2 Zinc Coatings

AHSS used in automotive manufacturing are typically coated with zinc to protect against corrosion. Zinc coatings protect the steel in two ways [24]:

1. Barrier protection – The coating physically separates the steel from the corrosive environment.
2. Galvanic protection – Zinc is anodic to iron and will sacrificially corrode, even if damage to the coating exposes the steel.

The zinc coatings commonly used in the automotive industry may be divided into two categories: hot-dipped and electrogalvanized [20].

2.2.1 Hot-Dip Galvanization

In hot-dip galvanization, the steel sheet is passed through a molten zinc bath. The steel sheet is pre-heated to the approximate temperature of the zinc bath to facilitate adhesion. After dipping, the excess zinc is removed from the surface with air knives to obtain the desired coating thickness [20,24,25]. 0.005 – 0.02 wt% of aluminum is added to the zinc bath to improve the appearance of the coating [24]. This type of coating is referred to as hot-dip galvanized (HDGI or GI) coating.

Following hot-dip galvanization, the coating may be annealed at a temperature of 450 – 600°C [24,26]. This allows iron to diffuse into the zinc coating, creating an iron-zinc alloy, typically with an iron content of 8 – 12% [20,24–26]. This type of coating is referred to as hot-dip galvannealed (HDGA or GA).

2.2.2 Electrogalvanization

The other commonly used method for applying the zinc coating is electrogalvanization. In this method, zinc is electroplated onto the steel substrate [20,24]. Pure zinc coatings can be produced, which are thinner, more aesthetically appealing, and require lower processing temperatures [20]. These coatings are referred to as electrogalvanized (EG) coatings.

2.3 Resistance Spot Welding (RSW)

Resistance spot welding (RSW) is a fusion welding process in which the material is melted by resistive heating generated by passing an electrical current through the workpiece [9,21,27,28]. A typical automobile contains 3000 – 6000 spot welds, making RSW the most widely used joining technique in the

automotive industry [29,30]. The features of RSW which make it ideal for automotive manufacturing include its low cost, high operating speeds, and suitability for automation [21,28].

2.3.1 RSW Fundamentals

The RSW process consists of five steps, which are illustrated in Figure 2.5 [31]:

1. Workpiece is clamped between the electrodes.
2. The full electrode force is applied to the workpiece.
3. Electrical current is applied for a specified time, causing melting at the sheet-sheet interface.
4. The current is stopped and the workpiece is held under the electrode force to allow molten metal to solidify. The length of time for which the workpiece is held is known as the holding time.
5. Electrode force is released.

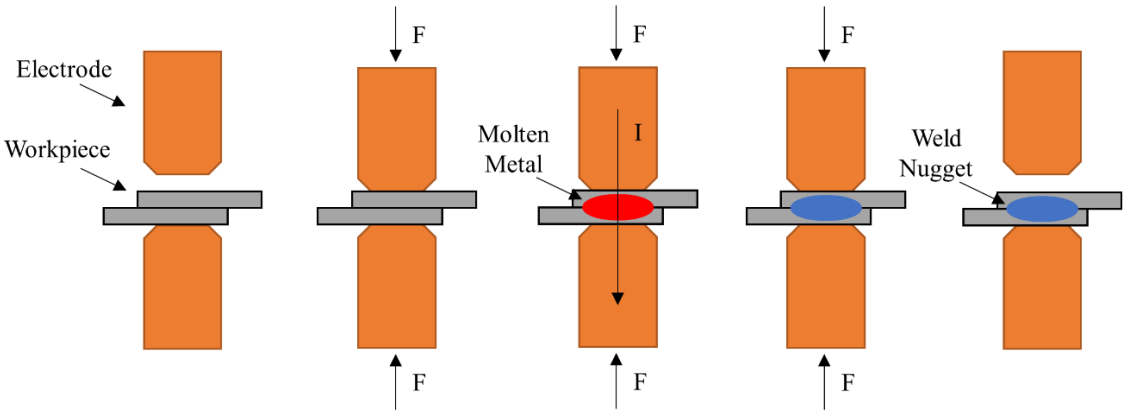

Figure 2.5 Steps of the resistance spot welding process.

The heat generated by Joule heating is given by the equation

$$Q = I^2 R t_{dur} \tag{2.1}$$

where Q is the heat generated, I is the applied current, R is the total resistance across the electrodes, and t_{dur} is the duration of the applied current [9]. The total resistance R is composed of seven individual resistances that exist in the circuit (Figure 2.6). R_e is the bulk resistance of the electrodes, R_w is the bulk resistance of the sheets, R_{ew} is the electrode-sheet contact resistance, and R_c is the sheet-sheet contact resistance [30]. Because these resistances are in series, they can simply be summed to calculate R. R_c is

generally the highest of the resistances, resulting in the majority of the heat generated during the welding process being concentrated at the sheet-sheet interface [31].

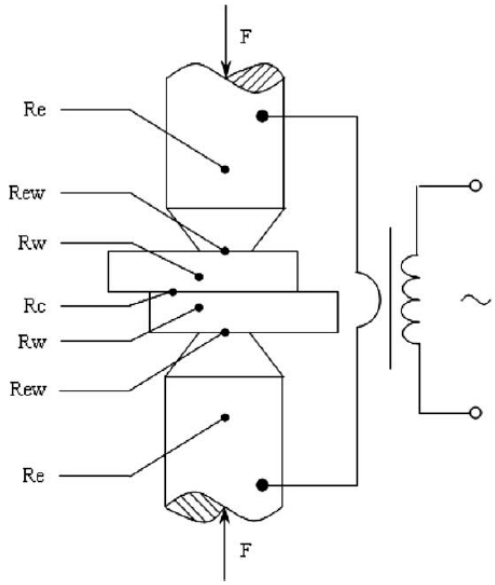

Figure 2.6 Schematic of the resistances present in RSW [30]**.**

During RSW, the resistance continuously changes as the material is heated and melted. From the dynamic resistance curve (Figure 2.7), the stages of spot weld formation can be described as follows [32]:

1. Surface breakdown – The initial contact resistance is very high due to the presence of surface films, oxide layers, or other contaminants. When the current begins to flow, the heat generated will cause a breakdown of these contaminants, which is observed as a drop in resistance.
2. Asperity softening – Metal-to-metal contact now exists but the effective contact area is low due to surface roughness (asperities). As the metal heats, these asperities will soften, increasing the contact area and decreasing the resistance further.
3. Temperature increase – In this stage, the bulk resistance of the metal dominates the total resistance. As resistivity increases with increasing temperature, an upward slope is seen in the dynamic resistance curve.
4. First melting – Melting begins at the interface of the two sheets. The resistivity of the bulk metal continues to increase, while the melting at the interface causes a decrease in sheet-sheet contact resistance (due to the increased contact area). As the temperature stabilizes and nugget growth

begins to dominate the resistance, the resistance begins to decrease. This point of the curve is known as the β peak.

5. Nugget growth – The nugget continues to grow, further decreasing the resistance. Softening of the metal due to the increased temperature causes the electrode to push into the metal and create an indentation (mechanical collapse). This reduces the sheet thickness (current path) and contributes to the decrease in resistance. If the nugget grows enough that it cannot be contained by the surrounding solid metal, expulsion (ejection of droplets of molten metal) may occur. This causes a decrease in sheet thickness and introduces many new current pathways, resulting in a sharp drop in resistance.

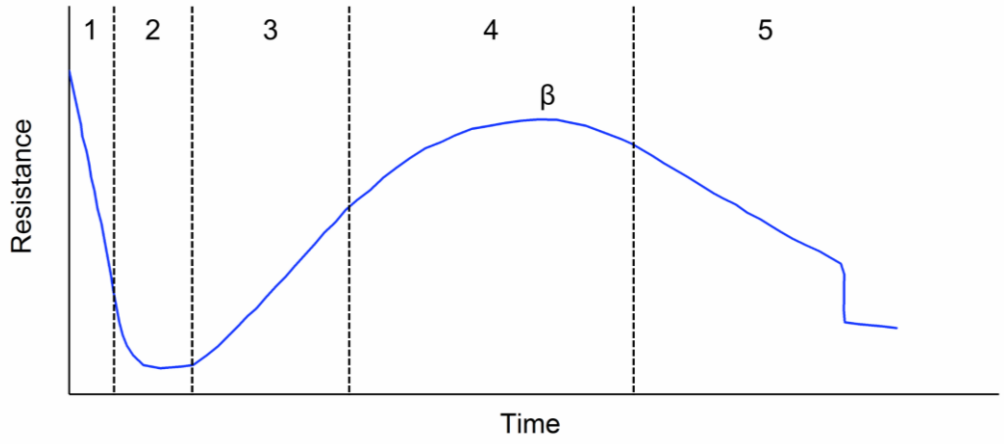

Figure 2.7 Theoretical dynamic resistance during RSW.

The sheet-sheet contact resistance is highly dependent on the surface condition of the sheets being welded. This is demonstrated by the first two stages of RSW (surface breakdown and asperity softening). In addition to surface contaminants and oxides, coatings deliberately applied to the material will also have an impact on contact resistance and weldability. As previously stated, AHSS used in automotive manufacturing are typically zinc coated for corrosion protection. During welding of hot-dip galvanized steel sheets, the zinc coating melts first, reducing the contact resistance at the sheet-sheet interface. As a result, welding of hot-dip galvanized steel requires a higher current than welding of bare steel [9,28]. However, galvannealed coatings have a higher resistivity than the free zinc in galvanized coatings, meaning that more heat is generated from the coating and the effect on weldability is less pronounced [9].

2.3.2 Welding Parameters

RSW is a highly customizable process with many parameters that may be altered by the operator, such as current, welding time, electrode force, hold time, and electrode tip diameter. The most important parameters are current, welding time, and electrode force, as these three parameters have a direct effect on the nugget size [21,30]. Recall from Equation 2.1 that heat input depends on current, welding time, and resistance. Increasing heat input by increasing the current or welding time results in a larger nugget diameter [21,28,30]. Electrode force also has an effect on heat input because the metal sheets must be pressed together to allow current to flow. A larger electrode force reduces the sheet-sheet contact resistance by increasing the effective contact area, causing a decrease in heat input and nugget diameter [21,27,30].

Weld lobe curves, such as the one shown in Figure 2.8, show the welding process window and are often used to select the welding parameters for a particular material. On the left side of the lobe are combinations of current and welding time which yield undersized welds. Undersized welds are not acceptable because nugget diameter affects the weld strength and fracture mode of the weld [21,33]. A small nugget corresponds to smaller shear and cross tension strengths. AWS D8.9 defines the minimum weld size (MWS) as

$$MWS = 4\sqrt{t} \tag{2.2}$$

where t is the sheet thickness [19]. When welding dissimilar materials with different sheet thickness, average sheet thickness is used. On the right side of the weld lobe are parameters with which expulsion occurs. Expulsion is typically not acceptable because it may cause defects, such as excessive electrode indentation, voids, and porosity, which are detrimental to weld mechanical performance [34,35]. Welding in the center of the weld lobe is desirable to produce welds of acceptable size, without expulsion defects. The location and width of the weld lobe are dependent on the material characteristics of the sheets being joined, such as bulk resistivity, sheet thickness, and surface condition [28]. A wider weld lobe is desirable because it indicates that a larger range of parameters can be used to make acceptable welds. This means the process has a higher degree of tolerance to variations in production conditions, such as surface conditions, fit-up between the sheets, and electrode tip quality, which influence nugget size [28].

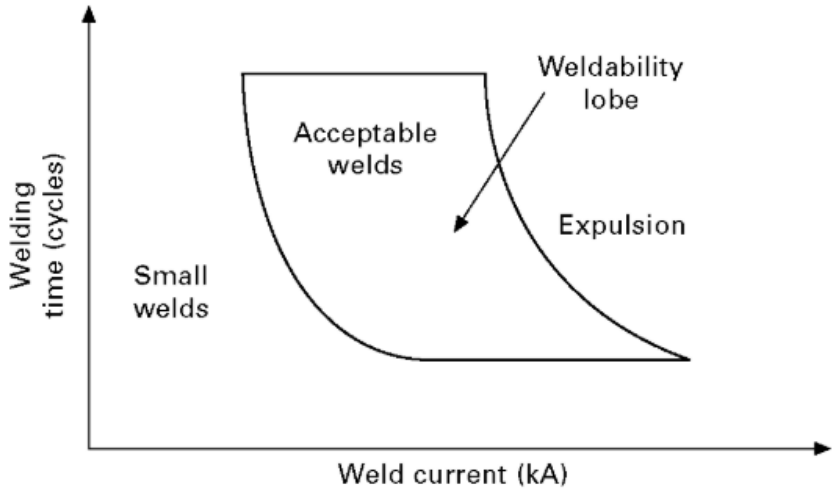

Figure 2.8 Weld lob curve for RSW [28]**.**

In addition to current, time, and electrode force, there are a number of other important parameters that do not affect heat input but still have an impact on weld quality. For instance, holding time does not affect the heat generated or the nugget diameter [36,37]. However, longer holding times have been shown to reduce shrinkage voids and increase fusion zone hardness [38,39]. In addition, increasing the electrode tip diameter will reduce the current density and slow the nugget growth, resulting in a smaller nugget diameter [28].

2.3.2.1 Pulsed Welding Schedules

The most basic RSW schedule consists of a single pulse with constant current. This type of welding schedule provides approximately constant heat input throughout the welding time [9]. In some cases it may be beneficial to apply a multiple pulse welding schedule. There are three different pulsed welding schedules that are detailed in the literature: pre-pulsing, pulsing during the weld, and post-pulsing.

Pre-pulsing refers to the application of a shorter current pulse before the main welding pulse. This method has been used to remove low temperature coatings or surface oxides that may interfere with the welding process [11,40,41]. The pre-pulse is used to melt the coating and push it out of the weld area, while the main welding pulse forms the weld nugget.

Pulsing during the weld involves dividing the main welding current into several shorter pulses. This technique has been shown to slow nugget growth and delay expulsion, which increases weldable

current range [42,43]. AWS D8.9 recommends this type of welding schedule when welding sheets thicker than 1.3 mm [19].

Post-pulsing has been used to modify the microstructure and mechanical properties of a weld by applying a pulse after the main welding pulse [44–48]. The nugget is formed during the first pulse. In the second pulse, the center of the nugget is re-melted, while the edges are annealed. Using a post-pulse has been shown to improve mechanical performance of the welds [44–48].

2.4 Liquid Metal Embrittlement (LME)

Liquid metal embrittlement (LME) refers to the reduction in strength and ductility that may occur when a metal or alloy is stressed in the presence of liquid metal [49]. This occurs due to liquid metal penetrating into the solid metal grain boundaries, weakening the grain boundaries and causing nucleation of surface cracks [11,15,50]. In the presence of tensile stresses, these cracks can open up, allowing zinc to penetrate further into the grain boundary and propagate the crack [15]. No bulk chemical or structural changes are caused to the solid metal [49].

There are three pre-requisite conditions that must be met for LME to occur: liquid metal contacting solid metal, tensile stress, and a susceptible solid/liquid metal system [49]. LME has only been observed for certain pairs of solid/liquid metals. Cu_{solid}/Bi_{liquid}, Al_{solid}/Ga_{liquid}, and $steel_{solid}/Zn_{liquid}$ are examples of such solid/liquid metal pairs [15,50–54]. The $steel_{solid}/Zn_{liquid}$ system is of particular interest for this thesis. The liquid metal must also be in direct contact with the solid metal; liquid metal embrittlement may be delayed or inhibited by the presence of an oxide layer on the surface of the solid [49]. These conditions are necessary for LME to occur but not sufficient [49]; there are a number of other factors which also impact the occurrence of LME and will be discussed in the following sections.

2.4.1 Effect of Temperature

LME is a temperature dependent phenomenon and only occurs within a specific temperature range, known as the “ductility trough” [49]. The onset temperature of LME must be above the melting temperature of the embrittling agent, but LME may not occur immediately following melting. For instance, in the $steel_{solid}/Zn_{liquid}$ system, the melting temperature of zinc is 419°C but LME has been observed to begin at around 700°C [15,50,55–57]. Beal theorized that at temperatures below 700°C, the critical stress required for LME cracking is higher than the yield strength (YS) and UTS [57]. This results in plastic deformation occurring before LME cracks begin to form. As the temperature increases above 700°C, the critical stress for LME cracking decreases to below the YS and UTS, causing LME cracking to

begin before plastic deformation. However, Beal also noted that the LME onset temperature is highly dependent on experimental methodology. For instance, the effect of strain rate on the ductility trough will be discussed in the next section.

The effect of temperature on LME can be seen in Figure 2.9, which shows that at 600°C there was no difference in the stress-strain curves for a bare and electrogalvanized Fe22Mn0.6C TRIP steel (Figure 2.9 a)), while at 800°C the EG coated steel showed a significant reduction in both strength and ductility (Figure 2.9 b)) [55]. The high temperature tensile test was repeated at many different temperatures to construct the complete ductility trough shown in Figure 2.10. The ductility recovery above 900°C is attributed to the vaporization of zinc, as its boiling point is 907°C.

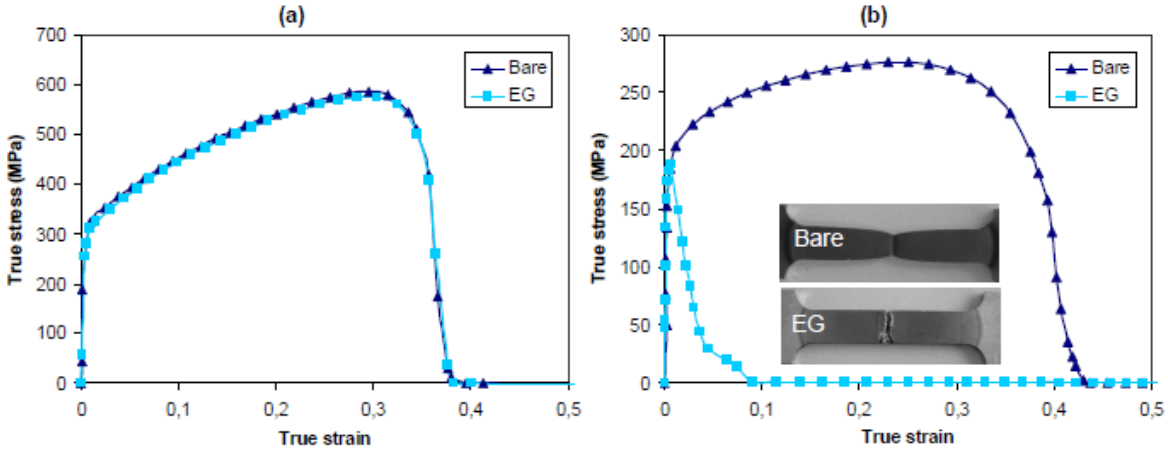

Figure 2.9 Stress-strain curves for Fe22Mn0.6C steel at a) 600°C and b) 800°C [55]**.**

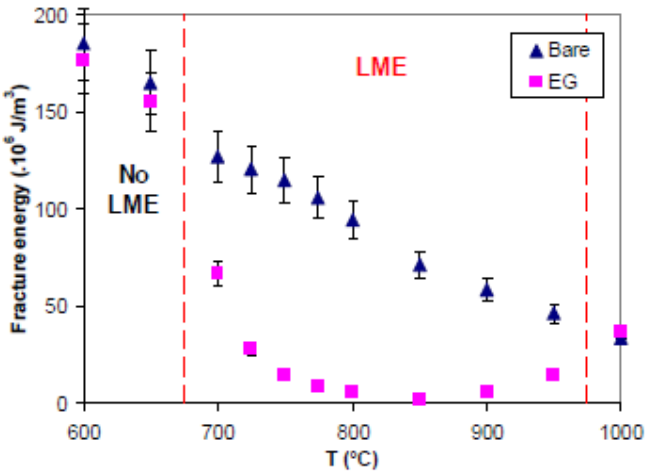

Figure 2.10 Ductility trough for Fe22Mn0.6C steel [55]**.**

2.4.2 Effect of Strain Rate

The high temperature tensile tests shown in the previous section may not be an ideal method to assess LME sensitivity because the strain rate has an impact on LME. In Al_{solid}/Hg-3% Zn_{liquid} and Ti_{solid}/Cd_{liquid} systems, an increased strain rate was shown to increase the ductility recovery temperature [58,59]. Similar behaviour has been observed in the $steel_{solid}$/Zn_{liquid} system and the reduction of the LME onset temperature has also been shown [15,50,55]. This widening of the ductility trough is illustrated in Figure 2.11.

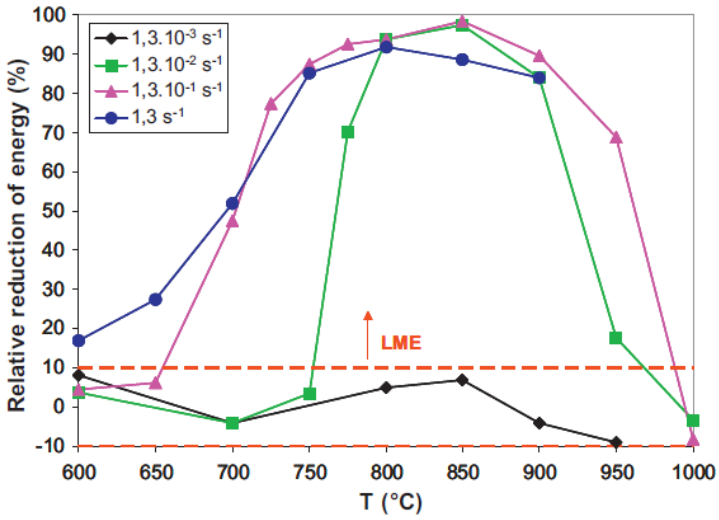

Figure 2.11 Effect of strain rate on ductility trough for Fe22Mn0.6C steel [15]**.**

2.4.3 Effect of Composition of Liquid Metal

As previously discussed, only specific couples of solid and liquid metals exhibit LME behaviour. Therefore, it follows that changes to the composition liquid metal will have an impact on the LME severity. For instance, copper experiences LME when in the presence of some liquid Bi-Pb alloys at 350°C. However, when the Pb content is increased above 30 wt%, the LME severity decreases [60]. This is demonstrated in Figure 2.12 a), which shows that as the Pb content of the Bi-Pb alloy increases, the percent elongation and fracture stress of the copper also increase. It has been proposed that changes in LME severity with changing alloy composition are due to differences in the interfacial energy between the solid and liquid metal [60]. In the case of Cu_{solid}/Bi-Pb_{liquid}, as the Pb content increases, the interfacial energy increases (Figure 2.12 b)), corresponding to the decrease in LME severity [60]. An increase in the interfacial energy will reduce the degree of wetting between the solid, which will reduce the likelihood of LME occurring (recall that direct contact between solid and liquid is a necessary condition for LME).

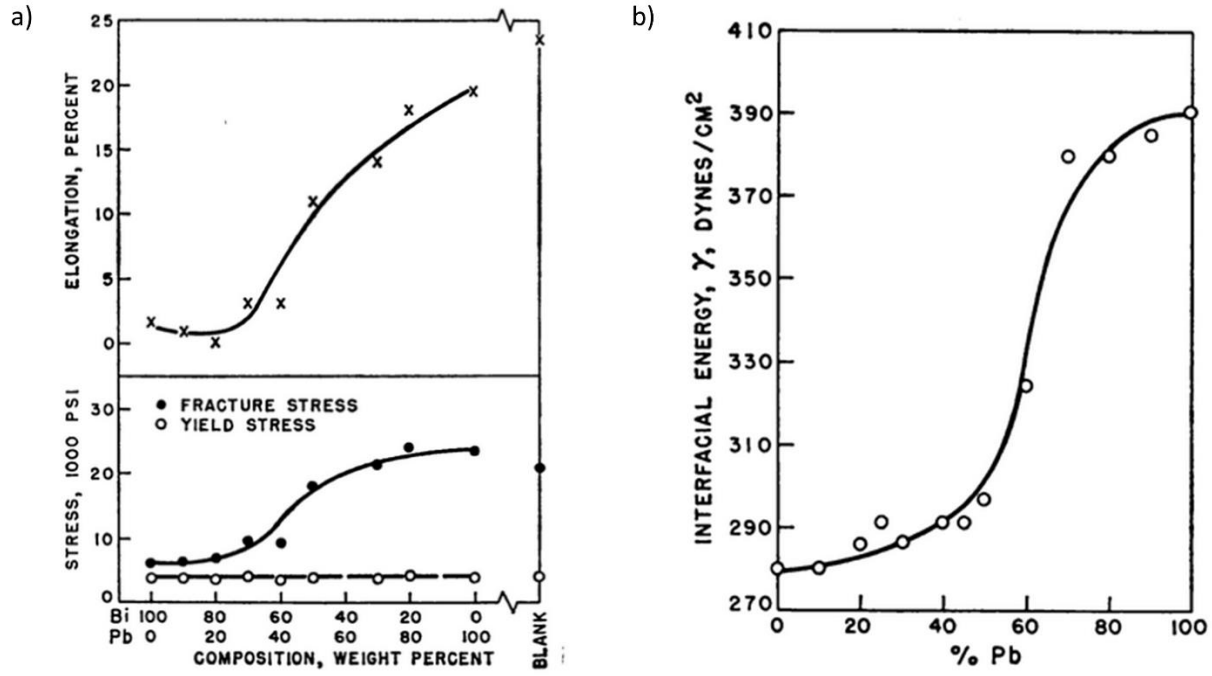

Figure 2.12 Effect of Bi-Pb alloy composition on a) tensile properties of copper and b) interfacial energy between copper and Bi-Pb at 350°C [60]**.**

A second way in which alloying may have an impact on LME severity is due to the possibility that low melting temperature metals may act as inert carriers to bring the embrittling agent in contact with the solid [49,61]. For instance, it has been shown that pure mercury does not embrittle solid cadmium [62]; however, a solution of 8% indium in mercury was observed to embrittle cadmium at room temperature [61]. This suggests that the indium is responsible for the embrittlement, and the mercury simply was simply the carrier of the embrittling species, allowing LME to occur below the melting temperature of indium (156.6°C). Similar behaviour has been observed in the $steel_{solid}/Zn_{liquid}$ system. Samples of C70D steel did not demonstrate LME when strained in contact with pure zinc, but embrittlement was seen when 2% of tin was added to the zinc bath [63].

The three types of zinc coating discussed in Section 2.2 (GI, GA, EG) have different composition and therefore should display different patterns of LME cracking. This was confirmed by Ashiri *et al*, who observed LME cracking in resistance spot welds of samples of the same TWIP steel with the different coating types [10,43]. LME was worst in the GI coated samples, followed by the GA coated samples, then the EG coated samples. The reduced LME sensitivity of the GA coating is typically attributed to its higher

melting temperature [10,43]. EG coatings tend to be even less LME sensitive because they are typically pure zinc; the addition of alloying elements, such as aluminum or tin, may worsen LME cracking [12,63].

2.4.4 Effect of Solid Metal Microstructure

In the $steel_{solid}/Zn_{liquid}$ system, it is generally agreed that austenite grain boundaries are more susceptible to LME than other microstructures. A number of studies have noted that zinc appears to propagate along austenite grain boundaries to create the microcracks that are characteristic of LME [57,64–67]. Conversely, Kang *et al*, observed no LME in zinc-coated IF steel tensile tested in both the ferrite and austenite stability ranges, leading them to conclude that grain boundary composition is more critical to LME sensitivity than crystal structure [68]. However, this result does not necessarily conflict with other studies because the temperature used to test the IF steel in the austenite stability range (950°C) may have been outside the temperature ductility trough for the particular conditions used in the study. In addition, LME severity has been observed to increase with increasing strength of the steel [69,70]. However, commercially available steels with different strengths and microstructures also have different chemical composition, which may impact LME susceptibility as well [69].

2.4.5 Possible Mechanisms

A number of models have been proposed to explain the mechanism by which LME occurs. These models can be divided into three categories: brittle fracture theory based propagation, plasticity (ductile fracture) based propagation, and grain boundary diffusion models [69].

The brittle fracture models are based on the idea that liquid metal in the grain boundaries reduces their surface energy, also reducing the energy required for fracture. The Stoloff-Johnson-Westwood-Kamdar model posits that liquid metal weakens the atomic bonds at the crack tip, allowing an applied stress to separate them and propagate the crack [71,72]. The Robertson-Glickman model suggests that stress at the crack tip acts as the driving force for localized dissolution of the base metal that propagates the crack [73,74].

The plasticity based propagation models are based on the idea that adsorption of liquid metal atoms affects the formation and motion of dislocations. In the Lynch model, the liquid reduces the strength of the interatomic bonds at the crack tip (similar to the Stoloff-Johnson-Westwood-Kamdar model), facilitating the nucleation of dislocations [75]. Dislocation slip leads to the formation of micro-voids, which combine with the crack. The Popovich model agrees that adsorbed liquid metal increases

generation of dislocations and further suggests that increased dislocation activity leads to localized work hardening and micro-crack formation [76].

The grain boundary diffusion models suggest that LME occurs due to the diffusion of the embrittling atoms along the grain boundaries of the solid. The Krishtal-Gordon-An model suggests that the embrittling atoms diffuse a short distance into the base material grain boundaries, where they lower crack resistance and suppress slip [77,78]. Once the concentration of the embrittler has built up to a critical level, crack nucleation occurs at the head of dislocation pileups. In the Klinger-Rabkin model, the diffusion of embrittling atoms along the grain boundaries creates stresses due to the Kirkendall effect, which may cause crack nucleation and intergranular fracture [79].

In addition to these general models, several mechanisms have also been proposed specifically for the $steel_{solid}/Zn_{liquid}$ system. Beal *et al*. proposed the following simple mechanism [15]:

1. Liquid zinc penetrates along steel grain boundaries due to tensile stresses.
2. When the critical amount of zinc penetration is achieved, subsequent tensile stresses cause the crack to open up.
3. The crack fills with liquid zinc, which then penetrates further into the grain boundary beyond the crack tip and the process repeats.

This is similar to the brittle fracture theory based propagation models in that liquid metal reduces the grain boundary strength, allowing the external stresses to form or propagate a crack.

Kang *et al*. proposed an alternative mechanisms for LME in TWIP steel, in which both liquid zinc penetration and grain boundary diffusion ahead of the liquid penetration path play a role in LME [68]. In this mechanism, zinc penetration occurs by solid-state grain boundary diffusion. Once the zinc concentration exceeds the solubility of zinc in steel, liquid zinc is formed, causing a loss in grain boundary cohesion and the initiation of cracks. This mechanism is more similar to the grain boundary diffusion models proposed by Krishtal-Gordon-An and Klinger-Rabkin.

2.5 LME in RSW of AHSS

LME is a concern when resistance spot welding zinc-coated AHSS. Because most of the heat is generated at the sheet-sheet contact area, the surfaces of the steel remain unmelted. However, zinc has a significantly lower melting point (419°C) than steel (approximately 1500°C); therefore, the zinc coating

on the surfaces will melt. This results in liquid zinc in contact with solid steel in the presence of stresses that develop during welding.

2.5.1 Characteristics of LME Cracking in Resistance Spot Welds

LME cracks have been classified by Choi *et al.* into three types based on their location in the weld [13,16,80]:

1. Type A cracks are located in the center area, which is in contact with the electrode during welding.
2. Type B cracks are located in the weld periphery, which is not in contact with the electrode during welding.
3. Type C cracks are located at the interface between the sheets.

The three types of cracks are illustrated in Figure 2.13.

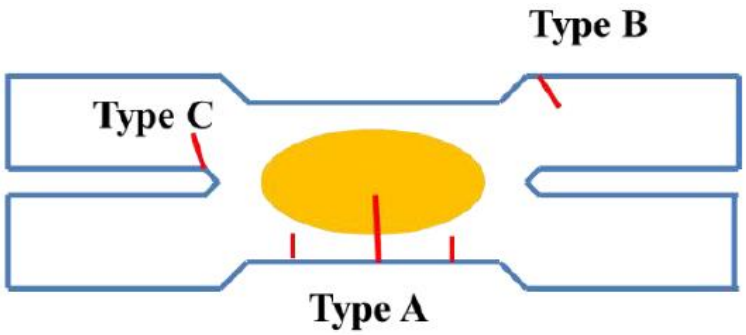

Figure 2.13 Classification of RSW crack locations [13]**.**

Type B cracks are the most common and have been observed in many studies [10–14,16,43,67,80]. According to a study by Ashiri *et al*, this is because this area is not in contact with the water-cooled electrode and therefore experiences higher temperatures and stresses [10]. Ashiri termed the weld periphery the "supercritical LME area" due to the frequent LME cracking in this area. Type A cracks are observed less frequently but have also been seen in a number of studies [11–13,16,17,67,80]. Type C cracks are rare and have only been observed in only a few studies [16,80].

LME cracks can be identified by their intergranular path and the presence of zinc inside the crack [10,13,17,43,80,81]. Some studies have also noted that copper was found in the LME cracks (indicating electrode degradation) [11,67]; however, this has only been observed in the minority of cases where the composition of the embrittling agent was measured.

2.5.2 Effect of Welding Parameters on LME

As noted in Section 2.3.2, there are a number of parameters which can be adjusted in RSW to obtain the desired weld performance. In particular, current, welding time, and electrode force have a direct effect on the heat input and nugget diameter (Equation 2.1). Several studies have been conducted to determine the impact of these important welding parameters on LME cracking, with the results showing that a larger heat input corresponds to more severe LME cracking. Ashiri *et al*. observed that LME cracking only occurred when a critical nugget diameter was exceeded [10]. A larger heat input resulted in a faster rate of nugget growth and more thermal expansion, leading to higher stresses in the weld shoulder. This is corroborated by several studies in which LME cracks were observed only at high welding currents [43,67,82]. Additionally, Kim *et al*. showed that above this critical heat input, LME cracking became more severe as current and welding time were increased [11]. Interestingly, the effect of welding time on LME severity does not seem to be an effect purely of heat input; Choi *et al.* demonstrated that lengthening the welding time while reducing current to maintain the same nugget diameter resulted in more severe LME due to the increased liquid metal contact time [13]. Finally, a reduction in electrode force causes an increase in heat input and decrease in cooling efficiency due to the reduced contact at the sheet-sheet interface and also corresponds to an increase in LME severity [11,13,14,80].

Although it does not have an impact on the heat input, the hold time also plays a role in the formation of LME cracks. It has been observed that increasing the hold time causes a reduction in LME cracking, especially in Type A cracks [11,16,67,80]. This is because during the holding time, the weld surfaces are under compressive stress and temperature is decreasing. When the electrodes are released, the stress changes from compressive to tensile and temperature increases (Figure 2.14) [13,16,80]. With a long enough hold time, temperature in the center of the weld surface (where Type A cracks form) can be reduced enough that there is no liquid zinc present when the electrodes release and the surface experiences tensile loading. A similar effect was observed for Type C cracks [80]. Conversely, Type B cracks are thought to form during heating, and therefore, are not affected by holding time [13].

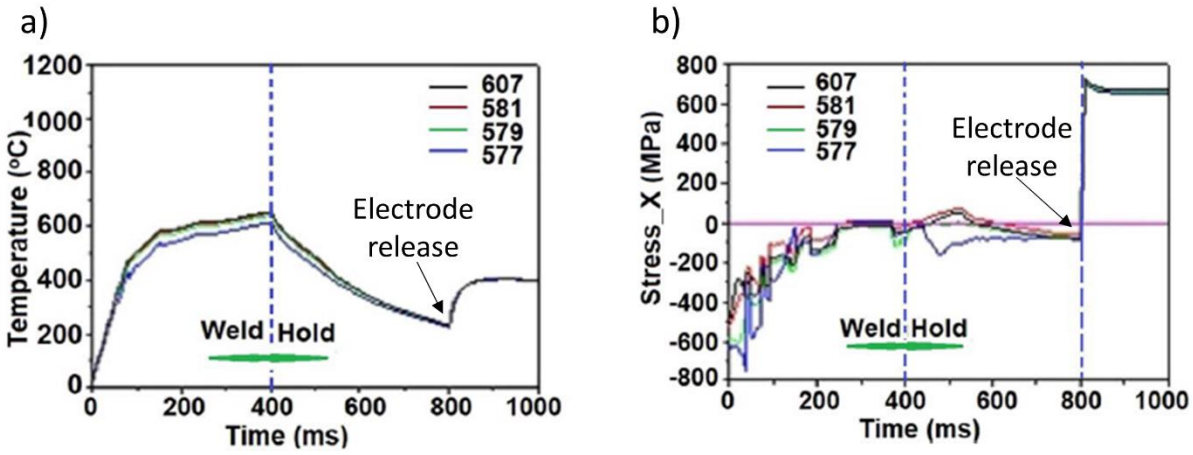

Figure 2.14 a) Temperature and b) stress in center surface (where Type A cracks form) during RSW simulated by SORPAS [13]**.**

2.5.3 Effect of LME on Weld Mechanical Performance

Currently, it is unclear what impact LME has on the mechanical performance of resistance spot welds. Several studies have shown no impact of heat affected zone cracking, including LME cracking, on tensile or fatigue properties [11,83–87]. However, a study by Choi *et al*. demonstrated a loss in mechanical properties (tensile shear and cross tension strength, absorbed energy, and fatigue life) in GI coated TRIP1180 only when LME cracks longer than 325 µm were present. In addition, DiGiovanni *et al*. concluded that crack location was a significant factor in determining whether a particular LME crack would have an impact on tensile lap shear strength and fracture [17,18]. The weld is not uniformly load during tensile lap shear testing and only cracks located in highly stressed areas were shown to reduce the weld strength. Further study is needed to establish a clearer relationship between LME cracking and weld performance.

2.5.4 Quantifying LME Severity

Determination of a quantitative relationship between LME cracking severity and mechanical performance is complicated by the fact that there is no standard method used to quantify LME cracking. Methods which have been described in literature include: maximum crack length [10,13,16,17,43,88], total length of surface cracks [12], total crack surface area [81], surface cracking ratio [11], number of cracks per weld [88], and mean crack length [14,89]. Large variability is associated with many of these commonly used methods, making it difficult to determine differences in LME crack populations with

confidence [90]. To be of descriptive value, any cracking metric developed should be relatable to weld performance. However, no such connection has been made with any of the aforementioned LME cracking quantification methods.

2.5.4.1 Statistical Distributions

The arithmetic mean (referred to hereafter simply as "mean") is a commonly used measurement of central tendency in a population. Therefore, it is logical that mean crack length would be used as a metric for LME severity, as it has been in several studies [14,89]. Use of the mean crack length to describe cracking requires the underlying assumption that the total crack population is normally distributed. The normal (or Gaussian) distribution is one of the most commonly observed probability distributions, with many numerical populations in nature closely fitting a normal distribution [91]. However, there are a number of other probability distributions which may be more appropriate for characterizing crack size. For instance, cracks observed in aircraft service inspections have been modelled with a lognormal distribution [92], crack length distribution density in fatigue fracture specimens has been observed to fit a Pareto distribution [93], and crack growth resistance coefficient has been modelled using a Weibull distribution [94]. In addition, large errors associated with mean crack length suggest that the normality assumption may not be applicable to LME cracking [90]. Further study into the distribution of crack length populations in LME affected welds would be beneficial to developing a better method of quantifying LME in resistance spot welds.

2.5.4.2 Outliers

Maximum crack length is another LME cracking metric which is commonly used in literature [10,13,16,17,43,88]. However, maximum crack length is very inconsistent between samples. For example, DiGiovanni *et al.* found that in welds of TRIP1100 made using the same welding parameters, the maximum crack length varied from 100 μm to over 1000 μm [17]. The maximum crack length will also be strongly affected by any outliers. Therefore, it is recommended that 95^{th} percentile crack length is substituted for maximum crack length, to reduce the effect of outlying data points.

2.5.5 Methods for LME Reduction in RSW

As discussed in Section 2.5.2, the welding parameters used have a large impact on the LME severity in a weld. Thus, the obvious solution for LME suppression is to select parameters that do not create favourable conditions for LME to occur. This would primarily mean reducing heat input (lowering welding current and/or time and increasing electrode force), while still ensuring the minimum nugget

diameter is met (Equation 2.2). Extended hold times may also be used to reduce LME cracking. However, increasing hold time is only effective for Type A cracks and will increase manufacturing cycle time. In cases where these techniques do not sufficiently reduce LME cracking, several alternative welding schedules have also been suggested.

Ashiri *et al*. proposed a two pulse welding schedule, which was capable of producing LME free welds in an electrogalvanized TWIP steel [43]. A longer first pulse was used to generate the minimum nugget diameter and a second shorter pulse was used to grow the nugget. SORPAS simulations demonstrated that this welding schedule resulted in lower temperatures and stresses in the supercritical LME area due to a lower heating rate. However, it should be noted that the nugget diameter was not kept constant between the single and double pulse welds, meaning that the effect of the welding schedule cannot be isolated from the effect of the reduced heat input. Further study is needed to determine the impact of pulsing on LME severity and the mechanisms by which this impact occurs.

Kim *et al*. were able to reduce LME severity in welds of GA coated TRIP590 through application of a pre-pulse [11]. As noted in Section 2.3.2.1, this technique has been used to remove low melting temperature coatings and oxides that may interfere with welding. The pre-pulse current is flowed for a short time before the main welding current to melt the zinc, while the electrode force "squeezes" it out of the welding area. De Cooman *et al*. demonstrated that LME could be prevented in press hardened steel by reducing the coating weight [95], which indicates that Kim's approach of reducing LME by removing zinc is valid. In Kim's study, a pre-pulse current 2 kA below the main welding current was effective for reducing LME. However, only two different pre-pulse conditions were tested, meaning that the possibilities and constraints of this method have not been fully explored. Additional study to determine under which conditions this method may be used to reduce LME cracking would be beneficial.

Chapter 3
Methodology

One of the main goals of this research is to reduce the occurrence of LME cracking in resistance spot welds by altering the welding schedule. Multiple pulse welding schedules have shown promise in this regard but have not been fully explored. Therefore, a major component of this thesis is investigating the effects of multiple pulse welding schedules on LME severity and the mechanisms behind these effects. Two different pulsed welding schemes are explored: pulsing during the main welding current (referred to hereafter simply as pulsed welding) and applying a pre-pulse before the main welding current (referred to hereafter as pre-pulse welding). The second goal of this research is to relate LME severity to mechanical performance of the welds. This chapter details the materials and methods used in both of the above studies.

3.1 Materials

Four different grades of AHSS were studied in this research: DP980, TRIP690, TRIP1100, and TRIP1200. An interstitial free (IF) steel was also used for welding dissimilar joint geometries. All of the materials were industrially produced and zinc coated using hot-dip galvanization. The steels were donated anonymously through the International Zinc Association. The chemical compositions and mechanical properties of all materials used can be found in Table 3.1 and Table 3.2 respectively.

Table 3.1 Compositions of LME susceptible AHSS.

Material	Coating Weight (g/m^2)		Composition (wt%)						
	Top	Bottom	C	Mn	Si	Al	Cr	Mo	Fe
DP980	60	55	0.10	2.1	0.3	0.05	0.2	0.3	Bal.
TRIP690	58	69	0.20	1.7	0.4	1.31	-	-	Bal.
TRIP1100	58	70	0.20	2.2	1.6	-	-	-	Bal.
TRIP1200	44	56	0.22	2.3	1.7	-	0.1	-	Bal.
IF Steel	64	68	-	0.1	-	0.05	0.1	-	Bal.

Table 3.2 Mechanical Properties of AHSS.

Material	Thickness (mm)	Yield Strength (MPa)	Ultimate Tensile Strength (MPa)	% Elongation
DP980	1.2	600	980	13.8
TRIP690	1.2	445	690	20.7
TRIP1100	1.6	861	1100	14.5
TRIP1200	1.6	1085	1236	15.4
IF Steel	1.5	165	305	46.0

3.2 Welding

The steel sheets were sheared into coupons with dimensions of 25 x 25 mm for the crack analysis tests and 100 mm x 25 mm for the tensile lap shear tests. In the case of the lap shear coupons, the rolling direction is along the 100 mm length of the tensile coupons. The coupon sizes used were smaller than those recommended by AWS D8.9 due to the limited supply of material. A coupon width of 25 mm was determined to be sufficient to prevent edge proximity effects because Choi *et al*. demonstrated that nugget diameters were not statistically smaller when samples were welded at least 5 mm from the sheet edge [96], a coupon width of 25 mm is sufficient to prevent edge proximity effects. All coupons were cleaned with ethanol prior to welding.

Welds were made using three different welders:

1. Medium frequency direct current (MFDC) pedestal welder with class 2, female, B-type electrode caps (Figure 3.1 a)).
2. Alternating current (AC) pedestal welder with class 2, female, B-type electrode caps.
3. FANUC 2000iC robot with a Type-C welding gun (Figure 3.1 b)).

The MFDC pedestal welder was used for all welds, unless otherwise specified. The AC pedestal welder was used to make welds of DP980 and TRIP690 at the expulsion current for the cracking quantification study (Chapter 5) because the AC welds were observed to display different patterns of LME cracking. The robot welder was used to make welds with a low current, long time pre-pulse for the study on multiple pulse welding schedules (Chapters 4 and 6).

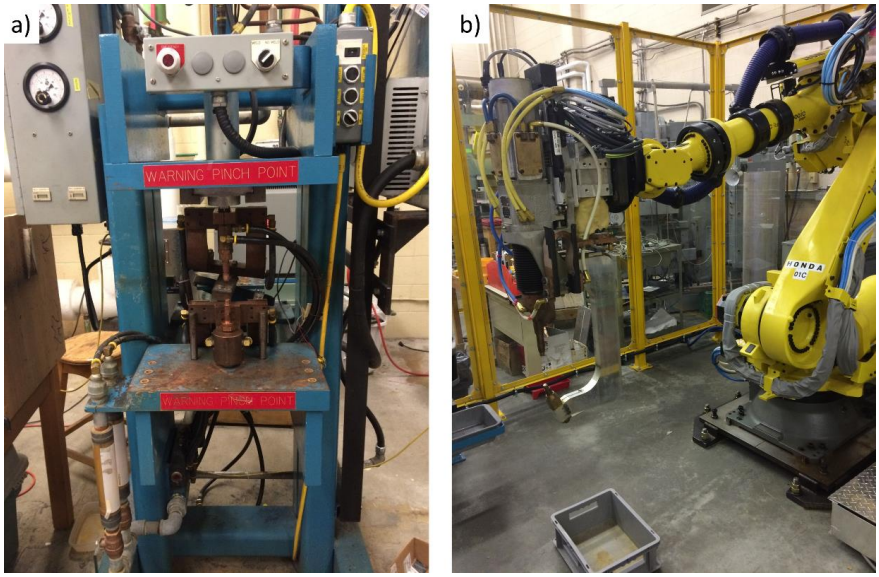

Figure 3.1 a) MFDC pedestal welder and b) FANUC 2000iC robot with Type-C welding gun.

Welds for LME studies were typically made at or up to 10% above the expulsion current to promote LME. The expulsion current, denoted as I_{max}, is defined as the minimum current for which expulsion was observed for three consecutive welds. I_{max} varies depending on the material and weld geometry. Other important welding parameters were selected according to the AWS D8.9 standard [19] and can be found in Table 3.3. Welding times are given in units of cycles (cy), a standard unit of measurement where 1 cy is equal to 16.67 ms. The length of a cycle is derived from the 60 Hz alternating current line frequency. TRIP1100 and TRIP1200 have weld times of 12-2-12 cy. This indicates that the welding schedule consists of two pulses of 12 cy each, with a cool time of 2 cy between pulses.

Table 3.3 Welding parameters recommended by AWS D8.9 [19]**.**

Material	Electrode Diameter (mm)	Force (kN)	Cooling (L/min)	Weld Time (cy)	Expulsion Current for 2-Sheet Similar Weld Geometry (kA)	Expulsion Current for 3-Sheet Dissimilar Weld Geometry (kA)
DP980	6	4.0	4	16	10.0	12
TRIP690	6	3.6	4	16	10.0	-
TRIP1100	7	5.5	6	12-2-12	10.0	13
TRIP1200	7	5.5	6	12-2-12	10.5	-

The welds for the pulse and pre-pulse welding studies (Chapters 4 and 6) were made using the 3-sheet dissimilar weld geometry shown in Figure 3.2 a) because it was observed to be highly LME susceptible. LME cracks were only measured in the AHSS sheet. In the cracking quantification study (Chapter 5), welds were made using a 2-sheet similar geometry (Figure 3.2 b)) so they could be directly compared with the results of the tensile lap shear testing.

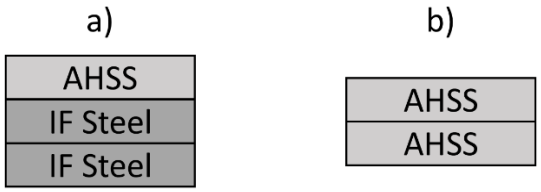

Figure 3.2 Schematics of resistance spot welds made using a) 3-sheet dissimilar and b) 2-sheet similar weld geometries.

3.2.1 Pulsed Welding Schedules

DP980 and TRIP1100 were used for the pulse study in a 3-high dissimilar weld geometry. Four different types of pulsing conditions were used for the study:

1. Short pulse followed by a long pulse.
2. Two equal length pulses.
3. Long pulse followed by a short pulse.
4. Single pulse weld (DP980 only).

The exact welding schedules used for each of the materials can be found in Table 3.4. The welding times are given in the form *x*-*y*-*z* where *x* is the weld time for the first pulse, *y* is the cool time between the pulses, and *z* is the weld time for the second pulse. Pulsing conditions were selected such that the total welding time for each welding schedule remained the same as the welding time recommended by AWS D8.9 (Table 3.3). For welding TRIP1100, a welding time of 12-2-12 cy, which is the welding schedule recommended by AWS D8.9, was used as the equal pulse welding schedule. For the other two welding schedules, the length of each pulse was varied by 2 cy to give a 10-2-14 cy and 14-2-10 cy welding schedule for the other two pulsed welding schedules. For welding DP980, a single pulse of 16 cy is recommended by AWS D8.9. For the pulsed welding schedules, a cool time of 2 cy was used, as when welding TRIP1100. The remaining welding time (14 cy) was divided in half to give an equal pulse

welding schedule of 7-2-7 cy. As with TRIP1100, the pulse lengths were varied by 2 cy each to give the remaining welding times of 5-2-9 cy and 9-2-5 cy. It was confirmed that the nugget diameters were the same between different pulsing conditions (Table 3.4) so that the effect of pulsing could be isolated from the effect of heat input.

Table 3.4 Pulsed welding schedules and associated nugget diameters for DP980 and TRIP1100.

DP980		TRIP1100	
Welding Time (cy)	**Nugget Diameter (mm)**	**Welding Time (cy)**	**Nugget Diameter (mm)**
5-2-9	6.5	10-2-14	7.3
7-2-7	6.5	12-2-12	7.3
9-2-5	6.2	14-2-10	7.5
16	6.6	-	-

3.2.2 Pre-pulse Welding Schedules

Only TRIP1100 was used for the pre-pulse welding studies, as it is the most LME susceptible of the materials tested. The recommended welding schedule from AWS D8.9 (Table 3.3) was used for all of the welds with the addition of a pre-pulse applied before the main welding pulses. A cool time of 2 cy was applied between the pre-pulse and main welding pulse. Three different pre-pulse cases were studied (Table 3.5):

1. High current, long time.
2. High current, short time.
3. Low current, long time.

Case 1 is the most extreme pre-pulse condition and was selected to minimize the zinc coating thickness in the weld area. Cases 2 and 3 were selected to reduce the zinc coating thickness without introducing too much additional heat to the weld. Note that for cases 1 and 2, the welds were made using the DC pedestal welder and for case 3, the welds were made using the DC robotic welder. The baseline (no pre-pulse) case was re-measured with the robot welder to compare against case 3.

Table 3.5 Pre-pulse welding schedules.

Case	Pre-Pulse Current (kA)	Pre-Pulse Time (cy)	Main Pulse Current (cy)	Main Pulse Time (cy)	Welder Type
1	11-17	6	13	12-2-12	Pedestal
2	17	1	13	12-2-12	Pedestal
3	4	3-12	13	12-2-12	Robot

3.3 Crack Analysis

For the pulsed welding schedule study, ten welds were made for crack analysis per condition tested. For all subsequent studies (pre-pulse and LME quantification), only five samples were welded per condition to save time and material. The welds were made using the smaller coupon size (25 x 25 mm). The weld surfaces were first examined under low (2 – 3 X) magnification and any visible surface cracks were identified. Samples were then cross-sectioned across the weld diameter to measure the depth and frequency of cracks for each weld. The cross-section direction was selected to pass through the most severe surface cracks (Figure 3.3 a)). After cross-sectioning, the welds were mounted, polished to a 1 µm diamond finish, and etched with 5% nital. Following metallographic preparation, micrographs were taken of any LME cracks in the cross-section using an Olympus BX51M optical microscope. The cracks were measured with a straight line from the crack opening to the crack tip, as shown in Figure 3.3 b), using the open source software ImageJ. Only cracks larger than 5 µm were considered. LME cracking severity was quantified using three of the cracking metrics seen in literature (see Section 2.5.4): arithmetic mean (mean) crack length, number of cracks per weld, and 95^{th} percentile crack length. 95^{th} percentile crack length was selected as an alternative to maximum crack length to prevent inclusion of outliers.

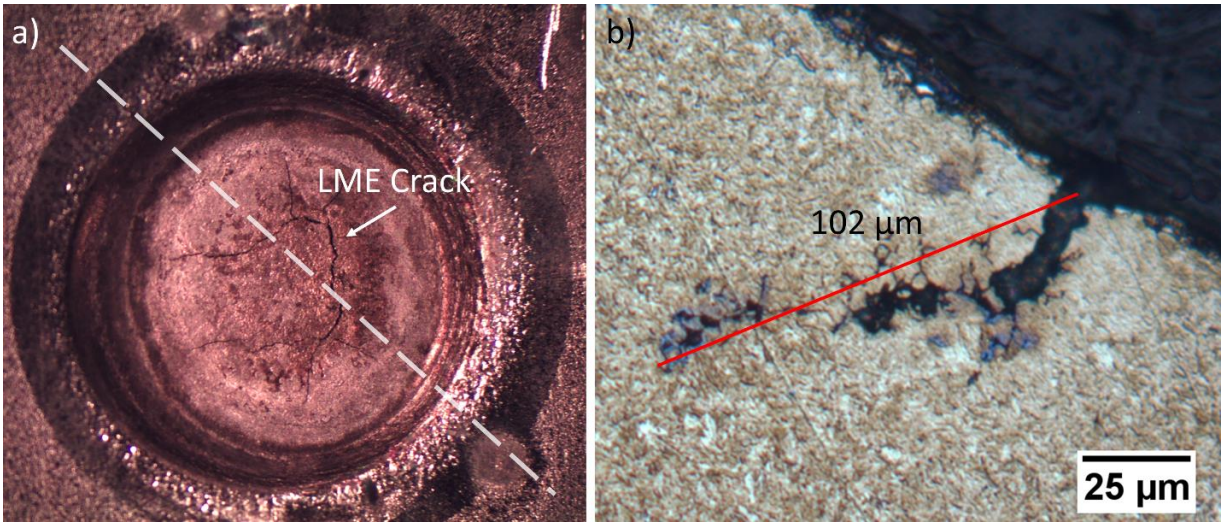

Figure 3.3 a) Selection of cross-section plane using visible surface cracks and b) measurement of LME crack lengths [90]**.**

3.4 Tensile Testing

Tensile lap shear testing is a standard method used for assessing weld strength. The impact of LME cracking on weld strength was measured by calculating the percent difference in strength between welds of zinc coated (LME susceptible) and uncoated (LME free) material as follows:

$$Strength\ Loss = \frac{F_{uncoated} - F_{coated}}{F_{uncoated}} \times 100 \tag{3.1}$$

where *F* represents the maximum load measured by the tensile test.

Tensile lap shear samples were welded in the 2-sheet similar weld geometry shown in Figure 3.4. The overlap of the sheets meets the minimum overlap for tensile lap shear testing recommended by Zhou *et al* [97]. Five samples were welded using coated and uncoated steel for each welding condition. The uncoated material was obtained by stripping the zinc coating from experimental materials by soaking them in a solution of 20% HCl prior to welding. Welding currents were selected such that the nugget diameter was the same between the coated and uncoated samples. This ensures that any strength difference is due to LME and not to a change in nugget diameter [17]. Tensile testing was conducted without shims using an Instron Model 4206 tensile tester (Figure 3.5) at a rate of 2 mm/min.

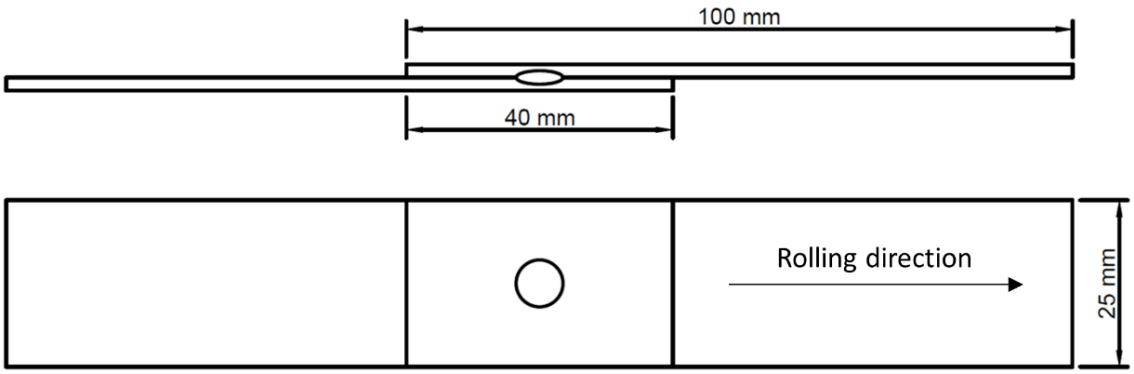

Figure 3.4 Tensile lap shear coupon geometry [90]**.**

Figure 3.5 Instron Model 4206 tensile tester.

3.5 Nugget Diameter Measurements

Nugget diameter measurements were used to estimate differences in heat input between welding conditions and to ensure that strength loss is due to LME cracking (refer to Sections 3.2.1 and 3.4). To determine nugget diameter, welds were first cross-sectioned through the diameter of the weld using an

Accuton-50 precision cutting saw. The cross-sections were mounted, polished to a 1 µm diamond finish, and etched with 5% nital. The nugget diameter was measured in ImageJ by drawing a line across the nugget, as shown in Figure 3.6.

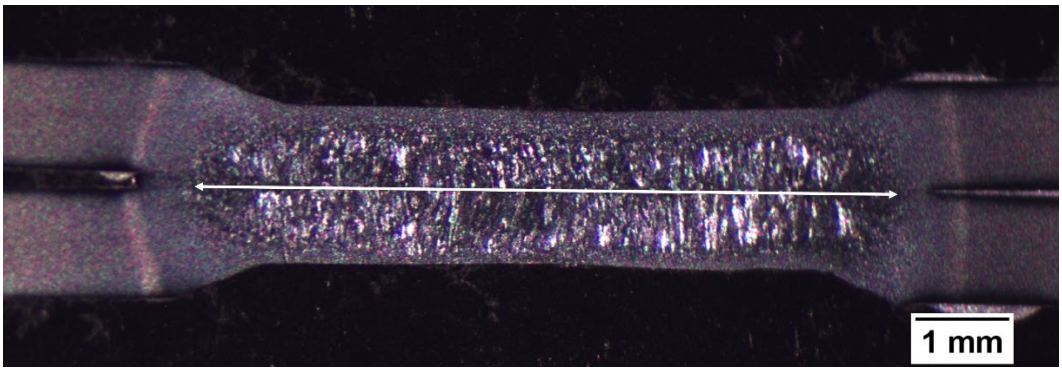

Figure 3.6 Measurement of nugget diameter.

3.6 Statistical Analysis

There will be uncertainty (error) associated with any quantity measured by experimentation. Statistical analysis is a necessary step to determine whether the results are significant. The statistical significance of the results was assessed using confidence intervals and significance testing. Linear regression analysis was also used in the LME quantification study (Chapter 5) to quantify the relationship between LME cracking and weld performance.

3.6.1 Error Calculations

To calculate the uncertainty associated with the percent difference in tensile strength, the standard deviations associated with the peak loads obtained for the welds of zinc coated and uncoated material were calculated and standard error propagation techniques were applied as follows:

$$\sigma_{Strength\ Loss} = |Strength\ Loss| \sqrt{\left(\frac{\sigma_{coated}}{F_{coated}}\right)^2 + \left(\frac{\sigma_{uncoated}}{F_{uncoated}}\right)^2} \tag{3.2}$$

where σ is standard deviation and |*Strength Loss*| is the absolute value of the percent difference in weld strength, calculated using Equation 3.1 [98].

For some quantities, such as 95th percentile crack length or median crack length, it is difficult to obtain a standard deviation analytically. Therefore, a numerical method, known as the bootstrap method,

was applied to calculate an approximation of the standard deviation [99]. In this method, a random sample, called a bootstrap sample, is taken from the total population. The bootstrap sample contains the same number of measurements as the total population and is sampled with replacement. With replacement means that a given measurement in the population may be included in a bootstrap sample more than once. The test statistic (ex. median) is calculated for the bootstrap sample. This process was repeated for 10,000 iterations. The estimate of the standard deviation for the entire population is calculated by taking the standard deviation of the 10,000 measurements of the test statistic in the bootstrap samples. A MATLAB function was written to implement the bootstrap method (Appendix A).

All error bars on graphs represent 95% confidence intervals, which were calculated using the equation

$$X \pm 1.96\frac{\sigma}{\sqrt{N}} \tag{3.3}$$

where X is the measured quantity and N is the number of measurements [100].

3.6.2 Significance Testing

A common method for determining whether the difference between two means is significant is the Student's t-test. When comparing more than two means, each possible pair of means can be compared using the t-test. However, there are two major disadvantages with this approach. Firstly, it is computationally expensive, particularly if there are a large number of comparisons. Secondly, if each test is performed at a significance level α, the overall significance of the all the tests, α', may be much greater than α. α' has an upper bound given by Bonferroni's inequality:

$$\alpha' \leq 1 - (1 - \alpha)^c \tag{3.4}$$

where c is the number of comparisons [100]. For instance, when comparing 5 different means, 10 individual comparisons can be made. Using a significance level of α=0.05 for the individual comparisons, the overall significance of the test may be as high as α'=0.40.

Instead, multiple means can be compared using the least significant difference (LSD) method. The significance level for the individual comparisons is selected using Bonferroni's correction:

$$\alpha = \frac{\alpha'}{c} \tag{3.5}$$

where α' is the desired upper bound for the overall significance . The least significant difference is then calculated as follows:

$$LSD = t_{DF,\alpha/2}\sqrt{\frac{2\sigma^2}{N}} \tag{3.6}$$

where *DF* is the number of degrees of freedom [100]. If the difference between two means is greater than the LSD, the difference is significant. In this work, the LSD is always calculated using an overall significance of α'=0.05.

3.6.3 Linear Regression Analysis

For the LME quantification study (Chapter 5), linear regression analysis was conducted using OriginPro 2017. The statistical significance of the model was tested using the analysis of variance (ANOVA) method and correlation coefficients (R^2) [100].

Chapter 4
Effect of Multiple Pulse Weld Schedules on LME Severity

Two different types of multiple pulse welding schedules have been proposed to suppress LME in RSW of AHSS: pulsing during the main welding current (pulsed welding) and applying a pre-pulse before the main welding current (pre-pulse welding). However, further study is needed to fully explore the effect these schedules have on LME severity. In this chapter, two studies are presented that aim to further develop these two methods for LME suppression.

4.1 Effect of Pulsed Welding Schedules

Ashiri *et al*. determined that LME cracking could be reduced using a two pulse welding schedule [43]. However, the nugget diameter was not kept constant between the welding schedules, meaning that the effect of pulsing cannot be isolated from the effect of heat input. This section details a revised version of Ashiri's study, in which the nugget diameter is kept constant (Table 3.4).

TRIP1100 and DP980 were used for this study. Ten welds were made for each pulsing condition. All welds were made using the 3-sheet dissimilar weld geometry (Figure 3.2 a)) at the expulsion current using the MFDC pedestal welder. The samples were analyzed using the method described in Section 3.3. Cracking severity is quantified in terms of mean crack length, number of cracks per weld, and 95th percentile crack length.

4.1.1 Single vs. Double Pulse Welds

LME cracking severity was compared between welds of DP980 made using single and double pulse welding schedules. It was expected that the double pulse weld would show a reduction in LME cracking compared to the single pulse weld because Ashiri *et al.* observed that switching from a single to double pulse eliminated LME cracking in the shoulder in an electrogalvanized TWIP steel [43]. Using SORPAS modelling, Ashiri concluded that this was due to a reduced temperature in the shoulder, which was termed the "supercritical LME area," reducing the amount of liquid zinc present for LME. The model also showed reduced tensile stress in this area.

In general, using a double pulse welding schedule reduced LME cracking severity, as expected. In particular, the average number of cracks per weld has been considerably reduced by using a double

pulse welding schedule (Figure 4.1 b)). However, the error bars on the graphs in Figure 4.1 are quite large and many of them are overlapping, which indicates that the differences are not statistically significant.

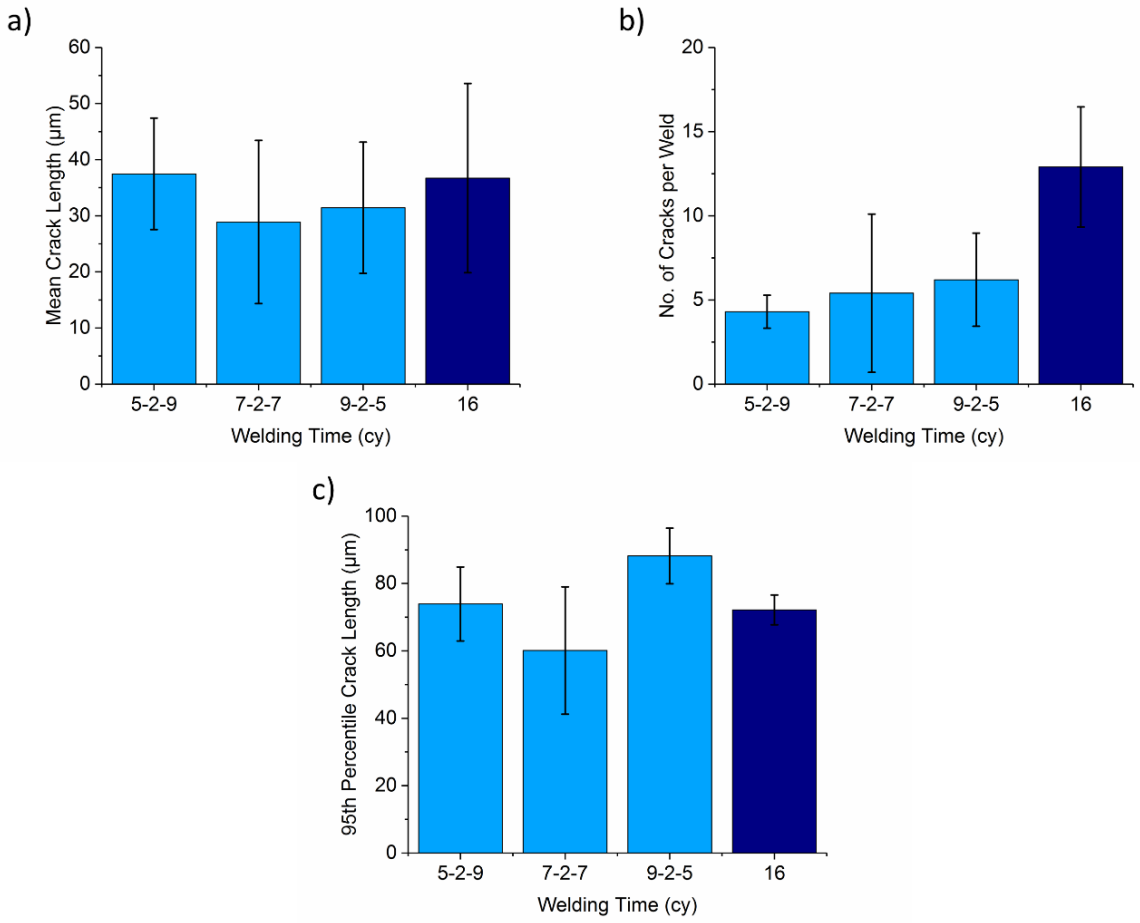

Figure 4.1 Comparison of a) mean crack length, b) number of cracks per weld, and c) 95th percentile crack length for DP980 welded with different pulsing conditions.

The significance of the results was assessed using the least significant difference (LSD) method described in Section 3.6.2. Recall that if the difference between two means is less than the LSD, that difference is not significant. The test was performed at an overall significance level of α'=0.05 and the Bonferroni correction was used to determine the significance level for the individual comparisons. In this case, the LSD was calculated using a significance level of α=0.01 for the individual comparisons. The results of the LSD calculation are given in Table 4.1. Unfortunately, for all three metrics, the differences between the pulsing conditions are not significant. The only exception is the difference in number of cracks between welds made with one of the double pulse schedules (5-2-9 cy) and welds made with a

single pulse schedule. This means that no conclusions can be drawn regarding the effect of using a double pulse welding schedule on LME severity in DP980 from these cracking metrics due to their large standard deviations. The large errors associated with the cracking metrics may indicate that they are not precise enough to evaluate crack severity.

Table 4.1 LME cracking measurements and LSD for DP980 welded with different pulsing conditions.

Welding Time (cy)	Mean Crack Length (μm)	Avg. No. of Cracks	95th Percentile Crack Length (μm)
5-2-9	37.5	4.3	73.9
7-2-7	28.9	5.4	60.1
9-2-5	31.4	6.2	88.2
16	36.7	12.9	72.1
LSD	**33.6**	**8.6**	**31.5**

Since using typical cracking metrics was shown to be ineffective in quantifying differences in LME, instead the total populations of cracks were observed to get a more complete picture of LME cracking in the welds. The majority of cracks in all welds are small, resulting in a peak in the crack distribution. The peak represents the most frequently observed crack length. The shapes of the distributions for all four pulsing conditions are very similar, with the most frequent crack lengths observed in the range of 10 – 15 μm. This explains why there was not a statistically significant difference in the mean crack lengths. However, although the most commonly observed crack lengths are approximately the same, there is a difference in how many cracks of this length are observed. The single pulse welds have more cracks of this length than the welds made using double pulse welding schedules, shown by the higher peak in Figure 4.2 a).

Similarly, when looking at the total crack distribution in Figure 4.2 b), the single pulse condition shows much larger numbers of cracks than the double pulse conditions, particularly in the 0 – 50 μm range. Few cracks larger than 100 μm were observed for any of the conditions; only a few scattered cracks can be observed at the higher crack lengths. Therefore, it can be concluded that the single pulse weld demonstrates more severe LME cracking than the double pulse welds, as indicated by the larger number of cracks.

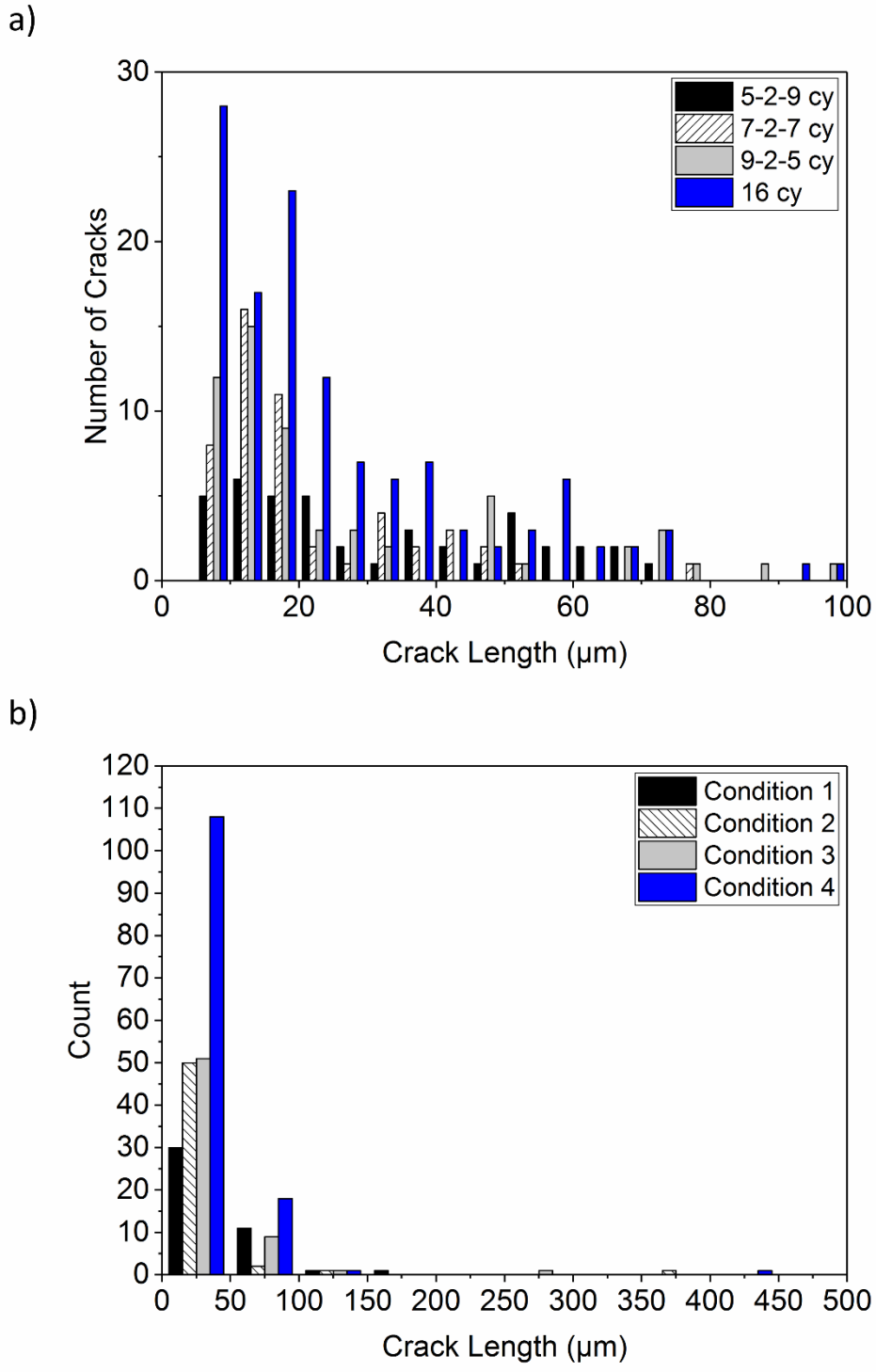

Figure 4.2 Histograms for all crack lengths measured in the range of a) 0 - 100 μm and b) 0 - 500 μm for DP980 welded with different pulsing conditions.

4.1.2 Effect of Changing Pulse Lengths

Since using a double pulse welding schedule was able to reduce LME severity, further study was conducted on different types of double pulse welding schedules to determine if further reductions in LME cracking are possible. The effect of changing pulse lengths within a double pulse weld is somewhat more difficult to predict than the difference between a single and double pulse weld. Ashiri *et al.* compared several different pulsed welding schedules and were able to obtain LME free welds using a welding schedule with a long pulse followed by a short pulse (12-1-3 cy) [43]. This type of welding schedule was able to form LME free welds over a larger current range (which Ashiri referred to as the "weldable current range") because it had the slowest rate of nugget growth. Conversely, a welding schedule consisting of a short pulse followed by a long pulse (3-1-12 cy) had a smaller weldable current range. However, in Ashiri's study, the 3-1-12 cy welding schedule also resulted in a higher heat input because he used a higher current for the second pulse than the first. To isolate the effect of heat input from the effect of pulsing, this study investigates the LME severity in welds made with different double pulse welding schedules but the same nugget diameter.

The effect of changing pulse lengths are slightly different for the two materials tested. In welds of DP980, the three cracking metrics were not significantly different in welds made with the three different double pulse welding schedules (Figure 4.1). Therefore, conclusions must be made using the total crack distributions, rather than the mean values. When looking at the distribution of short cracks in Figure 4.2 a), it can be seen that the number of cracks observed at the most frequent crack length (10 – 15 μm) is lower for the 5-2-9 cy welds than for the welds made using the other two double pulse schedules (7-2-7 and 9-2-5 cy). Since all of the double pulse welds have approximately the same total number of cracks per weld (Figure 4.1 b)), the presence of fewer small cracks indicates that the 5-2-9 cy welds must have a greater proportion of larger cracks. This is confirmed by the total distribution of cracks (Figure 4.2 b)), in which the 5-2-9 cy welds have the lowest number of cracks in the 0 – 50 μm range and the largest number in the 50 – 100 μm range out of the three double pulse welds. This suggests that the 5-2-9 cy welding time yielded the most severe LME cracking, but there is no significant difference in LME between the other two double pulsing welding schedules. This is consistent with the study by Ashiri *et al*, who also observed that LME cracking was more severe with welding schedules consisting of a short pulse followed by a long pulse.

When studying welds of TRIP1100, it is again difficult to determine which condition performed the best according to the typical cracking metrics (Figure 4.3). Calculating the LSD (using a significance level of α=0.02 for the individual tests in this case) showed the differences in the cracking metrics are mostly not statistically significant (Table 4.2). However, unlike DP980, the differences in the 95th percentile crack length are significant for TRIP1100. This is likely because large cracks are more consistently observed for TRIP1100.

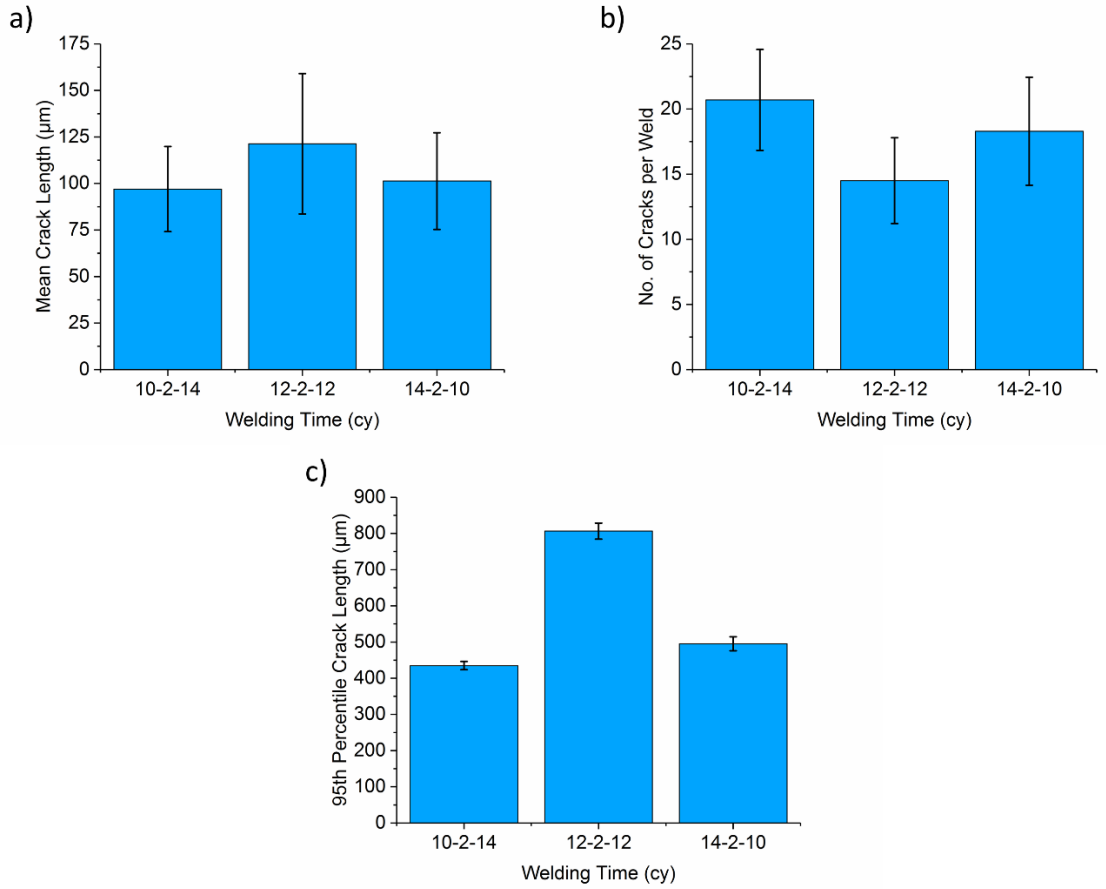

Figure 4.3 Comparison of a) mean crack length, b) number of cracks per weld, and c) 95th percentile crack length for TRIP1100 welded with different pulsing conditions.

Table 4.2 LME cracking measurements and LSD for TRIP1100 welded with different pulsing conditions.

Welding Time (cy)	Mean Crack Length (μm)	Avg. No. of Cracks	95th Percentile Crack Length (μm)
10-2-14	97.0	20.7	434.7
12-2-12	121.3	14.5	806.6
14-2-10	101.3	18.3	495.0
LSD	**61.0**	**8.3**	**37.4**

Using the crack distributions to assess LME cracking severity in TRIP1100, there is a difference in the most frequent crack length observed. Using the 12-2-12 and 14-2-10 cy welding times, the most common crack lengths observed are between 25 and 30 μm, while cracks are most commonly observed in the 45 – 50 μm range when welding with the 10-2-14 cy schedule (Figure 4.4 a)). This can also be seen in Figure 4.4 b), where the 10-2-14 cy welds have a greater number of cracks in the range of 50 – 150 μm than the other two conditions. Because of this, it can be concluded that, similar to DP980, the 10-2-14 cy welding time yielded the most severe LME, but it is difficult to make conclusions regarding the other two conditions. The 14-2-10 cy welds have the most cracks on average (although recall that this difference is not statistically significant) but cracks are not as long, demonstrated by the shorter 95th percentile crack length (Figure 4.3 c)).

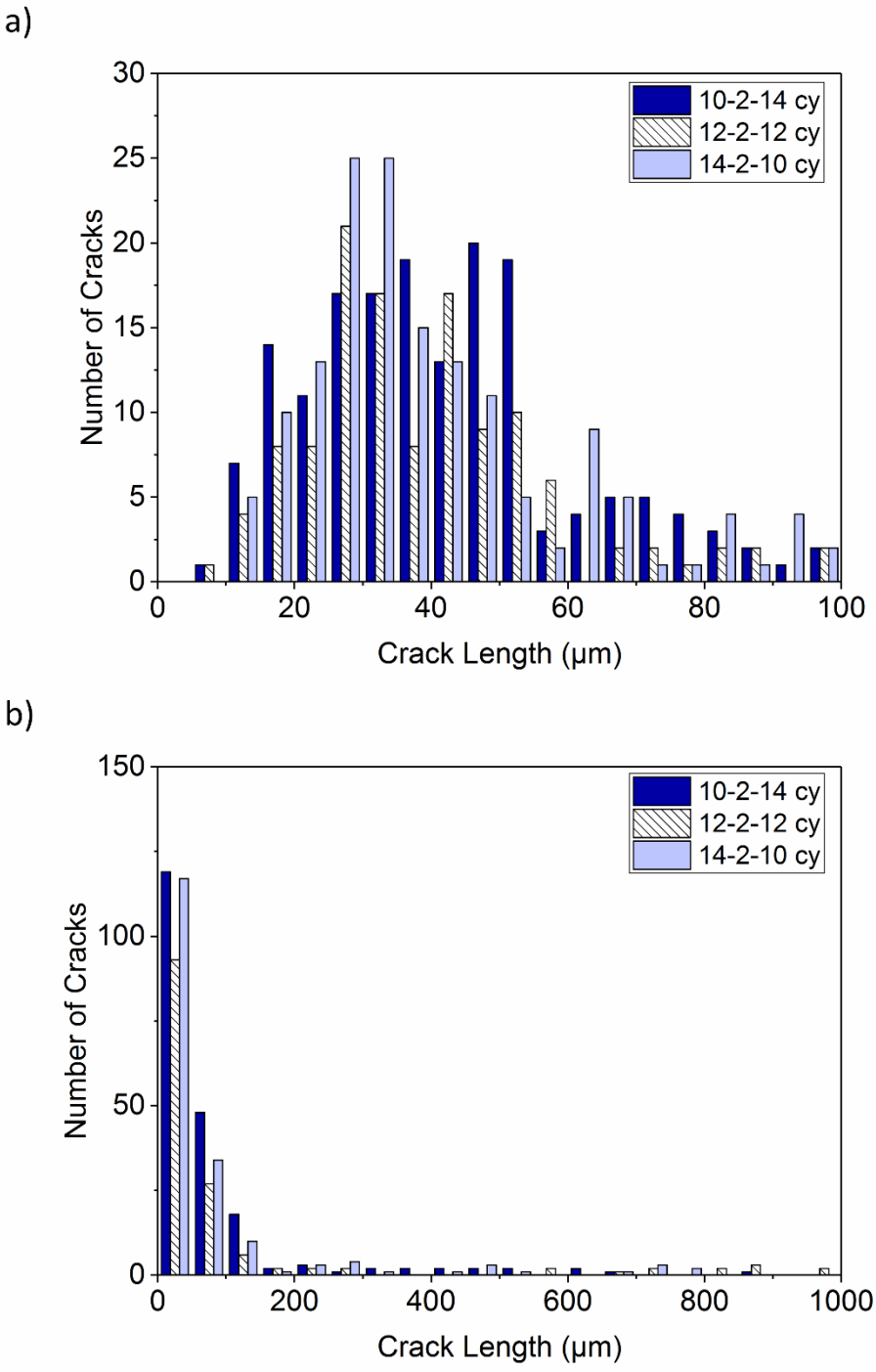

Figure 4.4 Histograms for all crack lengths measured in the range of a) 0 - 100 μm and b) 0 - 1000 μm for TRIP1100 welded with different pulsing conditions.

4.2 Effect of Pre-Pulse Welding Schedules

For this portion of the study, only TRIP1100 was used because it is the more LME susceptible of the two materials. Five welds were made with the MFDC pedestal welder using the 3-sheet geometry using the expulsion current and the standard welding schedule in Table 3.3. The last set of pre-pulse welds (low current, long time pre-pulse) were made using the DC robotic welder. The pre-pulses were applied 2 cy before the main welding current. Again, the LME cracking in the samples was analyzed according to Section 3.3. Note that a pre-pulse of zero refers to the standard welding schedule with no pre-pulse applied.

It was expected that the addition of a pre-pulse would cause a reduction in LME severity in the welds. Kim *et al*. demonstrated that applying a pre-pulse could reduce LME cracking or even eliminate it completely in RSW of galvannealed TRIP590 [11]. The pre-pulse was intended to melt the zinc coating and remove it from the weld area prior to application of the main welding current. Kim *et al*. tested only two different pre-pulse conditions. This study was intended to determine the optimum pre-pulse conditions for reduction of LME in TRIP1100 spot welds.

4.2.1 Effect of Pre-Pulse on LME Cracking

For welds made using welding schedules with a 6 cy pre-pulse, the LSD analysis (using a significance level of α=0.005 in this case) shows that there is not a statistically significant difference in mean crack length or number of cracks per weld as the pre-pulse current is increased (Table 4.3). However, applying a pre-pulse current of 11 to 15 kA did cause a reduction in 95^{th} percentile crack length (Figure 4.5). Due to the lack of statistical significance, the only conclusion that can be made is that for 2 out of 3 of the LME metrics, applying a 6 cy pre-pulse does not cause a significant improvement in LME severity.

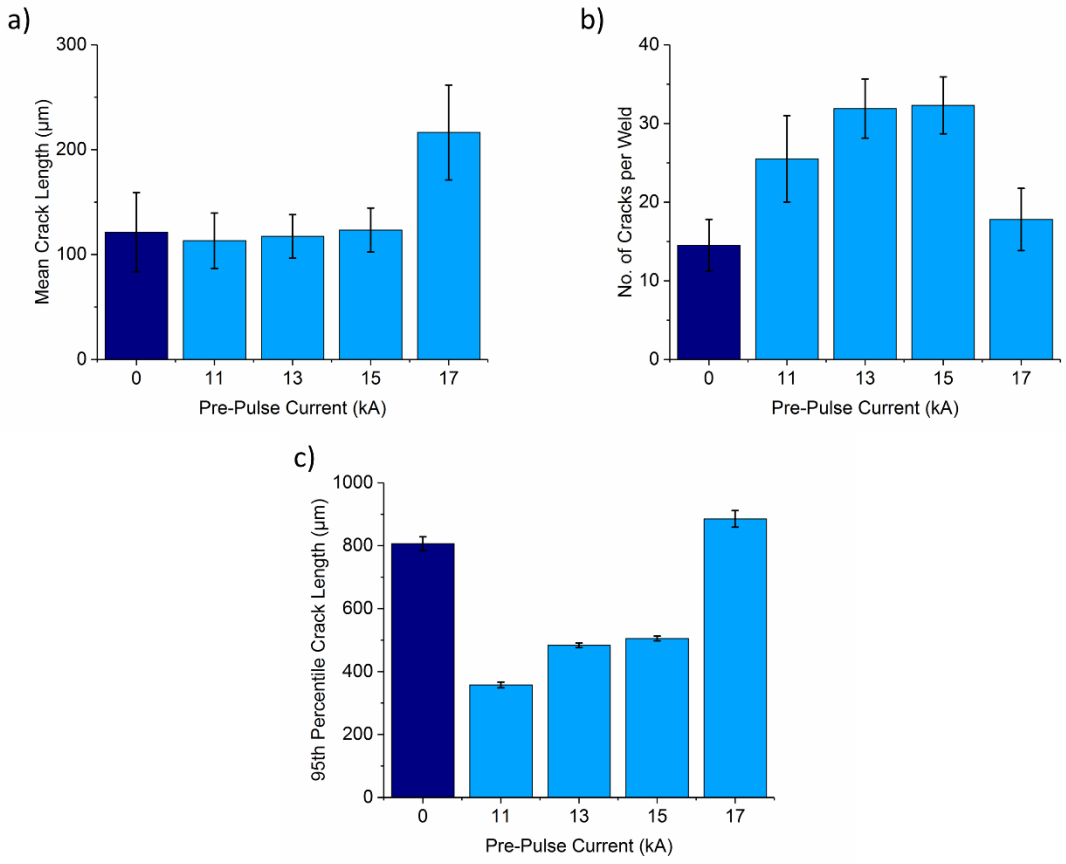

Figure 4.5 Comparison of a) mean crack length, b) number of cracks per weld, and c) 95th percentile crack length for TRIP1100 welded with 6 cy pre-pulses of different currents.

Table 4.3 LME cracking measurements and LSD for TRIP1100 welded with 6 cy pre-pulses of different currents.

Pre-Pulse Current (kA)	Mean Crack Length (µm)	Avg. No. of Cracks	95th Percentile Crack Length (µm)
0	121.3	14.5	806.6
11	113.2	25.5	357.4
13	117.3	31.9	483.3
15	123.4	32.3	505.2
17	216.4	17.8	885.2
LSD	**101.8**	**13.8**	**53.2**

On average, it seems that LME becomes more severe as the pre-pulse current is increased, even though the zinc coating is reducing. This is likely due to the increase weld heat. It has been well documented that increasing heat to the weld worsens LME cracking [10,11,16,43,69]. This is also consistent with the study by Kim *et al*., which showed that when the pre-pulse current was too high, there was no improvement in LME severity in the weld [11]. This indicates that to use the pre-pulse method, one must find a balance between coating removal and heat input.

To melt the zinc coating while still minimizing the amount of heat introduced to the weld, a pre-pulse with high current applied over a short time was selected. Therefore, pre-pulse currents of 17 kA with lengths of 1, 2, 4, and 6 cy were tested next. Before cross-sectioning, the length of visible surface cracks were first measured. While this is not ideal, since not all cracks are visible on the surface, it is a useful screening test because the normal crack analysis method that is quite time consuming. The average surface crack length for most of the pre-pulse conditions is longer than for the standard welding schedule condition. However, for the 17 kA, 1 cy pre-pulse, there was a slight reduction in average surface crack length, so these samples were cross-sectioned and used for more detailed LME analysis (Figure 4.6).

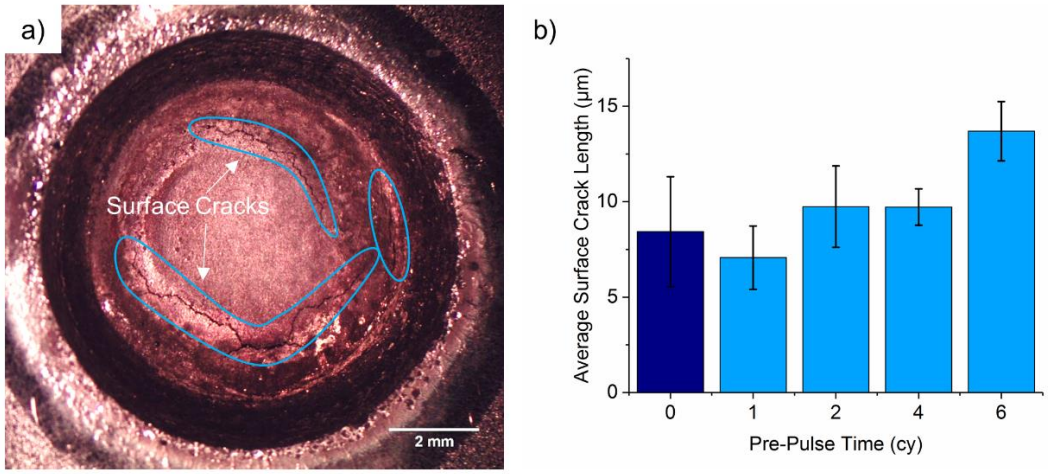

Figure 4.6 a) Surface cracks and b) average surface crack length in TRIP1100 welded with 17 kA pre-pulses of different lengths.

For welds made using a 17 kA, 1 cy pre-pulse, two out of three of the cracking metrics again showed no reduction in LME with the applied pre-pulse (Figure 4.7). Since there is only one comparison in this case, a standard t-test using α=0.05 can be used instead of the LSD method. According to the t-test, there is no statistical difference in mean crack length or number of cracks per weld between the welds

made using the standard welding schedule and the welds made with the 17 kA, 1 cy pre-pulse. There is a significant decrease in 95th percentile crack length when the pre-pulse is added but overall, the pre-pulse does not appear to reduce LME severity.

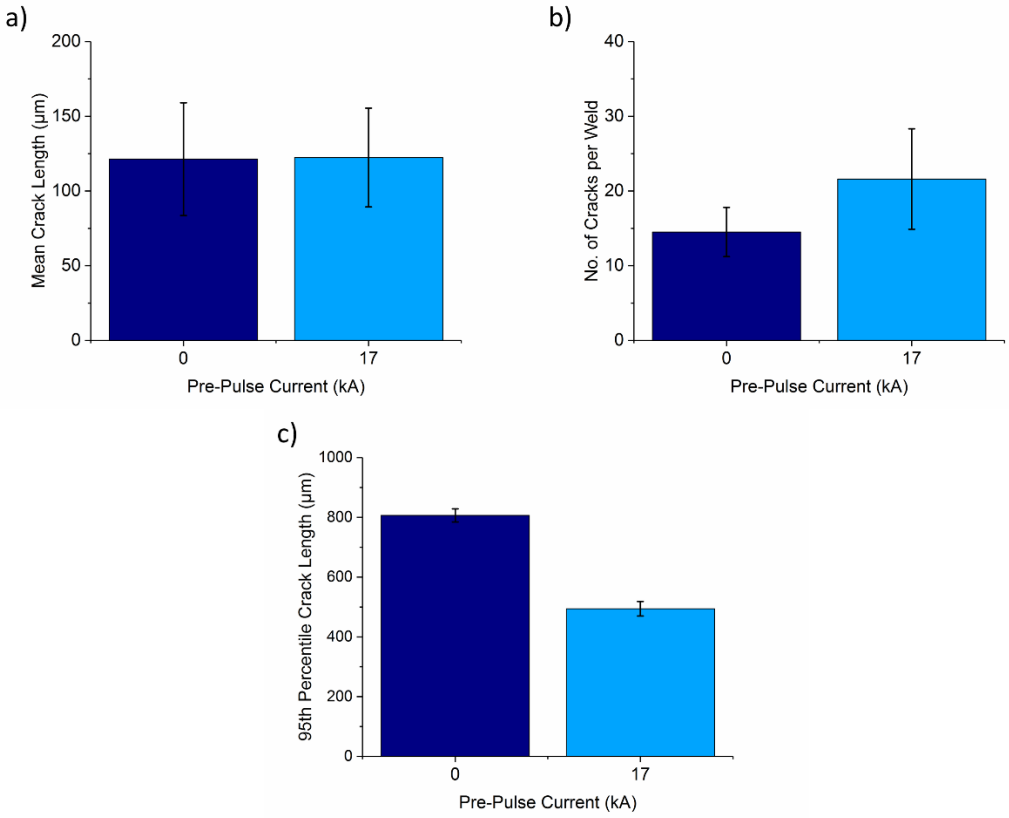

Figure 4.7 Comparison of a) mean crack length, b) number of cracks per weld, and c) 95th percentile crack length for TRIP1100 welded with and without 17 kA, 1 cy pre-pulse.

Since the 17 kA, 1 cy pre-pulse did not significantly reduce LME cracking, a low current over a longer time was tested next. 4 kA was selected as the pre-pulse current, as it was the lowest current the welder was able to output. Recall that the robotic welder was used to make the welds for this portion of the study. Three different pre-pulse times were used (3, 6, and 12 cy). In this case, welds made using all three 4 kA pre-pulse conditions showed no improvement in LME cracking compared to the standard weld for all three cracking metrics (Figure 4.8). The welds made using a 4 kA, 3 cy pre-pulse had fewer cracks per weld on average compared to the standard weld and the welds made using a 4 kA, 6 cy pre-pulse had a lower 95th percentile crack length, but the LSD analysis (using a significance level of α=0.01 for the individual tests in this case) showed that these differences were not significant (Table 4.4).

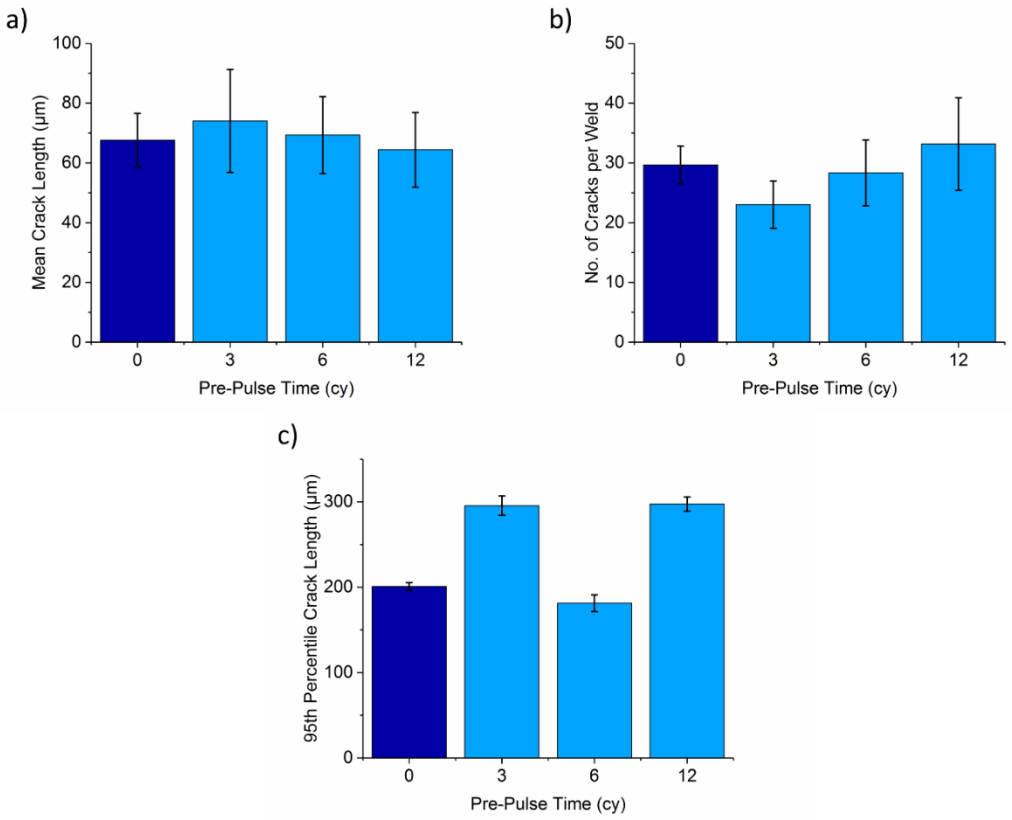

Figure 4.8 Comparison of a) mean crack length, b) number of cracks per weld, and c) 95th percentile crack length for TRIP1100 welded with 4 kA pre-pulses of different lengths.

Table 4.4 LME cracking measurements and LSD for TRIP1100 welded with 4 kA pre-pulses of different lengths.

Pre-Pulse Time (cy)	Mean Crack Length (µm)	Avg. No. of Cracks	95th Percentile Crack Length (µm)
0	67.6	29.7	200.8
3	74.0	23.0	295.5
6	69.3	28.3	181.3
12	64.4	33.2	297.6
LSD	**34.9**	**15.4**	**104.1**

4.3 Summary and Further Work

The use of multiple pulse welding schedule to reduce LME severity in resistance spot welds of DP980 and TRIP1100 was evaluated. Mean crack length, number of cracks per weld, 95th percentile crack length, and histograms of the crack populations were used to evaluate the LME severity in the welds.

The investigation of the effect of pulsing on LME severity yielded mixed results. Changing from a single to a double pulse welding schedule reduces LME severity, but the impact of changing the pulse lengths is unclear. Based on the crack length distributions, welding schedules consisting of a short pulse followed by a long pulse (5-2-9 cy for DP980 and 10-2-14 cy for TRIP1100) showed the greatest LME severity, but no conclusions could be made regarding the effect of the other two pulsing conditions.

The application of a pre-pulse does not appear to be an effective method for reduction of LME in RSW. In order to successfully use the pre-pulse method, a balance must be found between coating reduction and heat input. None of the pre-pulse conditions tested were able to significantly reduce LME in TRIP1100 welds according to the three cracking metrics used.

Forming conclusions from the three cracking metrics (mean crack length, number of cracks per weld, and 95th percentile crack length) was difficult because of the lack of statistically significant differences between conditions. This is due to the large confidence intervals of the average lengths and numbers of cracks observed in LME susceptible welds. This suggests that these commonly used cracking metrics may not be the best method for quantifying LME cracking in resistance spot welds.

Chapter 5
LME Quantification and Relationship with Weld Performance

In the previous chapter it was shown that LME cracking is not effectively quantified using typical cracking metrics (mean crack length, number of cracks per weld, and 95th percentile crack length) due to their large uncertainty. This chapter explores alternative methods of crack quantification.

All four grades of AHSS (DP980, TRIP690, TRIP1100, and TRIP1200) were used in this study to ensure that the quantification methods studied are applicable to different materials with different LME susceptibilities. Welds of each material were made using the standard welding schedule described in AWS D8.9 (see Table 3.3) at a current 10% above the expulsion current (I_{max}+10%). Following this, samples of TRIP1100 and TRIP1200 were also welded with currents between I_{max} and I_{max}+10% to vary the amount of LME cracking. Additional DP980 and TRIP690 samples were also welded at I_{max} with the AC pedestal welder because the AC welds display different patterns of LME cracking. Five samples were welded per condition using a two high similar geometry (Figure 3.2 b)) and the LME cracking severity was assessed as per Section 3.3. Tensile lap shear samples were made using the same welding parameters according to the method described in Section 3.4. The LME severity was related to the percent difference in strength by performing linear regression analysis. ANOVA tables for the linear regressions can be found in Appendix B.

5.1 Crack Analysis

The four materials tested displayed different patterns of crack susceptibility. Very few cracks were observed in DP980 and those that were seen tended to be small (Figure 5.1 a, b)). Few cracks were also observed in TRIP690 (Figure 5.1 c)), but there were some very large cracks in the center of the weld area (Figure 5.1 b)). In TRIP1100, large cracks were observed in the center of the weld (Figure 5.1 e)) and many small cracks were also observed in the shoulder (Figure 5.1 f)). TRIP1200 had a large number of cracks, which were mostly small and located in the weld shoulder (Figure 5.1 h)).

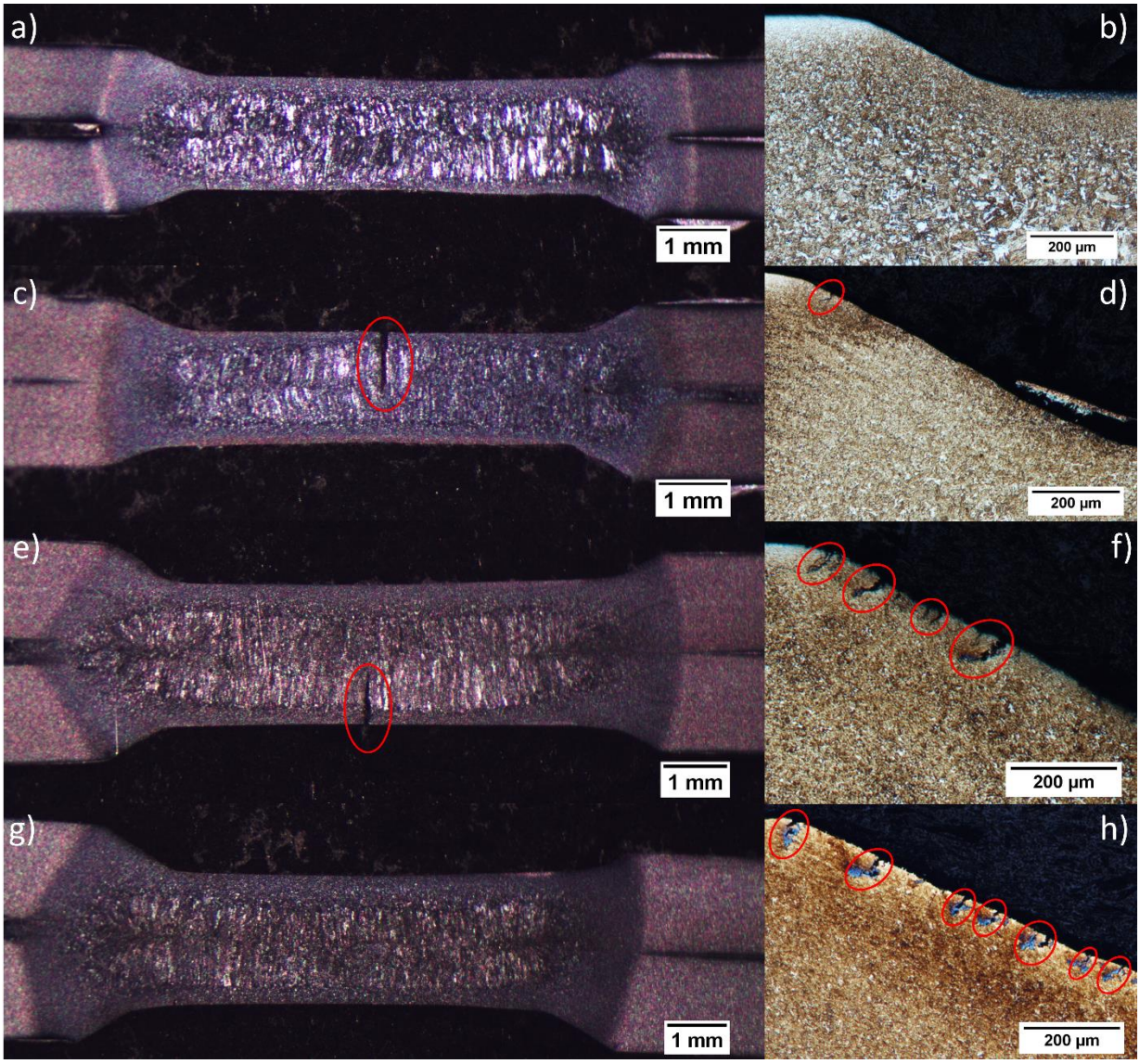

Figure 5.1 Micrographs of resistance spot welds of DP980 (a, b), TRIP690 (c, d), TRIP1100 (e, f), and TRIP1200 (g, h) welded at I_{max}+10%. LME cracks are circled [90].

Similar to the analysis carried out in Chapter 4, it is very difficult to make any conclusions regarding which material displayed the most severe LME cracking using the three typical cracking metrics (mean crack length, number of cracks per weld, 95th percentile crack length). The large and overlapping error bars show that there is not a statistically significant difference between welds of different materials (Figure 5.2). This is particularly clear when observing mean crack length, where TRIP690 has such a large 95% confidence interval that there is no clear difference between it and any of

the other materials (Figure 5.2 a)). This was confirmed by calculating the LSD using the method described in Section 3.6.2. Recall that the calculations were performed with an overall significance level of α'=0.05 and the Bonferroni correction was used to determine the significance level for the individual comparisons. In this case, the significance level used was α=0.01. The differences in 95th percentile crack length are significant (except for the difference between TRIP1100 and TRIP690) and TRIP1200 has a significantly larger number of cracks than DP980 and TRIP690. All other differences are not significant (Table 5.1).

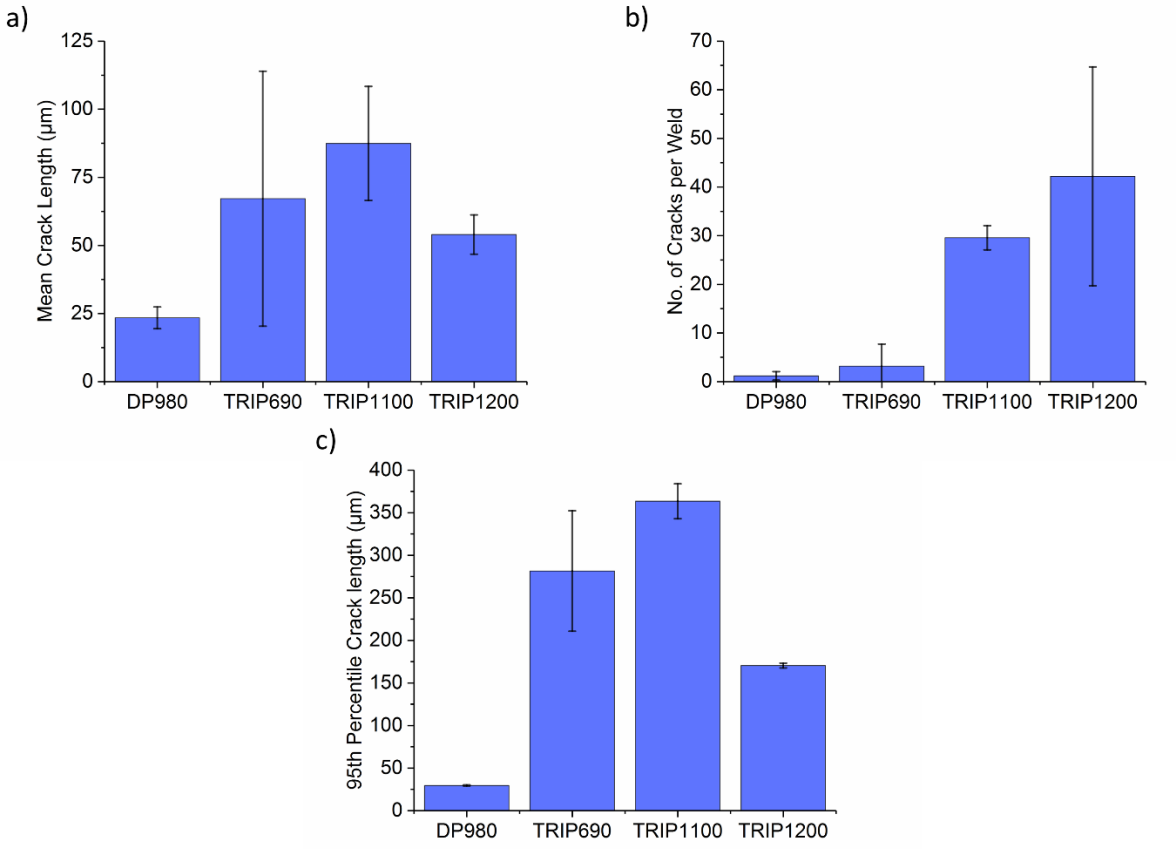

Figure 5.2 Comparison of a) mean crack length, b) number of cracks per weld, and c) 95th percentile crack length in samples of AHSS welded at I_{max}+10% [90]**.**

Table 5.1 LME cracking measurements and LSD for AHSS welded at I_{max}+10%.

Material	Mean Crack Length (μm)	Avg. No. of Cracks	95th Percentile Crack Length (μm)
DP980	23.4	1.2	29.6
TRIP690	67.2	3.2	281.6
TRIP1100	87.4	29.6	363.5
TRIP1200	54.0	42.2	170.5
LSD	**68.6**	**29.4**	**96.5**

Even excluding the lack of statistical significance, it would be difficult to make any conclusions regarding which material is the most LME susceptible. The three crack metrics do not show the same trend in cracking severity. If observing only mean crack length or 95th percentile crack length, one would conclude that TRIP1100 is the most LME susceptible. Observing only number of cracks, on the other hand, would lead to the conclusion that TRIP1200 is the most LME susceptible. This is consistent with the micrographs in Figure 5.1; TRIP1100 had very large cracks, while TRIP1200 had the largest number of cracks (although they were small). This suggests that using a single one of these crack metrics is not enough to give a complete picture of LME cracking severity.

5.2 Tensile Lap Shear Testing

In addition to quantifying LME cracking with low uncertainty, an ideal cracking quantification metric should also be able to predict weld performance. The results of the tensile lap shear testing revealed that the difference in strength between welds of zinc coated (LME susceptible) and uncoated (LME free) material varies depending on the material and welding current. For instance, for welds made with a current of I_{max}+10%, TRIP1100 and TRIP1200 show a significant loss of strength in the LME affected welds (43% and 32% difference in strength, respectively), while LME had almost no effect on the weld strength in DP980 and TRIP690 (Figure 5.3). The nugget diameters of the welds of coated and uncoated material were similar (Table 5.2), confirming that the loss in strength is due to LME cracking.

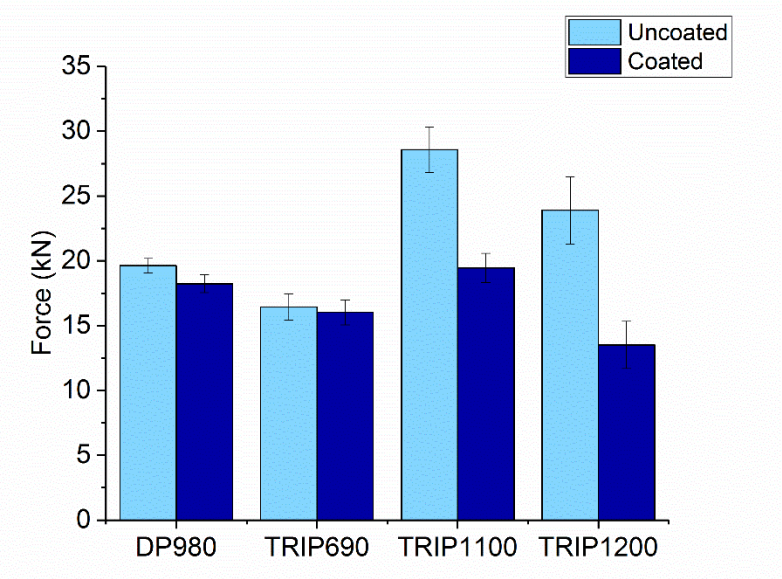

Figure 5.3 Comparison of peak load for coated vs. uncoated AHSS welded at I_{max}+10% [90]**.**

Table 5.2 Comparison of nugget diameters for coated vs. uncoated AHSS welded at I_{max}+10%

Material	Nugget Diameter	
	Uncoated	Coated
DP980	6.7	6.6
TRIP690	6.8	6.5
TRIP1100	7.6	7.8
TRIP1200	7.6	7.4

To explain this difference in strength loss, the percent difference in weld strength was plotted against the three cracking characterization metrics. For both mean crack length and 95th percentile crack length, the correlation coefficients (R^2 values) are very low (0.15 and 0.11, respectively) and the ANOVA analysis from the linear regression determined that the slope was not significantly different from zero. This indicates that there is no relationship between crack length and strength loss. However, upon closer inspection, there does appear to be an increasing trend but the outlying TRIP690 and TRIP1200 points at the bottom right of the graph (circled in Figure 5.4 a) and c)) are interfering with the statistical analysis. Similarly, a larger number of cracks also corresponds to a larger decrease in strength (Figure 5.4 b)). Although the correlation is not perfect, the ANOVA analysis determined that the slope of the trend line is significantly different from zero and the correlation coefficient is reasonable (R^2=0.71).

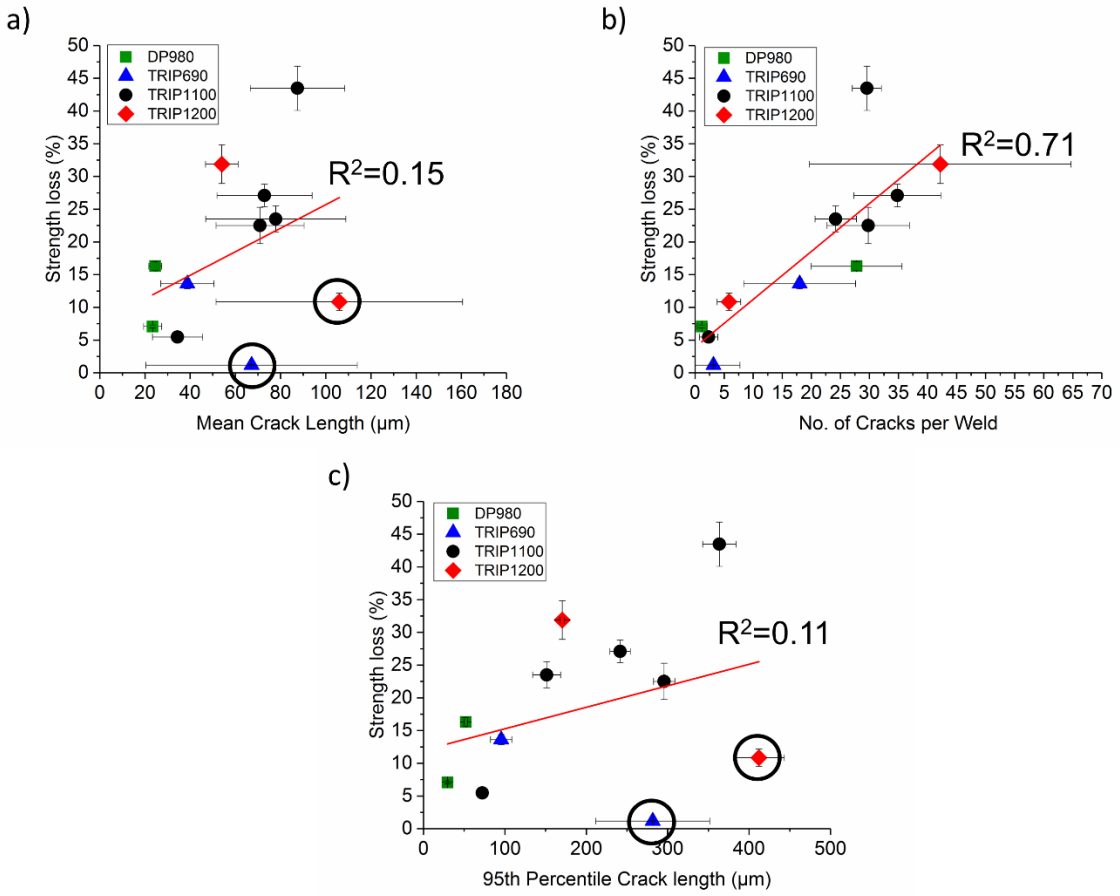

Figure 5.4 Relationship between a) mean crack length, b) number of cracks per weld, and c) 95th percentile crack length and weld strength loss for resistance spot welded AHSS [90]**.**

The observations that longer cracks and a larger number of cracks correspond to a larger strength loss are consistent with literature. Choi *et al*. observed that spot welds with LME cracks longer than 325 μm demonstrated a reduced mechanical performance [16]. In addition, DiGiovanni *et al*. showed that crack location and the direction of loading determine whether an LME crack will have an impact on weld strength and fracture [17,18]. While this location effect cannot be directly accounted for using one of these simple crack metrics, the probability of a crack being located in a critical area will increase as the number of cracks in the weld increases. This probabilistic effect explains why there is such a strong relationship between number of cracks and strength loss. Even though neither length nor number can fully predict the loss in strength, both clearly have an effect on the weld performance.

5.3 Crack Population Distributions

The analysis method must be amended to improve the correlation between crack sizes and weld strength loss. Previously, mean crack length was used because it is a common descriptor of the "typical" crack size in a population. However, the very large error bars in Figure 5.2 a) suggest that this may not be an accurate method for characterizing crack length. This is because when using the mean crack length, there is an underlying assumption that the data is normally distributed. However, constructing histograms of the LME crack populations shows that the normality assumption does not hold. Figure 5.5 a) shows a histogram of the actual cracks measured in samples of TRIP1200 welded at I_{max}+10% fitted with an ideal normal distribution with the same mean, standard deviation, and number of measurements. There is a clear lack of fit between the model and the data. Conversely, when fitted with a lognormal distribution instead, the model matches quite well with the data (Figure 5.5 b)). This indicates that lognormal statistics should be used to quantify LME crack size.

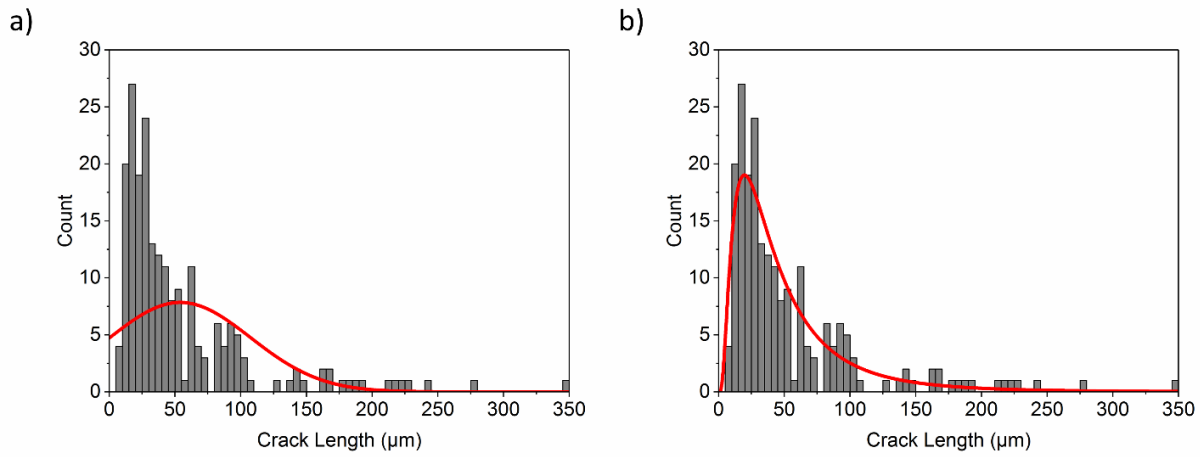

Figure 5.5 Histograms of LME cracks observed in TRIP1200 welded at I_{max}+10% fitted with a) a normal distribution and b) a lognormal distribution [90]**.**

Changing to using the lognormal mean shows an improvement over the arithmetic mean, as the error bars are slightly reduced (Figure 5.6 a)). However, the error bars are still overlapping, suggesting that the differences will not be statistically significant. In addition, the correlation between lognormal mean and strength loss is still poor, with an R^2 value of only 0.13 (Figure 5.6 c)) and the ANOVA analysis reveals that the slope is not significantly different from zero. The same two points in the bottom right corner of the graph are interfering with the analysis. A much more significant improvement is seen

when the lognormal median (also known as the geometric mean) is used instead of the lognormal mean. The error bars are considerably smaller (Figure 5.6 b)) and the correlation with the strength loss is also slightly improved (Figure 5.6 d)). While the ANOVA analysis still shows that the slope of the linear regression is not significant, the R^2 value is now 0.28, which is an improvement. Note that the lognormal distribution used was based on the natural logarithm. However, calculating using a base 10 logarithm yielded a very similar result.

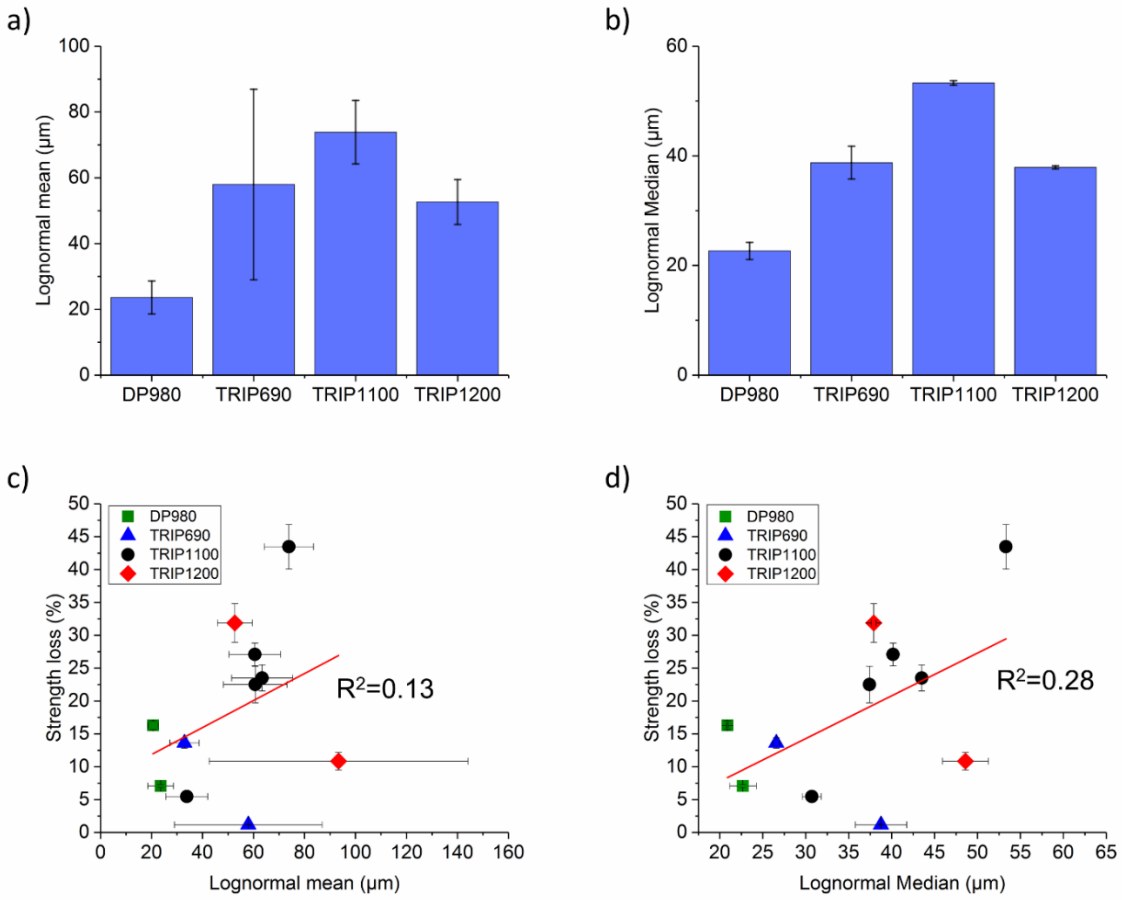

Figure 5.6 a) Lognormal mean and b) lognormal median of samples welded at I_{max}+10%. Relationship between c) lognormal mean and strength loss and d) lognormal median and strength loss in resistance spot welded AHSS [90]**.**

5.4 Crack Index

The results discussed in Section 5.2 indicate that both crack length and location have an impact on weld performance. To account for both of these factors, a "crack index" can be calculated:

$$Crack\ index = \frac{nL}{t} \tag{5.1}$$

where n is the number of cracks per weld, L is the lognormal median crack length, and t is the sheet thickness of the AHSS. The number of cracks per weld accounts for the probability that a crack is located in a critical area, while the lognormal median determines whether the crack is likely to be of sufficient length to cause a loss of strength. The product of n and L is divided by the sheet thickness as a normalization factor because the critical crack length for strength loss will depend on the sheet thickness. It is necessary to take a probabilistic approach because both the crack analysis and tensile lap shear testing are destructive methods. This means that the welds that are tensile tested cannot be the same welds which are analyzed for LME cracks, so the actual crack populations in the tensile lap shear samples are unknown.

Comparing the crack index for the four grades of AHSS welded at I_{max}+10%, the differences in LME severity are much clearer. TRIP1100 and TRIP1200 have approximately the same crack index, which is much greater than the crack index for DP980 and TRIP690 (Figure 5.7 a)). The LSD test showed there was no significant difference between TRIP1100 and TRIP1200 or DP980 and TRIP690. However, the TRIP1100 and 1200 do have a significantly higher crack index than DP980 and TRIP690 (Table 5.3). This is consistent with the cracking observed in the micrographs in Figure 5.1. TRIP1100 and TRIP1200 displayed very serious cracking with very long cracks (for TRIP1100 only) and large numbers of small cracks, while DP980 and TRIP690 showed few cracks in general. The crack index may be physically considered to be a ratio of the total length of cracks in the cross section to the sheet thickness.

The crack index is able to effectively model the effect of LME cracking on weld strength loss. Plotting the strength decrease against the crack index reveals a linear relationship (Figure 5.7 b)). The ANOVA analysis shows that the slope is significantly different from zero and the R^2 value of 0.9 indicates that the model fits the data well.

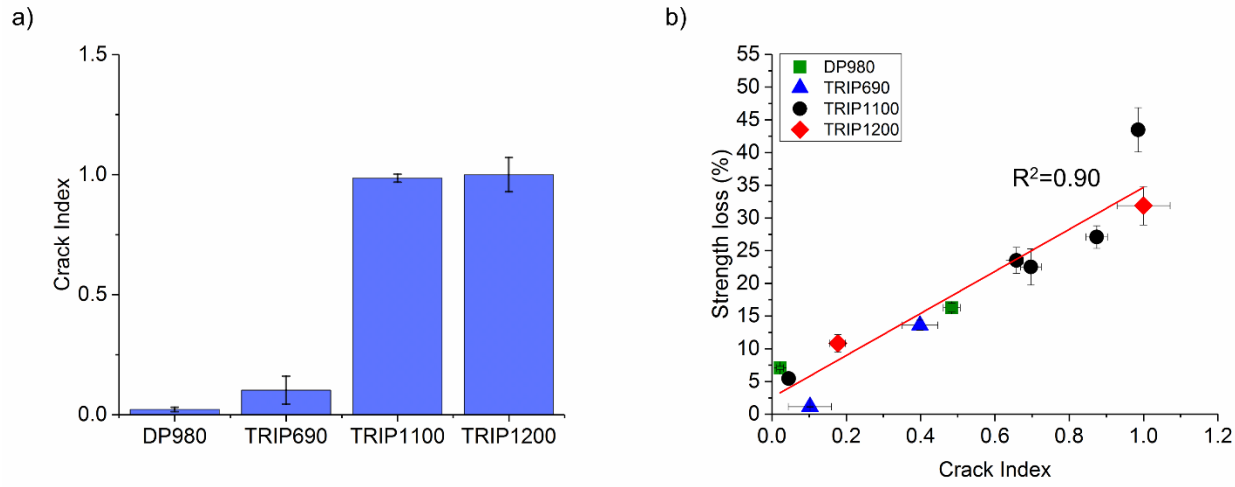

Figure 5.7 a) Crack index for AHSS welded at I_{max}+10%. b) Relationship between crack index and strength loss for AHSS [90]**.**

Table 5.3 Significance testing for differences in crack index in AHSS welded at I_{max}+10%.

Material	Crack Index
DP980	0.02
TRIP690	0.10
TRIP1100	0.99
TRIP1200	1.00
LSD	0.12

5.5 Alternative Crack Indices

While the crack index is able to accurately explain the loss of strength in LME affected welds, using the lognormal median to characterize crack length is not intuitive and may be complicated for those who are unfamiliar with this type of distribution. In the following sections, several alternative methods for calculating a crack index are discussed to simplify analysis.

5.5.1 Crack Index with Normal Median

The lognormal median was used as the characteristic length in the original crack index because the LME crack population was observed to fit a lognormal distribution. However, a comparison between the normal and lognormal median reveals that the two are similar in most cases (Figure 5.8 a)). Recalculating the crack index with the normal median and plotting against the strength loss reveals that

there is still a strong correlation (Figure 5.8 b)). The ANOVA confirms that the slope is still significantly different from zero, and the R^2 is 0.88, which is only a decrease of 0.02 compared to the crack index with lognormal median.

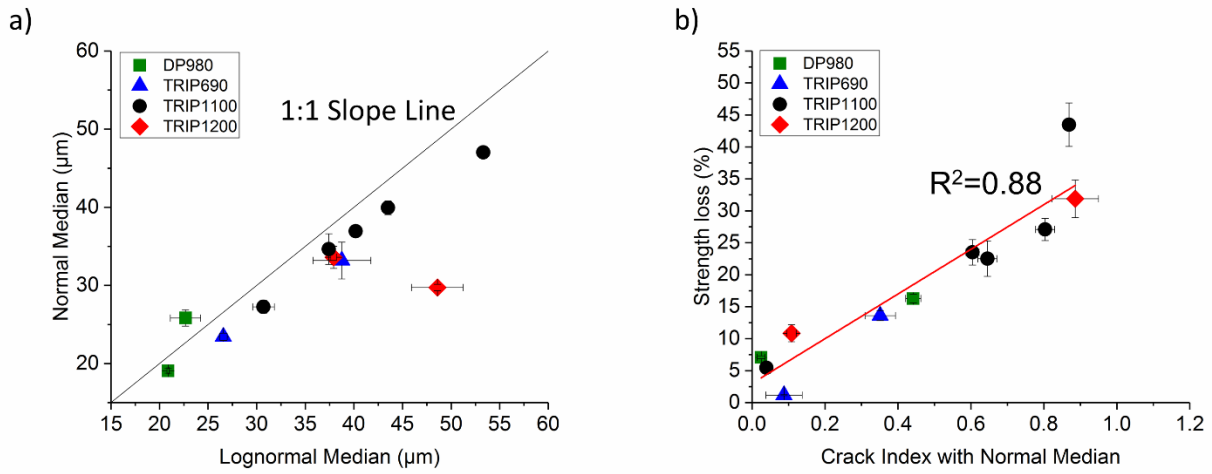

Figure 5.8 a) Comparison of normal and lognormal median. b) Relationship between crack index calculated with normal median and strength loss [90]**.**

5.5.2 Crack Index with Different Percentile Crack Lengths

The median crack length is the same as the 50th percentile crack length. The crack index was also calculated using different percentile lengths. Each of these crack indices was plotted against the strength loss and linear regression was performed to get a correlation coefficient (R^2). The R^2 values were plotted against the percentile to determine which percentile gave the best correlation with strength loss. It appears that most of these crack indices correlate reasonably well with strength loss. All of the R^2 values are above 0.8, with the exception of the crack index calculated with the 90th percentile crack length. In general, it seems that the R^2 value decreases as percentile increases (Figure 5.9).

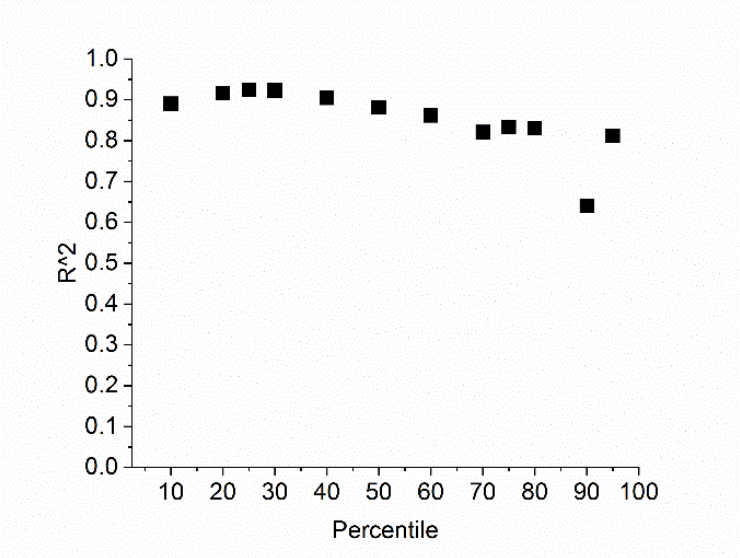

Figure 5.9 Correlation coefficient (R^2) for crack indices calculated with different percentile crack lengths.

To identify why this is the case, the regressions were examined more closely. There is an outlier to the linear trend seen in many of the regressions (TRIP1100 with a 43% strength loss), which is circled in red in Figure 5.10 a) and b). With moderate percentiles (Ex. 60th percentile shown in Figure 5.10 b)), this point is separated from the line. However, as the percentile decreases, the outlier moves closer to the main line (Ex. 20th percentile shown in Figure 5.10 a)). The fit does not actually seem to be changing significantly but because the outlier moves closer, the R^2 is increasing. However, with the high percentiles (Ex. 95th percentile shown in Figure 5.10 c)), the linear fit actually does appear to be worse.

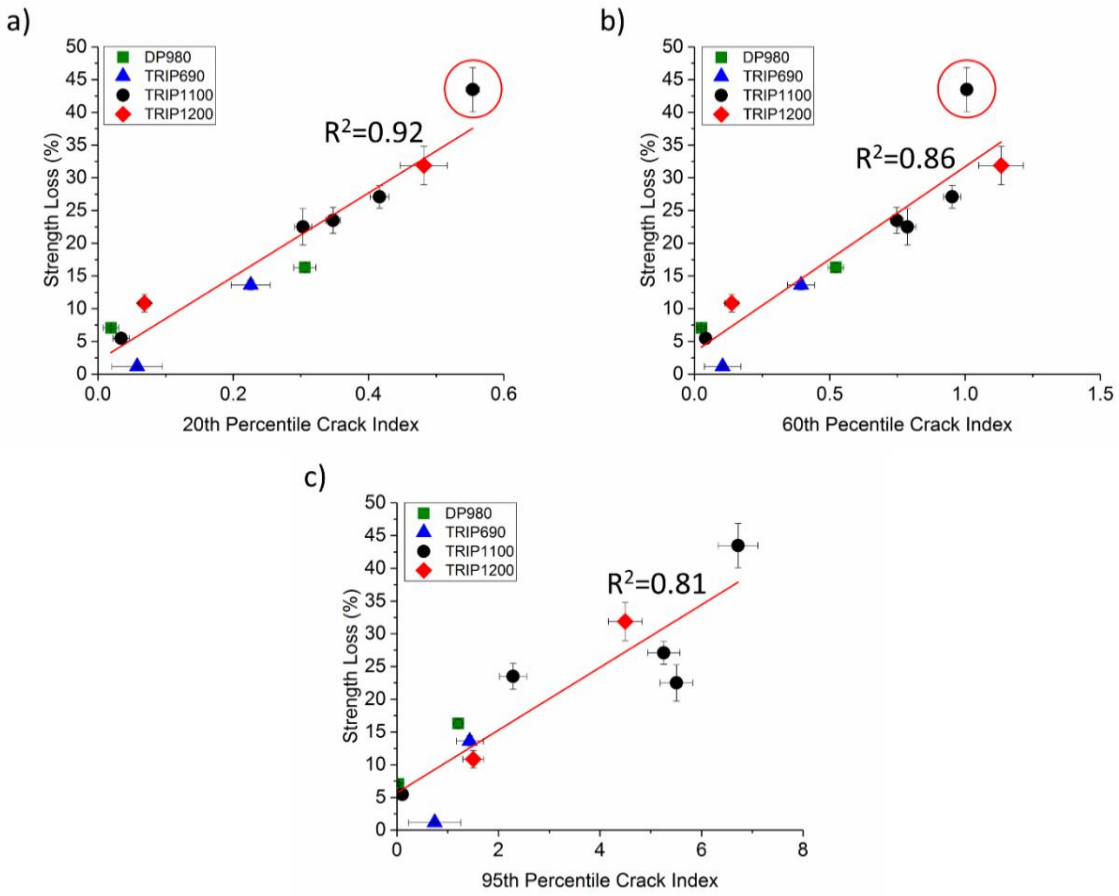

Figure 5.10 Relationship between crack index and strength loss for crack index calculated using a) 20th, b) 60th, and c) 95th percentile crack length.

To isolate the actual fit from the effect of the outlier, the outlying data point was removed and the analysis was repeated. The R^2 values were again plotted against the percentile. The R^2 remained fairly constant, particularly in the range of 30^{th} to 75^{th} percentile (Figure 5.11). There is a slight decrease in R^2 with the very small percentiles (10^{th} to 25^{th}) but overall the R^2 does not change much until the 80^{th} percentile, when it begins to decline. This indicates that any percentile crack length below the 80^{th} percentile can be used to calculate a crack index, as long as it is used consistently. However, the percentiles above the 80^{th} did not correlate as well with the strength loss, likely because they are strongly affected by the presence of very long cracks. Using the median (or other percentile crack length) implicitly assumes that the different crack populations fit the same type of distribution. The ability to use any crack length between the 10^{th} to the 80^{th} percentile shows that using a statistical approach to characterize crack length is valid.

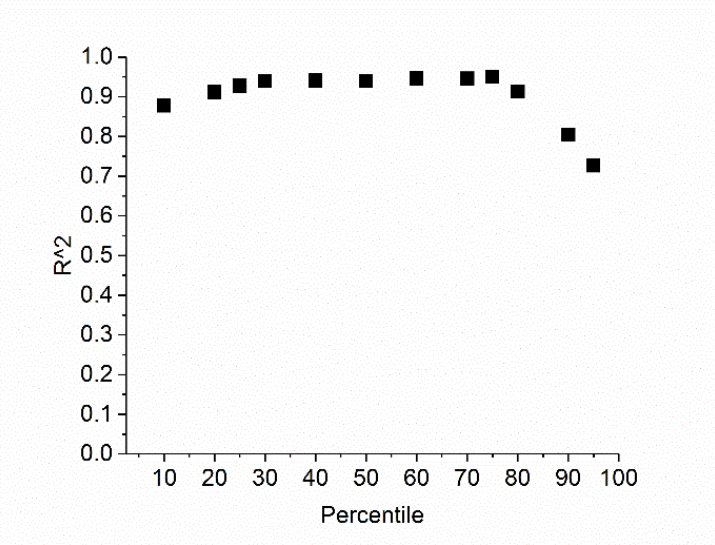

Figure 5.11 Correlation coefficient (R^2) for crack indices calculated with different percentile crack lengths with outlier removed.

5.6 Summary and Further Work

This chapter proposed a crack index to characterize LME cracking severity based on crack length, number of cracks, and sheet thickness. The crack index was shown to have a strong linear relationship with loss in tensile lap shear strength. It is calculated using the lognormal median as a metric of crack size, number of cracks per weld to account for the probability that a crack will be located in a critical area, and sheet thickness as a normalization factor. The crack index is able to quantify differences in cracking populations with more confidence than previously used cracking metrics (mean crack length, number of cracks, and 95th percentile crack length) due to its lower uncertainty. Normal median (50th percentile crack length) or another percentile crack length below the 80th percentile may also be used to calculate a crack index, confirming that the probabilistic approach to measuring crack length is valid. However, crack indices calculated with the 80th percentile or above do not demonstrate as strong a correlation with strength loss because they are strongly affected the presence of very long cracks.

In the following chapters, the term "crack index" will refer to the crack index calculated using the lognormal median. The next chapter will apply the crack index analysis to the data from Chapter 4 on the effect of welding schedule on LME cracking.

Chapter 6
Applying the Crack Index to Analyze Impact of Multiple Pulse Welding Schedules on LME Severity

In Chapter 4, the effect of multiple pulse welding schedules (pulsed and pre-pulse welding) were investigated using mean crack length, number of cracks per weld, and 95th percentile crack length as the metrics of cracking severity. Due to a lack of statistically significant differences between welding conditions using these metrics, the overall crack distributions were also examined. In this chapter, the data from Chapter 4 will be re-analyzed using the crack index method developed in Chapter 5. The crack index will be calculated using Equation 5.1 with the lognormal median used as the crack length parameter. The mechanisms responsible for the observed changes in crack index will also be explored.

6.1 Effect of Pulsed Welding Schedules

6.1.1 Single vs. Double Pulse Welds

In Chapter 4, it was concluded from the crack distribution patterns that single pulse welds demonstrated worse LME than double pulse welds in DP980. The most frequently observed crack length was the same for all four pulsing conditions (10 – 15 μm); however, the single pulse condition had a greater number of cracks in this range.

Re-analyzing the data using the crack index method confirmed that single pulse welds do indeed exhibit more severe LME cracking than double pulse welds. Using a double pulse welding schedule resulted in a 52 – 62% reduction in crack index compared to the standard double pulse welding schedule (Figure 6.1). This result is consistent with literature, as Ashiri *et al.* were able to eliminate LME cracking in the shoulder of electrogalvanized TWIP steel with a UTS of 920 MPa by changing from a single to double pulse weld [43]. SORPAS modelling demonstrated that this was due to reduced temperature and tensile stresses in the weld shoulder, which they termed the "supercritical LME area." The significance of the results of this study were analyzed using the LSD method described in Section 3.6.2 with an overall significance level of α'=0.05. The Bonferroni correction was used to determine the significance for the individual comparisons (α=0.01 in this case). The LSD calculation showed that the differences between the single pulse condition and each of the double pulse conditions are significant (Table 6.1). No significant difference was seen between the LME responses of the three double pulse welding schedules.

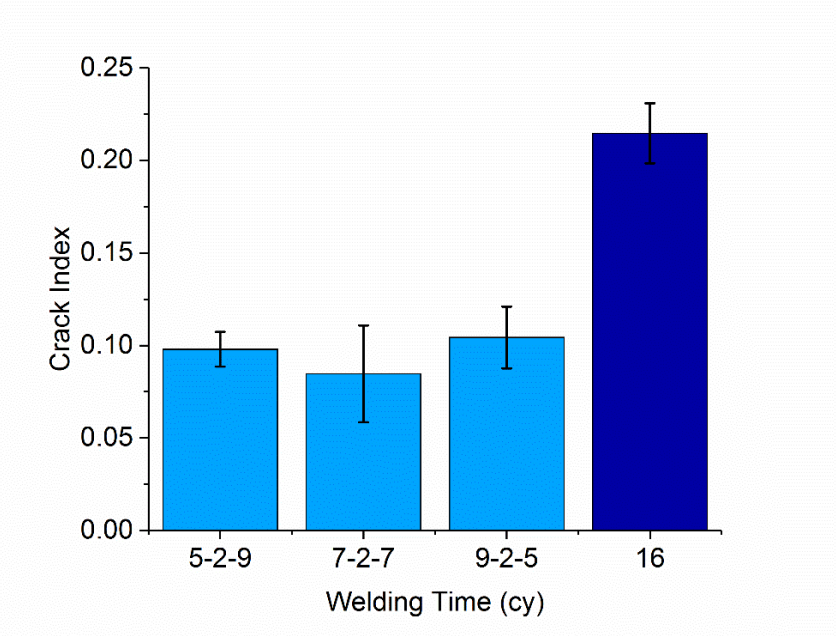

Figure 6.1 Comparison of crack index for DP980 welded with different pulsing conditions.

Table 6.1 Crack index and LSD for DP980 welded with different pulsing conditions.

Welding Time (cy)	Crack Index
5-2-9	0.10
7-2-7	0.08
9-2-5	0.10
16	0.21
LSD	0.05

6.1.2 Effect of Changing Pulse Lengths

In Chapter 4, it was concluded that welds made using the welding schedule consisting of a short pulse followed by a longer pulse (5-2-9 cy in DP980 and 10-2-14 cy in TRIP1100) demonstrated the worst LME cracking, while there was no clear difference between the other two conditions. Re-analyzing the LME cracks in welds in DP980 using the crack index method shows that there is no significant difference in cracking between the three different double pulse conditions (Table 6.1). This contradicts the observations from Chapter 4 and is unexpected because there was an obvious difference in crack length distribution between the 5-2-9 cy welds and the 7-2-7 and 9-2-5 cy welds (Figure 4.2 a)). However,

it is possible that pulsing does affect LME and the difference is not seen with DP980 because it is relatively insensitive to LME.

Using the crack index method to examine LME cracking of welds made in TRIP1100, which is more LME sensitive than DP980, a clear difference was seen in the LME severity of the three pulsing conditions. The 10-2-14 cy welds had the highest crack index, which is consistent with the observations made in Chapter 4. A difference can even be resolved between the 12-2-12 and 14-2-10 cy welds. Welds made with the 12-2-12 cy welding schedule have the lowest crack index and the 14-2-10 cy welds have a slightly higher crack index (Figure 6.2). Calculating the LSD (using a significance level of α=0.02 for the individual tests in this case) showed that the differences are significant for all the possible comparisons (Table 6.2).

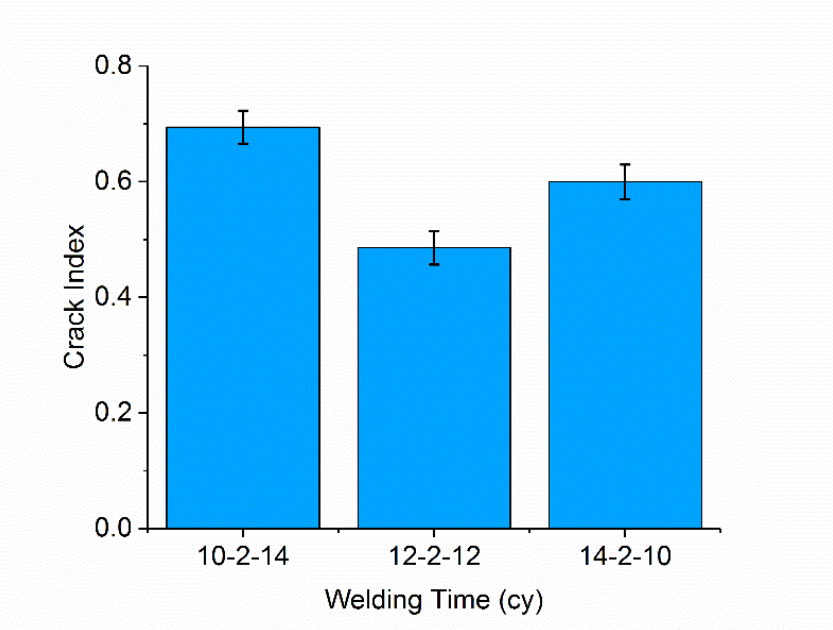

Figure 6.2 Comparison of crack index for TRIP1100 welded with different pulsing conditions.

Table 6.2 Crack index and LSD for TRIP1100 welded with different pulsing conditions.

Welding Time (cy)	Crack Index
10-2-14	0.69
12-2-12	0.49
14-2-10	0.60
LSD	**0.06**

Since the nugget diameters of the welds made using the three conditions are approximately equal, the heat input is also approximately the same. This means that the change in LME severity must be due to the different thermal histories creating a difference in the microstructure in the welds. The three welding schedules are identical until 10 cy into the weld, where they diverge. Therefore, welds made with only the first pulse (10, 12, 14 cy) were examined using SEM to observe differences in coating morphology.

As the length of the first pulse increases, the amount of free zinc available for LME is expected to decrease. The reasons for this are two-fold. Firstly, some of the molten zinc coating will be "squeezed" out of the weld area by the electrode force, resulting in a thinner coating. Reducing coating thickness is a strategy which has been employed to prevent LME in previous literature [95]. Secondly, some iron will diffuse into the zinc coating, forming a Fe-Zn alloy. This increases the stability of the zinc, as evidenced by the phase diagram, which shows that as the amount of iron increases, the liquidus temperature also increases (Figure 6.3). This increased stability should create some additional resistance to LME. The reduction of LME with a change in alloying has been well documented. Recall the example of Bi-Pb embrittlement of copper, in which LME severity decreased as Pb content increased above 30% (discussed in Section 2.4.3) [60]. Similar effects have been observed in the $steel_{solid}/Zn_{liquid}$ system. For instance, Beal *et al*. observed that holding EG coated TWIP steel at 750°C prior to high temperature tensile testing was able to prevent LME due to the formation of Fe-Zn intermetallic compounds [50]. It has also been seen that GA coatings, which are composed of a Fe-Zn alloy, exhibit less severe LME than GI coatings [10,43].

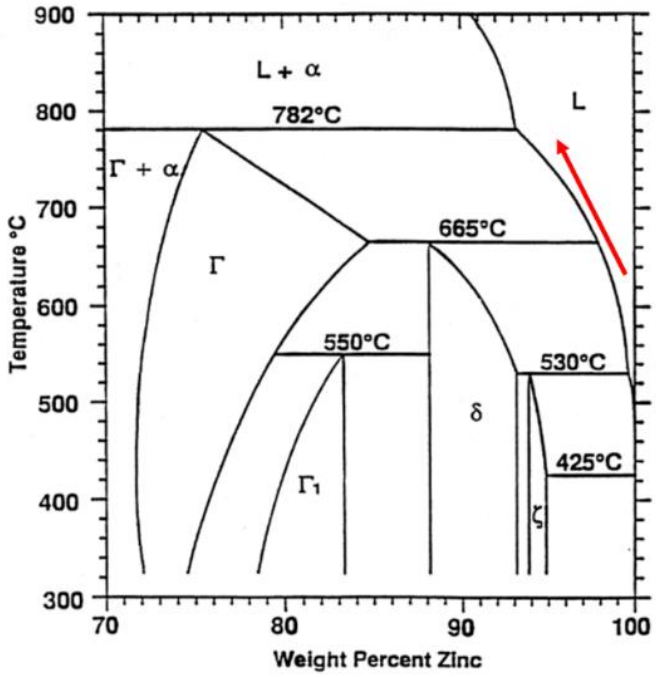

Figure 6.3 Iron-zinc phase diagram [24]**.**

To confirm that the amount of available zinc is decreasing, the thickness and composition of the remaining zinc coating was analyzed using EDS. Because the majority of cracks occur in the shoulder (supercritical LME area), EDS analysis was focused on the shoulder (Figure 6.4 a)). In the analysis of the EDS line scans, the boundary of a material layer was defined as the point at which the height of the EDS curve decreased to half of its peak height.

To estimate the thickness of the zinc coating layer, the peak height was first determined for both the iron and zinc peaks (Figure 6.4 b)). A second line was then drawn at half the peak height (Figure 6.4 c)). A vertical line was drawn at the point where the iron peak intersected with the half height line to determine the transition point between the steel and zinc. A second vertical line was drawn where the zinc peak intersects with its half height line to determine the location of the edge of the zinc coating (Figure 6.4 d)). The distance between the two lines was measured to determine the zinc thickness. This process was repeated in three different locations in the shoulder and the thickness measurements were averaged.

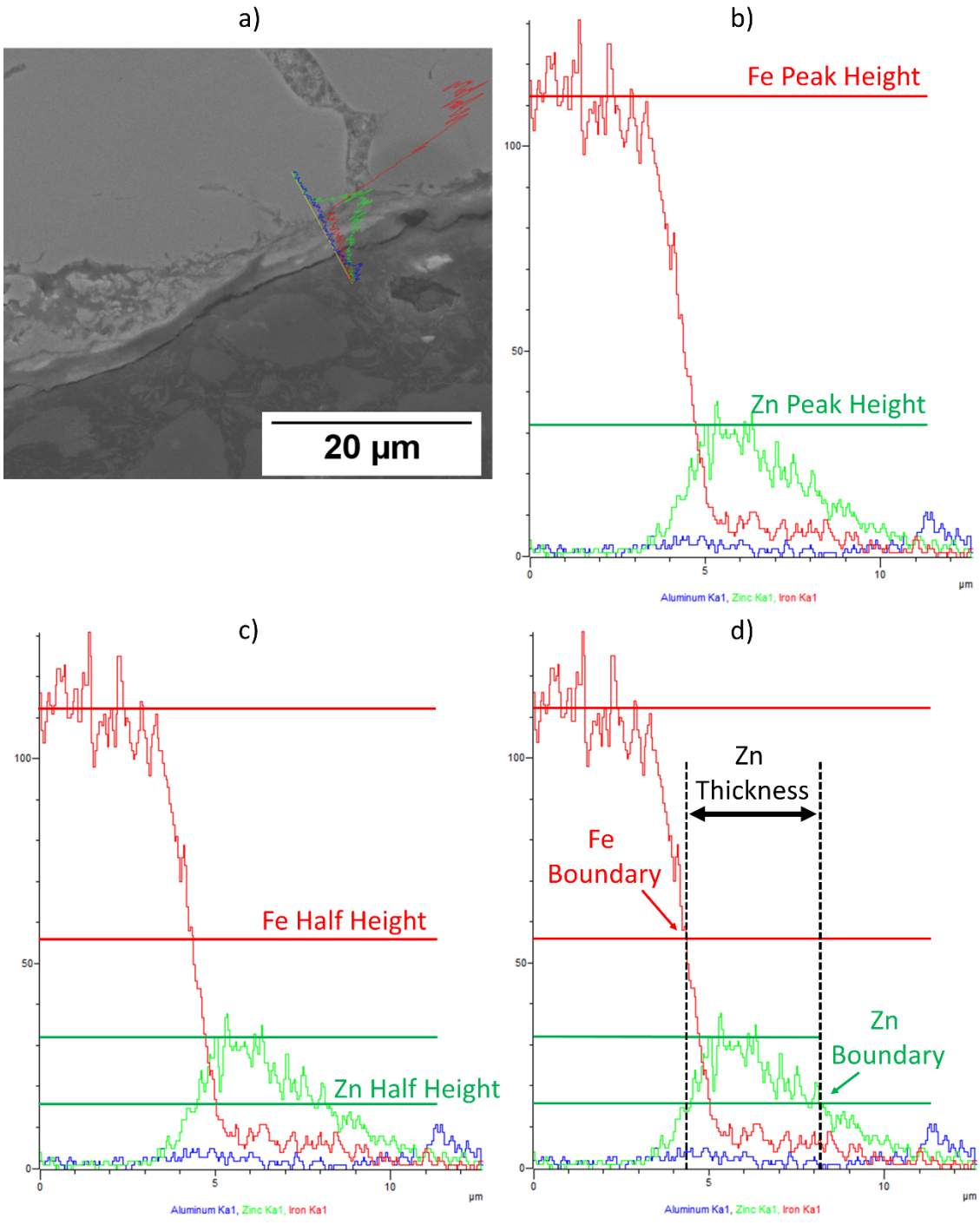

Figure 6.4 a) EDS line scan of zinc coating remaining on TRIP1100 after a 12 cy pulse. Iron is shown in red, zinc is in green, and aluminum is in blue. b) Measurement of peak heights. c) Determination of peak half heights. d) Measurement of zinc coating thickness.

To determine how much iron is in the zinc coating after the first pulse, the peak height for iron in the steel was measured, as well as the height of the iron in the zinc coating (Figure 6.5). The peak height gives the EDS count for approximately 100% iron. Thus, the percentage of iron in the zinc coating can be approximated by calculating the ratio of the EDS count in the coating to the EDS count in the steel:

$$\% \text{ of Fe in Zn} = \frac{\text{Height of Fe in Coating}}{\text{Fe Peak Height}} \times 100. \tag{6.1}$$

As with the zinc coating thickness, this measurement was repeated three times and the results averaged.

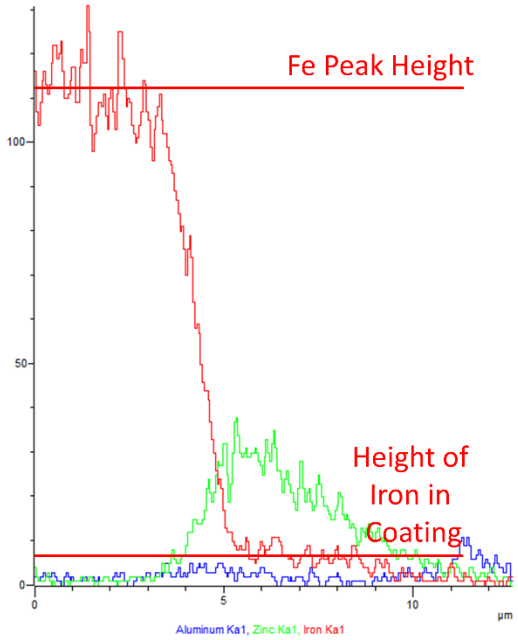

Figure 6.5 Method for determining amount of iron in the remaining zinc coating for a sample of TRIP1100 welded with a 12 cy pulse.

The EDS analysis confirmed that as the length of the first pulse increases, the zinc coating thickness is decreasing and iron alloying is increasing, leading to a reduction in free zinc for LME (Figure 6.6). Since Ashiri *et al*. indicated that LME occurs during the second pulse (when the critical nugget diameter is reached) [43], this explains why the 10-2-14 cy welds display the most severe LME: there is more zinc available at the end of the first pulse and it is less stable.

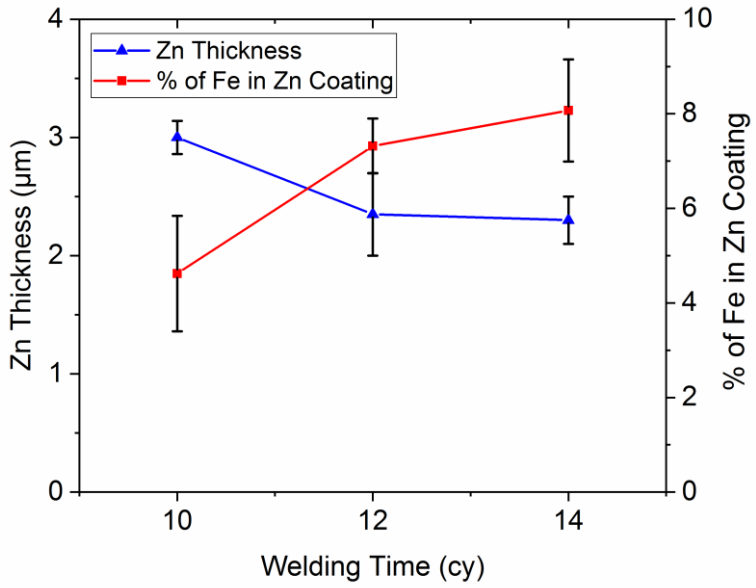

Figure 6.6 Average thickness and composition of zinc coating remaining after the first pulse.

However, the reduction in free zinc does not explain why the 14-2-10 cy welds also shows more severe LME than the 12-2-12 cy welds. Since there is less available and more stable zinc at the beginning of the second pulse, it would be expected that LME would be less likely to occur. To gain a better idea of how the 12-2-12 and 14-2-10 cy welding times differ, the model developed by DiGiovanni *et al.* [101] was used to examine the differences in temperature and stress throughout the welding time using the three pulsed welding schedules. Because the model is still under development, the output values have been excluded from the analysis and only the general trends are discussed. The temperature profiles are largely the same, with the main differences appearing between 0.2 and 0.3 s (the cool times between pulses). The model showed that for the 14-2-10 cy welding time, at the end of the first pulse (at 0.233 s) the electrode pushes into the steel, creating an indentation (mechanical collapse).This brings the shoulder area into contact with the water-cooled electrode, which, combined with the beginning of the cool time, causes a large drop in temperature (Figure 6.7 a)). The rapid cooling generates tensile stresses in the shoulder, creating potential for LME to occur. Conversely, for the 12-2-12 cy and 10-2-14 cy welding times, the mechanical collapse occurs in the second pulse, resulting in two smaller temperature drops. The plot of maximum principle stress shows that the 14-2-10 cy welding time results in the largest tensile stresses in the shoulder area (Figure 6.7 b)). These results contradict Ashiri's assertion that LME occurs during the second pulse [43]. LME may or may not occur in the second pulse, depending on the temperature and

stress distributions within the weld. For the conditions used in this study, LME cracks in the shoulder are most likely to form during the cool time between the two welding pulses because the stresses change from compressive to tensile. Reduction in free zinc and increase in tensile stress are competing effects that act on the weld to either suppress or facilitate LME. A welding time of 12-2-12 cy provides the optimum conditions for LME resistance, resulting in the lower crack index shown in Figure 6.2.

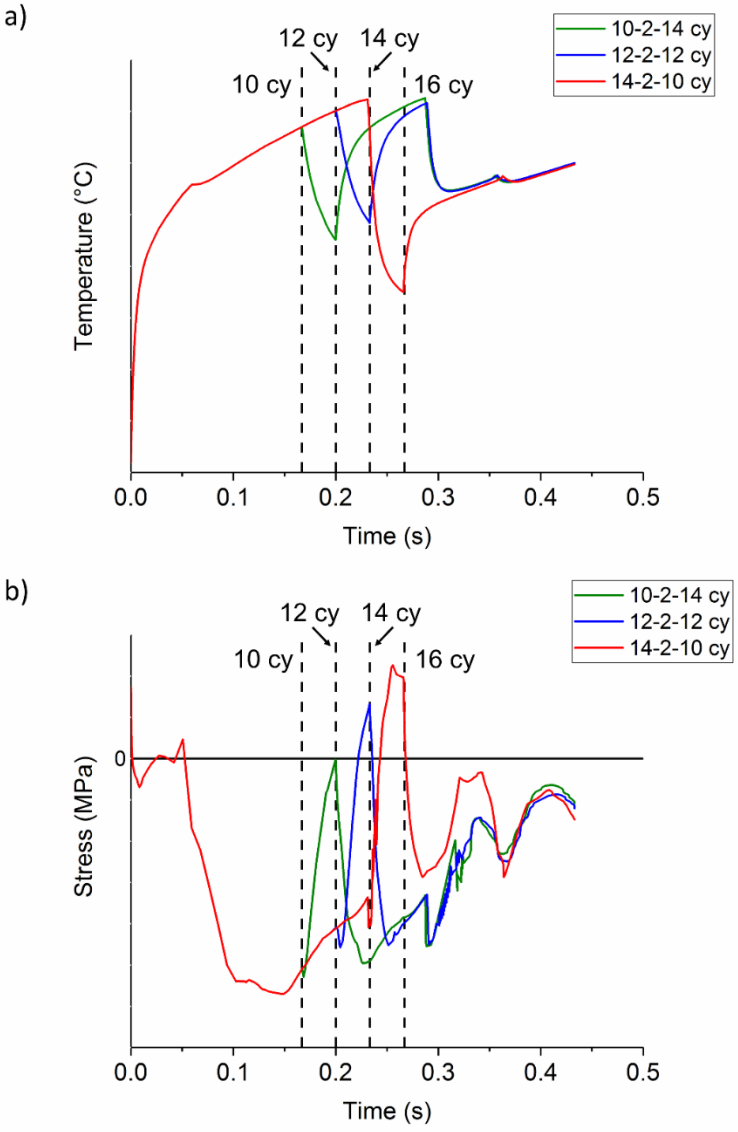

Figure 6.7 a) Temperature and b) maximum principle stress in the weld shoulder of TRIP1100 welded with different pulsing conditions.

6.2 Effect of Pre-Pulse Welding Schedules

The first pre-pulse conditions tested were high currents (11 – 17 kA) applied over a long time (6 cy). These pre-pulse conditions were selected to minimize the zinc coating thickness in the weld area. In Chapter 4, it was concluded that these high current, long time pre-pulses did not decrease LME severity in welds of TRIP1100 because too much additional heat was applied during the pre-pulse. Re-analyzing the data using the crack index method confirms that this conclusion was correct. Applying a high current, long time pre-pulse increases the crack index (Figure 6.8).

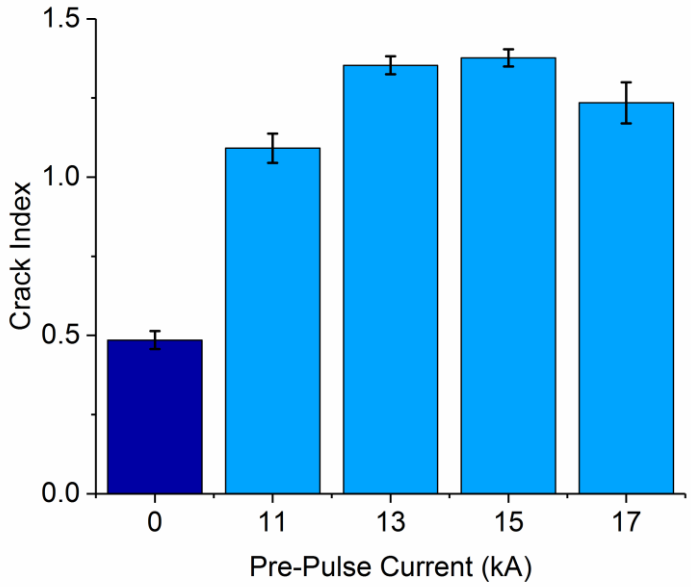

Figure 6.8 Comparison of crack index for TRIP1100 welded with 6 cy pre-pulses of different currents.

The next condition tested was a high current, short time pre-pulse (17 kA, 1 cy). This pre-pulse was selected to melt the zinc coating without introducing as much extra heat into the weld. In Chapter 4, it was shown that this type of pre-pulse was not successful in reducing LME, which is again confirmed by the crack index analysis. As with the 6 cy pre-pulses, the crack index increases when the pre-pulse is applied (Figure 6.9).

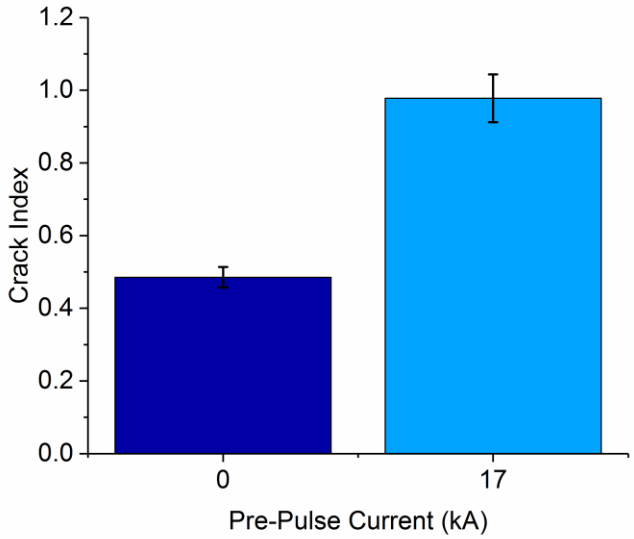

Figure 6.9 Comparison of crack index for TRIP1100 welded with and without 17 kA, 1 cy pre-pulse.

The final pre-pulse condition tested was a low current (4 kA) over a longer time (3 – 6 cy). These pre-pulses were also intended to reduce the zinc coating thickness without introducing too much additional heat into the weld. In Chapter 4, it was shown that these pre-pulses also did not significantly reduce LME. However, when re-analyzed with the crack index method, these pre-pulses actually did cause a reduction in LME cracking (Figure 6.10). The 6 and 12 cy pre-pulses showed a small reduction in LME cracking (10%), while the 3 cy pre-pulse showed a larger reduction (29%). The LSD calculation (performed using a significance level of α=0.005 in this case) showed that these reductions in LME cracking were statistically significant (Table 6.3).

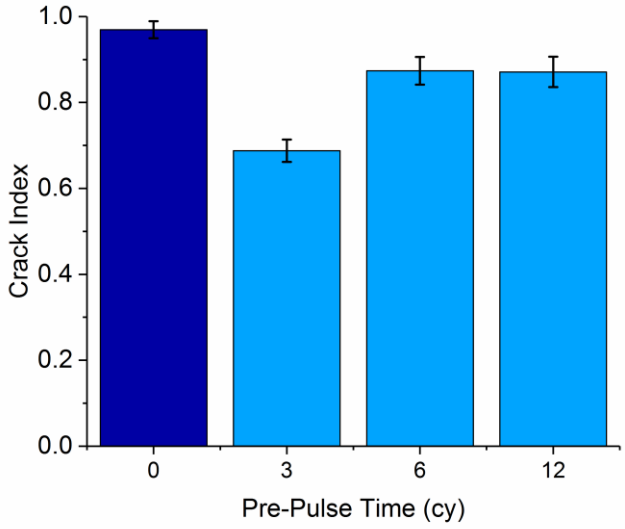

Figure 6.10 Comparison of crack index for TRIP1100 welded with 4 kA pre-pulse of different lengths.

Table 6.3 Crack index and LSD for TRIP1100 welded with 4 kA pre-pulses of different lengths.

Pre-pulse Time (cy)	Crack Index
0	0.97
3	0.69
6	0.87
12	0.87
LSD	**0.08**

Recall that the heat input to the weld is given by the equation

$$Q = I^2 R t_{dur} \tag{2.1}$$

where I is the welding current, R is resistance, and t_{dur} is welding time. Both the low current, long time pre-pulses and high current, short time pre-pulses were intended to reduce the coating thickness without introducing additional heat into the weld. The low current, long time pre-pulse was much more successful due to the squared dependence of heat input on current. Reducing the current causes a more significant reduction in heat input than reducing time.

To determine why the 4 kA, 3 cy pre-pulse was the most effective at reducing LME cracking, EDS analysis was carried out, as in Section 6.1.2. The zinc coating thickness and Fe alloying were measured following the application of the pre-pulse. The zinc coating thickness was similar between the three different pre-pulse lengths (Figure 6.11), suggesting that the coating did not melt during the pre-pulse. However, some iron still diffuses into the zinc coating during the pre-pulse, stabilizing the zinc. The amount of iron in the zinc coating increases as the length of the pre-pulse increases (Figure 6.11). Based on this alone, it would be expected that welds made using the 12 cy pre-pulse have the least severe LME. This is not the case because there is also a competing effect of increasing heat input to the weld as the pre-pulse length increases. The larger heat input is illustrated by a larger nugget diameter (Table 6.4). A 4 kA, 3 cy pre-pulse reduces the free zinc available for LME without introducing too much additional heat, leading to the best LME resistance.

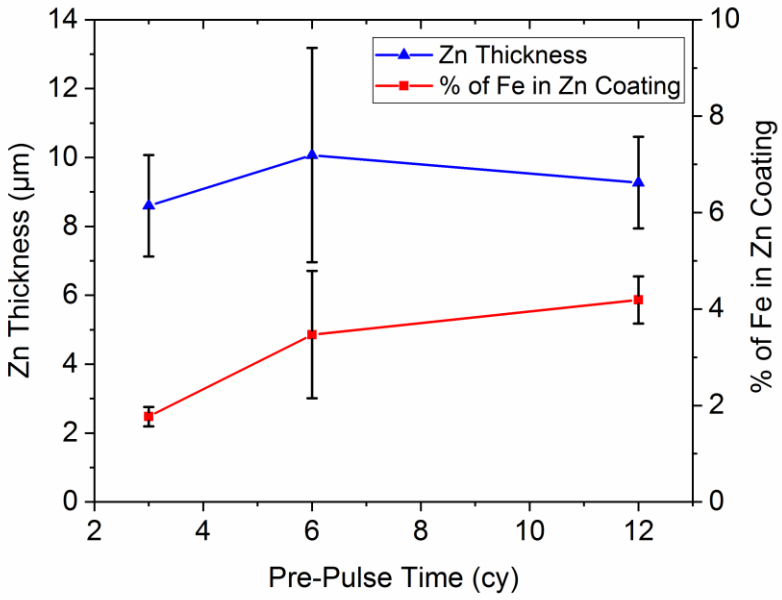

Figure 6.11 Average thickness and composition of zinc coating remaining after a 4 kA pre-pulse.

Table 6.4 Nugget diameter for TRIP1100 welded with 4 kA pre-pulses of different lengths.

Pre-pulse Time (cy)	Nugget Diameter (mm)
3	6.7
6	7.0
12	7.1

6.3 Summary

Based on the analysis presented in this chapter, the conclusions from Chapter 4 can be amended. A number of the conclusions remain the same, but can be stated with greater confidence after conducting the crack index analysis.

As in Chapter 4, it was seen that using a double pulse welding schedule was able to decrease LME cracking. However, unlike in Chapter 4, the effect of the different pulsing conditions is now clear. For TRIP1100, the most severe LME was observed for welds made with a short pulse followed by a long pulse (5-2-9 cy for DP980 and 10-2-14 cy for TRIP1100) and the least severe LME was seen in welds made with two equal length pulses (7-2-7 cy for DP980 and 12-2-12 cy for TRIP1100). The reason for this was determined to be a combination of a reduction in available zinc and lower tensile stresses. For DP980, there was not a statistically significant difference in LME cracking for the different double pulse conditions.

Previously, it was concluded that the pre-pulse method was not effective in reducing LME severity in resistance spot welds. Following crack index analysis, pre-pulse may in fact be used to help mitigate LME. However, successful use of the pre-pulse method requires careful selection of parameters. In TRIP1100, a 4 kA, 3 cy pre-pulse was able to reduce LME cracking by almost 30%. This is because the pre-pulse alloys iron alloying to stabilize the zinc without introducing too much additional heat into the weld.

Chapter 7
Conclusions and Recommendations

The objectives for this research were to relate LME severity to mechanical performance of resistance spot welds and to reduce LME cracking by manipulating the welding schedule. Reduction of LME cracking was attempted using two types of multiple pulse welding schedule: pulsed welding and pre-pulse welding. The conclusions of this thesis are presented in the following sections, as well as recommendations for future research.

7.1 LME Quantification and Relationship to Weld Performance

Commonly used LME cracking quantification metrics, such as mean or maximum crack length, are unable to accurately characterize LME cracking in resistance spot welds because of large variability in the data. This work demonstrated that this is because these crack metrics assume the crack populations are normally distributed when they are actually lognormally distributed. In addition, conclusions regarding differences in LME severity between materials or welding conditions depend on which of these metrics is used, as the trends observed are different. Because an ideal cracking quantification metric should be relatable to weld performance, LME cracking was compared to the loss in tensile lap shear strength. Both crack length and number of cracks have a correlation with weld strength loss, although neither is able predict loss in strength alone due to the noise in the data. A new crack characterization method, known as the crack index, was developed using the lognormal median as a metric of crack size, the number of cracks to describe the probability that a crack will be located in a critical location, and the sheet thickness as a normalization factor. The crack index has a lower associated error and a linear relationship with loss in tensile lap shear strength. It is the first LME quantification method to be successfully linked to weld mechanical performance. Crack indices calculated using the normal median (50^{th} percentile crack length) or other percentile crack length below the 80^{th} percentile also show a strong correlation with weld strength loss. This indicates that the probabilistic approach to measuring crack length is valid. The correlation with strength loss is not as strong for crack indices calculated with the 80^{th} percentile crack length or above as they are more sensitive to outliers.

7.2 Effect of Multiple Pulse Welding Schedules on LME Severity

Ashiri *et al*. demonstrated the use of a pulsed welding schedule to reduce LME cracking severity in resistance spot welds by slowing the nugget growth [43]. This research confirmed that using a double

pulse welding schedule rather than a single pulse welding schedule does reduce LME severity, as Ashiri concluded. In welds of DP980 made using a double pulse welding schedule, the crack index was 52 – 62% lower than in those made using a single pulse welding schedule. However, the mechanism described in Ashiri's study was not able to explain the effect of pulsing on LME cracking when heat input was kept constant between welding schedules. Pulsing improves LME resistance both by changing the coating morphology and controlling the temperature and stress states in the weld. As the welding time proceeds, the zinc coating becomes thinner and iron diffuses into the coating, stabilizing the zinc. Therefore, as the length of the first pulse increases, the availability of free zinc for LME at the end of the first pulse decreases. This is important because thermo-mechanical modelling shows that LME is most likely to occur in the weld shoulder during the cool time between pulses, when the stresses change from compressive to tensile. This contradicts Ashiri's work, which showed that LME occurred during the second pulse. As the length of the first pulse increases, the magnitude of the tensile stress during the cool time also increases. A pulsed welding schedule consisting of two equal length pulses provides the optimum LME resistance in welds of TRIP1100 by reducing the amount of free zinc available for LME without introducing too much tensile stress in the shoulder.

Application of a pre-pulse was used by Kim *et al*. to reduce LME cracking severity in resistance spot welds [11]. Kim's study concluded that the reduction in LME was due to the zinc coating being removed from the weld area by the pre-pulse. This work showed that this is not the case; when a pre-pulse is applied that generates enough heat to melt the coating, the LME cracking becomes more severe due to the increased heat input. However, low current (4 kA) pre-pulses are able to reduce crack index by 10 – 29% in welds of TRIP1100. These pre-pulses do not increase the temperature enough to melt the coating but do allow zinc diffusion into the coating to occur. As the length of the pre-pulse increases, the iron alloying (and therefore, zinc stability) increases. However, the nugget diameter (and therefore, heat input) also increases. A 4 kA, 3 cy pre-pulse provides the best LME resistance because it allows iron to diffuse into the coating and stabilize the zinc without introducing too much additional heat.

7.3 Recommended Future Work

This work has shown that a multiple pulse welding schedule can be used to reduce LME cracking in resistance spot welds. However, there is still additional work that should be done to fully understand and implement these methods. The study on welding with a pulsed schedule only examined three different types of double pulse welding and the welding schedules used were very similar (only a difference of 2 cy between pulse lengths). Examination of other types of pulsed welding schedules is needed to understand

where the first pulse should end for optimum LME resistance. Also, further study is needed to determine why this work was not able to replicate the complete elimination of LME cracks observed by Kim *et al.* when applying the pre-pulse method [11]. Perhaps the pre-pulse welding schedules can be adjusted to give a greater reduction in LME severity. For instance, using a higher electrode force during the pre-current may help force liquid zinc out of the weld area. A study of the effect of zinc coating thickness on LME severity would also be beneficial to understanding the mechanisms by which multiple pulse welding schedules change LME cracking. Determination of a minimum coating thickness for LME, if one exists, would assist in development of optimum welding schedules for LME resistance.

In addition, although the crack index analysis method is able to effectively predict the loss in tensile lap shear strength, there are still opportunities for further study on the relationship between cracking and weld strength. The largest loss in strength observed in this thesis work was approximately 43%. The loss in strength obviously cannot exceed 100%, meaning that at some point the linear relationship between crack index and strength loss must break down. Further study is required to determine the limits of the crack index analysis. Also, the crack index was applied only to tensile lap shear testing. A study should be conducted to determine if the crack index can also predict cross tension strength.

References

[1] S. Petit, World Vehicle Population Rose 4.6% in 2016, WardsAuto. (2017). http://subscribers.wardsintelligence.com/analysis/world-vehicle-population-rose-46-2016.

[2] Intergovernmental Panel on Climate Change, Climate Change 2014: Synthesis Report. Contribution of Working Groups I, II and III to the Fifth Assessment Report of the Intergovernmental Panel on Climate Change, Geneva, 2014. doi:10.1046/j.1365-2559.2002.1340a.x.

[3] M. McNutt, Climate change impacts, Science (80-.). 341 (2013) 435. doi:10.1126/science.1243256.

[4] F. Creutzig, P. Jochem, O.Y. Edelenbosch, L. Mattauch, D.P. van Vuuren, D. McCollum, J. Minx, Transport: A roadblock to climate change mitigation?, Science. 350 (2015) 911–2. doi:10.1126/science.aac8033.

[5] US DOE, Energy, Materials and Vehicle Weight Reduction, (2011) 30.

[6] A.I. Taub, A.A. Luo, Advanced lightweight materials and manufacturing processes for automotive applications, MRS Bull. 40 (2015) 1045–1053. doi:10.1557/mrs.2015.268.

[7] R. Kuziak, R. Kawalla, S. Waengler, Advanced high strength steels for automotive industry, Arch. Civ. Mech. Eng. 8 (2008) 103–117. doi:10.3989/revmetalm.1158.

[8] N. Baluch, Z. Mohamed Udin, C. Sobry Abdullah, Advanced High Strength Steel in Auto Industry: an Overview, Eng. Appl. Sci. Res. 4 (2014) 686–689. http://www.etasr.com/index.php/ETASR/article/view/444/265.

[9] H. Zhang, J. Senkara, Electrothermal Processes of Welding, in: Resist. Weld. Fundam. Appl., CRC Press, Boca Raton, 2006: pp. 19–57. doi:10.1017/CBO9781107415324.004.

[10] R. Ashiri, M.A. Haque, C.W. Ji, M. Shamanian, H.R. Salimijazi, Y. Do Park, Supercritical area and critical nugget diameter for liquid metal embrittlement of Zn-coated twining induced plasticity steels, Scr. Mater. 109 (2015) 6–10. doi:10.1016/j.scriptamat.2015.07.006.

[11] Y.G. Kim, I.J. Kim, J.S. Kim, Y. Il Chung, D.Y. Choi, Evaluation of Surface Crack in Resistance Spot Welds of Zn-Coated Steel, Japan Inst. Met. Mater. 55 (2014) 171–175. doi:10.2320/matertrans.M2013244.

[12] E. Tolf, J. Hedegård, A. Melander, Surface breaking cracks in resistance spot welds of dual phase steels with electrogalvanised and hot dip zinc coating, Sci. Technol. Weld. Join. 18 (2013) 25–31. doi:10.1179/1362171812Y.0000000068.

[13] D.-Y. Choi, A. Sharma, S.-H. Uhm, J.P. Jung, Liquid Metal Embrittlement of Resistance Spot Welded 1180 TRIP Steel: Effect of Electrode Force on Cracking Behavior, Met. Mater. Int. (2018). doi:10.1007/s12540-018-0180-x.

[14] J. Barthelmie, A. Schram, V. Wesling, Liquid Metal Embrittlement in Resistance Spot Welding and Hot Tensile Tests of Surface-refined TWIP Steels, IOP Conf. Ser. Mater. Sci. Eng. 118 (2016). doi:10.1088/1757-899X/118/1/012002.

[15] C. Beal, X. Kleber, D. Fabregue, M. Bouzekri, Embrittlement of a zinc coated high manganese TWIP steel, Mater. Sci. Eng. A. 543 (2012) 76–83. doi:10.1016/j.msea.2012.02.049.

[16] D.-Y. Choi, S.-H. Uhm, C.M. Enloe, H. Lee, G. Kim, C. Horvath, Liquid Metal Embrittlement of Resistance Spot Welded 1180TRIP Steel - Effects of Crack Geometry on Weld Mechanical Performance, Contrib. Pap. from Mater. Sci. Technol. 2017. (2017) 454–462.

[17] C. DiGiovanni, E. Biro, N. Zhou, Impact of liquid metal embrittlement cracks on resistance spot weld static strength, Sci. Technol. Weld. Join. (2018) 1–7. doi:10.1080/13621718.2018.1518363.

[18] C. DiGiovanni, X. Han, A. Powell, E. Biro, N.Y. Zhou, Experimental and Numerical Analysis of Liquid Metal Embrittlement Crack Location, J. Mater. Eng. Perform. (2019). doi:10.1007/s11665-019-04005-2.

[19] American Welding Society, American Welding Society: Test Method for Evaluating the Resistance Spot Welding Behavior of Automotive Sheet Steel Materials (AWS D 8.9M), (2012) 1–107.

[20] S. Keeler, M. Kimchi, P.J. Mooney, Advanced High-Strength Steels Application Guidelines Version 6.0, WorldAutoSteel. (2017).

[21] M. Pouranvari, S.P.H. Marashi, Critical review of automotive steels spot welding: process, structure and properties, Sci. Technol. Weld. Join. 18 (2013) 361–403. doi:10.1179/1362171813Y.0000000120.

[22] M. Takahashi, Development of High Strength Steels for Automobiles, Nippon Steel Tech. Rep. (2003) 2–7.

[23] H. Bhadeshia, R. Honeycombe, Steels - Microstructure and Properties, 4th ed., Elsevier, 2017.

[24] A. R. Marder, The metallurgy of zinc-coated steel, Prog. Mater. Sci. 45 (2000) 191–271. doi:10.1016/S0079-6425(98)00006-1.

[25] W. Warnecke, R. Bode, R. Kothe, L. Meyer, Modern Hot Dip Coated Steel Sheet - Processing, Coating Characteristics and Fabricating Properties, in: G. Krauss, D.K. Matlock (Eds.), Zinc-Based Steel Coat. Syst. Metall. Perform., The Minerals, Metals & Materials Society, Warrendale, 1990: pp. 3–18.

[26] A.R. Marder, Microstructural Characterization of Zinc Coatings, in: G. Krauss, D.K. Matlock (Eds.), Zinc-Based Steel Coat. Syst. Metall. Perform., The Minerals, Metals & Materials Society, Warrendale, 1990: pp. 55–82.

[27] N.T. Williams, J.D. Parker, Review of resistance spot welding of steel sheets - Part 1 Modelling and control of weld nugget formation, Int. Mater. Rev. 49 (2004) 45–75. doi:10.1179/095066004225010523.

[28] P.K. Mallick, Joining for Lightweight Vehicles, in: P.K. Mallick (Ed.), Mater. Des. Manuf. Light. Veh., CRC Press, Boca Raton, 2010: pp. 275–308.

[29] S. Donders, M. Brughmans, L. Hermans, N. Tzannetakis, The Effect of Spot Weld Failure on Dynamic Vehicle Performance, LMS Int. Interleuvenlaan 68. (2005) 1–13. doi:10.1088/1757-899X/10/1/012057.

[30] Y. Luo, J. Liu, H. Xu, C. Xiong, L. Liu, Regression modeling and process analysis of resistance spot welding on galvanized steel sheet, Mater. Des. 30 (2009) 2547–2555. doi:10.1016/j.matdes.2008.09.031.

[31] J.S. Hou, Resistance Spot Welding and In-Process Heat Treatment of Hot Stamped Boron Steel, University of Waterloo, Waterloo, 2016.

[32] D.W. Dickinson, J.E. Franklin, A. Stanya, Characterization of Spot Welding Behavior by Dynamic Electrical Parameter Monitoring, (1980).

[33] P. Russo Spena, M. De Maddis, G. D'Antonio, F. Lombardi, Weldability and Monitoring of Resistance Spot Welding of Q&P and TRIP Steels, Metals (Basel). 6 (2016) 270. doi:10.3390/met6110270.

[34] H. Zhang, Expulsion and Its Influence on Weld Quality, Weld. J. 78 (1999) 373s–380s.

doi:10.1243/09544054JEM858.

[35] M. Pouranvari, A. Abedi, P. Marashi, M. Goodarzi, Effect of expulsion on peak load and energy absorption of low carbon steel resistance spot welds, Sci. Technol. Weld. Join. 13 (2008) 39–43. doi:10.1179/174329307X249342.

[36] M. Pouranvari, S.P.H. Marashi, Factors affecting mechanical properties of resistance spot welds, Mater. Sci. Technol. 26 (2010) 1137–1144. doi:10.1179/174328409X459301.

[37] M. Pouranvari, H.R. Asgari, S.M. Mosavizadch, P.H. Marashi, M. Goodarzi, Effect of weld nugget size on overload failure mode of resistance spot welds, Sci. Technol. Weld. Join. 12 (2007) 217–225. doi:10.1179/174329307X164409.

[38] A. Joaquin, A.N.A. Elliott, C. Jiang, Reducing Shrinkage Voids in Resistance Spot Welds, Weld. J. 86 (2007) 24–27. doi:10.1016/j.ebiom.2015.07.037.

[39] W.L. Chuko, G.J. E, Development of Appropriate Resistance Spot Welding Practice for Transformation-Hardened Steels, Weld. J. 81 (2002) 1s–7s.

[40] J. Hou, K. Chan, N. Scotchmer, N. Zhou, A.P. Gerlich, In-Situ Tempering of Hot Stamped Martensitic Steel, Sheet Met. Weld. Conf. XVI. (2014) 1–9.

[41] T. Manzenreiter, M. Rosner, T. Kurz, G. Brugger, R. Kelsch, D. Hartmann, A. Sommer, Challenges and Advantages in Usage of Zinc-Coated, Press-Hardened Components with Tailored Properties, Berg- Und Hüttenmännische Monatshefte. 157 (2012) 97–101. doi:10.1007/s00501-012-0061-4.

[42] I.S. Hwang, M.J. Kang, D.C. Kim, Expulsion Reduction in Resistance Spot Welding by Controlling of Welding Current Waveform, Procedia Eng. 10 (2011) 2775–2781. doi:10.1016/j.proeng.2011.04.461.

[43] R. Ashiri, M. Shamanian, H.R. Salimijazi, M.A. Haque, J.H. Bae, C.W. Ji, K.G. Chin, Y. Do Park, Liquid metal embrittlement-free welds of Zn-coated twinning induced plasticity steels, Scr. Mater. 114 (2016) 41–47. doi:10.1016/j.scriptamat.2015.11.027.

[44] P. Eftekharimilani, E.M. van der Aa, M.J.M. Hermans, I.M. Richardson, Microstructural characterisation of double pulse resistance spot welded advanced high strength steel, Sci. Technol. Weld. Join. 22 (2017) 545–554. doi:10.1080/13621718.2016.1274848.

[45] P. Eftekharimilani, E.M. van der Aa, M.J.M. Hermans, I.M. Richardson, The microstructural

evolution and elemental distribution of a 3rd generation 1 GPa advanced high strength steel during double pulse resistance spot welding, Weld. World. 61 (2017) 691–701. doi:10.1007/s40194-017-0459-4.

[46] E.M. Van der Aa, M. Amirthalignham, J. Winter, D.N. Hanlon, M.J.M. Hermans, M. Rijnders, I.M. Richardson, Improved Resistance Spot Weldability of 3rd Generation AHSS for Automotive Applications, 11th Int. Semin. Numer. Anal. Weldability. (2015).

[47] C. Sawanishi, T. Ogura, K. Taniguchi, R. Ikeda, K. Oi, K. Yasuda, A. Hirose, Mechanical properties and microstructures of resistance spot welded DP980 steel joints using pulsed current pattern, Sci. Technol. Weld. Join. 19 (2014) 52–59. doi:10.1179/1362171813Y.0000000165.

[48] V.H. Baltazar Hernandez, Y. Okita, Y. Zhou, Second Pulse Current in Resistance Spot Welded TRIP Steel — Effects on the Microstructure and Mechanical Behavior, Weld. J. 91 (2012) 278–285.

[49] M.G.G. Nicholas, C.F.F. Old, Liquid metal embrittlement, J. Mater. Sci. 14 (1979) 1–18. doi:10.1007/BF01028323.

[50] C. Beal, X. Kleber, D. Fabregue, M. Bouzekri, Liquid zinc embrittlement of twinning-induced plasticity steel, Scr. Mater. 66 (2012) 1030–1033. doi:10.1016/j.scriptamat.2011.12.040.

[51] B. Joseph, F. Barbier, M. Aucouturier, Embrittlement of copper by liquid bismuth, Scr. Mater. 40 (1999) 893–897. doi:10.1016/S1359-6462(99)00030-5.

[52] B. Joseph, F. Barbier, G. Dagoury, M. Aucouturier, Rapid penetration of liquid Bi along Cu grain boundaries, Scr. Mater. 39 (1998) 775–781. doi:10.1016/S1359-6462(98)00230-9.

[53] R.C. Hugo, R.G. Hoagland, In-situ TEM observation of aluminum embrittlement by liquid gallium, Scr. Mater. 38 (1998) 523–529. doi:10.1016/S1359-6462(97)00464-8.

[54] W. Ludwig, E. Pereiro-López, D. Bellet, In situ investigation of liquid Ga penetration in Al bicrystal grain boundaries: Grain boundary wetting or liquid metal embrittlement?, Acta Mater. 53 (2005) 151–162. doi:10.1016/j.actamat.2004.09.012.

[55] C. Beal, X. Kleber, D. Fabrègue, M. Bouzekri, Embrittlement of a High Manganese TWIP Steel in the Presence of Liquid Zinc, Mater. Sci. Forum. 706–709 (2012) 2041–2046. doi:10.4028/www.scientific.net/MSF.706-709.2041.

[56] G. Jung, I.S. Woo, D.W. Suh, S.J. Kim, Liquid Zn assisted embrittlement of advanced high

strength steels with different microstructures, Met. Mater. Int. 22 (2016) 187–195. doi:10.1007/s12540-016-5579-7.

[57] C. Beal, Mechanical behaviour of a new automotive high manganese TWIP steel in the presence of liquid zinc [Dissertation], Insa Lyon. (2012).

[58] H. Ichinose, C. Oouchi, The Transition Dependence of the Ductile-Brittle Temperature of Aluminium in Liquid Metals, Trans. Japan Inst. Met. 9 (1968) 41–47.

[59] W.M. Robertson, Embrittlement of titanium by liquid cadmium, Metall. Trans. 1 (1970) 2607–2613. doi:10.1007/BF03038392.

[60] W. Rostoker, J.M. McCaughey, H. Markus, Mechanism of Liquid Metal Embrittlement, in: Embrittlement by Liq. Met., Reinhold Publishing Corporation, New York, 1960: pp. 129–159.

[61] M.H. Kamdar, The Occurrence of Liquid-Metal Embrittlement, Phys. Status Solidi. 4 (1971) 225–233. doi:10.1002/pssa.2210040123.

[62] E.D. Shchukin, N. V Pertsov, Y. V Goryunov, On the Variation of Mechanical Properties, Structure, and Electrical Conductivity of Single Crystals Under the Influence of a Strong Adsorption-Active Medium, Sov. Phys. - Crystallogr. 4 (1960) 840–850.

[63] J. Mendala, Liquid metal embrittlement of steel with galvanized coatings, IOP Conf. Ser. Mater. Sci. Eng. 35 (2012). doi:10.1088/1757-899X/35/1/012002.

[64] L. Cho, H. Kang, C. Lee, B.C. De Cooman, Microstructure of liquid metal embrittlement cracks on Zn-coated 22MnB5 press-hardened steel, Scr. Mater. 90 (2014) 25–28. doi:10.1016/j.scriptamat.2014.07.008.

[65] C.W. Lee, D.W. Fan, I.R. Sohn, S.J. Lee, B.C. De Cooman, Liquid-metal-induced embrittlement of Zn-coated hot stamping steel, Metall. Mater. Trans. A Phys. Metall. Mater. Sci. 43 (2012) 5122–5127. doi:10.1007/s11661-012-1316-0.

[66] C.W. Lee, W.S. Choi, L. Cho, Y.R. Cho, B.C. De Cooman, Liquid-Metal-Induced Embrittlement Related Microcrack Propagation on Zn-coated Press Hardening Steel, ISIJ Int. 55 (2015) 264–271. doi:10.2355/isijinternational.55.264.

[67] D.R. Sigler, J.G. Schroth, W. Yang, X.Q. Gayden, C. Jiang, Y. Sang, P.J. Morin, Observations of Liquid Metal-Assisted Cracking in Resistance Spot Welds of Zinc-Coated Advanced High-

Strength Steels, Proc. Sheet Met. Weld. Conf. XIII. (2008) 1–17.

[68] H. Kang, L. Cho, C. Lee, B.C. De Cooman, Zn Penetration in Liquid Metal Embrittled TWIP Steel, Metall. Mater. Trans. A Phys. Metall. Mater. Sci. 47 (2016) 2885–2905. doi:10.1007/s11661-016-3475-x.

[69] D. Bhattacharya, Liquid metal embrittlement during resistance spot welding of Zn-coated high-strength steels, Mater. Sci. Technol. 0 (2018) 1–21. doi:10.1080/02670836.2018.1461595.

[70] E. Biro, C. Jiang, J. Hunt, LME and Hot Cracking Sensitivity of AHSS during Gas Metal Arc Welding and Brazing, Sheet Met. Weld. Conf. XIV. (2010) 1–13. http://www.awsdetroit.org/smwc.html.

[71] N.S. Stoloff, T.L. Johnston, Crack propagation in a liquid metal environment, Acta Metall. 11 (1963) 251–256. doi:10.1016/0001-6160(63)90180-9.

[72] A.R.C. Westwood, M.H. Kamdar, Concerning liquid metal embrittlement, particularly of zinc monocrystals by mercury, Philos. Mag. 8 (1963) 787–804. doi:10.1080/14786436308213836.

[73] W. Robertson, Propagation of a crack filled wih liquid metal, Trans. Metall. Soc. AIME. 236 (1966) 1478–1482.

[74] E.E. Glickman, Dissolution condensation mechanism of stress corrosion cracking in liquid metals: Driving force and crack kinetics, Metall. Mater. Trans. A Phys. Metall. Mater. Sci. 42 (2011) 250–266. doi:10.1007/s11661-010-0429-6.

[75] S.P. Lynch, Environmentally assisted cracking: Overview of evidence for an adsorption-induced localised-slip process, Acta Metall. 36 (1988) 2639–2661. doi:10.1016/0001-6160(88)90113-7.

[76] V. V. Popovich, Mechanisms of liquid-metal embrittlement, Sov. Mater. Sci. 15 (1980) 438–445. doi:10.1007/BF00729232.

[77] P. Gordon, H.H. An, The mechanisms of crack initiation and crack propagation in metal-induced embrittlement of metals, Metall. Trans. A. 13 (1982) 457–472. doi:10.1007/BF02643354.

[78] M.A. Krishtal, The Formation of Dislocations in Metals on Diffusion of SUrface-Active Substances in Connection with the Effect of Adsorption Embrittlement, Sov. Phys. - Dokl. 15 (1970) 614–617.

[79] L. Klinger, E. Rabkin, Theory of the Kirkendall effect during grain boundary interdiffusion, Acta

Mater. 59 (2011) 1389–1399. doi:10.1016/j.actamat.2010.10.070.

[80] D.-Y. Choi, A. Sharma, J.P. Jung, Parametric Study for Liquid Metal Embrittlement in Resistance Spot Welds of Galvanized TRIP Steel, Sheet Met. Weld. Conf. XVIII. (2018) 1–9.

[81] J. Frei, M. Rethmeier, Susceptibility of electrolytically galvanized dual-phase steel sheets to liquid metal embrittlement during resistance spot welding, Weld. World. 62 (2018) 1031–1037. doi:10.1007/s40194-018-0619-1.

[82] Ľ. Kaščák, E. Spišák, Evaluation of the Influence of the Welding Current on the Surface Quality of Spot Welds, (2016) 32–37.

[83] Y. Benlatreche, H. Ghassemi-Armaki, M. Duchet, T. Dupuy, D. Cornette, G. Carollo, P. Dietsch, Spot-Weld Integrity of Zn-coated 3rd Gen. Advanced High Strength Steels in Presence of LME, Int. Automot. Body Congr. (2017).

[84] C. Jiang, A.K. Thompson, M.F. Shi, S. Agashe, J. Zhang, H. Zhang, Liquid Metal Embrittlement in Resistance Spot Welds of AHSS Steels, AWS Prof. Progr. (2003).

[85] H. Gaul, G. Weber, M. Rethmeier, Influence of HAZ cracks on fatigue resistance of resistance spot welded joints made of advanced high strength steels, Sci. Technol. Weld. Join. 16 (2011) 440–445. doi:10.1179/1362171810Y.0000000031.

[86] D.C. Saha, I. Chang, Y.-D. Park, Heat-affected zone liquation crack on resistance spot welded TWIP steels, Mater. Charact. 93 (2014) 40–51. doi:10.1016/j.matchar.2014.03.016.

[87] B. Yan, H. Zhu, S. Lalam, S. Baczkowski, T. Coon, Spot weld fatigue of dual phase steels, SAE Tech. Pap. (2004). doi:10.4271/2004-01-0511.

[88] E. Wintjes, A. Macwan, E. Biro, Y.N. Zhou, Effect of Multi-Pulse Welding on Lme Severity in RSW Joints, Sheet Met. Weld. Conf. XVIII. (2018).

[89] M.H. Razmpoosh, A. Macwan, E. Biro, D.L. Chen, Y. Peng, F. Goodwin, Y. Zhou, Liquid metal embrittlement in laser beam welding of Zn-coated 22MnB5 steel, Mater. Des. 155 (2018) 375–383. doi:10.1016/j.matdes.2018.05.065.

[90] E. Wintjes, C. DiGiovanni, L. He, E. Biro, Y. Zhou, Quantifying the Link Between Crack Distribution and Resistance Spot Weld Strength Reduction in Liquid Metal Embrittlement Susceptible Steels, Weld. Word. (2019).

[91] J.L. Devore, Continuous Random Variables and Probability Distributions, in: Probab. Stat. Eng. Sci., 5th ed., Brooks/Cole, Duxbury Press, 2000: pp. 143–200.

[92] P.W. Hovey, J. Knopp, Estimating Flaw Size Distributions From Service Inspection Results, 2006.

[93] S.R. Ignatovich, V.S. Krasnopol'skii, Probabilistic Distribution of Crack Length in the Case of Multiple Fracture, Strength Mater. 49 (2017) 760–768. doi:10.1007/s11223-018-9921-9.

[94] H. Itagaki, T. Ishizuka, Huang Pei Yan, Experimental estimation of the probability distribution of fatigue crack growth lives, Probabilistic Eng. Mech. 8 (1993) 25–34. doi:10.1016/j.gie.2018.04.2360.

[95] B.C. De Cooman, W. Jung, K.R. Jo, D.H. Sulistiyo, L. Cho, Liquid metal embrittlement of advanced high strength steel, Proc. Galvatech 2017. (2017) 790–795.

[96] J.K.W. Choi, N.Y. Zhou, A.P. Gerlich, Interpreting Dynamic Resistance To Monitor Shunting and Edge Proximity, Sheet Met. Weld. Conf. XVIII. (2018) 1–11.

[97] M. Zhou, S. Hu, H. Zhang, Critical specimen sizes for tensile-shear testing of steel sheets, Weld. J. (1999) 305–313. http://aws.org/wj/supplement/sept99/ZHOU.pdf.

[98] J.R. Taylor, An Introduction to Error Analysis: The Study of Uncertainties in Physical Measurements, 2nd ed., University Science Books, Sausalito, CA, 1997.

[99] B. Efron, Bootstrap Methods: Another Look at the Jackknife, Ann. Stat. 7 (1979) 1–26. doi:10.1214/aos/1176344552.

[100] D.C. Montgomery, Design and Analysis of Experiments, 9th ed., John Wiley & Sons Inc., Hoboken, NJ, 2017.

[101] C. DiGiovanni, S. Bag, C. Mehling, K.W. Choi, A. Macwan, E. Biro, N.Y. Zhou, Reduction of Liquid Metal Embrittlement Using Weld Current Ramping, IIW Comm. III Intermed. Meet. III-1908-1 (2019).

Appendix A

MATLAB Implementation of the Bootstrap Method for Calculating Standard Deviation of 95th Percentile Crack Length

```
function s = bootstrap95 (x, n, B)
% calculate standard deviation using bootstrap method
% x = vector of measurements
% n = bootstrap sample size
% B = number of bootstrap samples

per=zeros(1,B); %initialize vector of 95th percentile calculations

for i=1:B

    r=randi(length(x),1,n);  %generate  n  random  integers  between  1  and
length(x)

    z=x(r); %select measurement in positions r in the x vector

    per(i)=prctile(z,95); %calculate 95th percentile for bootstrap sample

end

s=std(per); %calculate standard deviation of 95th percentile measurements

end
```

Appendix B

ANOVA Tables for Linear Regression Analysis

Table B.1 ANOVA for linear regression of strength loss vs. mean crack length.

Source	DF	Sum of Squares	Mean Square	F value
Model	1	234.86755	234.86755	1.54196
Error	9	1370.85704	152.31745	
Total	10	1605.72459		

Table B.2 ANOVA for linear regression of strength loss vs. number of cracks per weld.

Source	DF	Sum of Squares	Mean Square	F value
Model	1	1143.24105	1143.24105	22.24764
Error	9	462.48354	51.38706	
Total	10	1605.72459		

Table B. 3 ANOVA for linear regression of strength loss vs. 95th percentile crack length.

Source	DF	Sum of Squares	Mean Square	F value
Model	1	183.98972	183.98972	1.16471
Error	9	1421.73487	157.97054	
Total	10	1605.72459		

Table B.4 ANOVA for linear regression of strength loss vs. lognormal mean.

Source	DF	Sum of Squares	Mean Square	F value
Model	1	210.34454	210.34454	1.35669
Error	9	1395.38005	155.04223	
Total	10	1605.72459		

Table B.5 ANOVA for linear regression of strength loss vs. lognormal median.

Source	DF	Sum of Squares	Mean Square	F value
Model	1	451.70604	451.70604	3.52278
Error	9	1154.01854	128.22428	
Total	10	1605.72459		

Table B.6 ANOVA for linear regression of strength loss vs. crack index.

Source	DF	Sum of Squares	Mean Square	F value
Model	1	1441.88758	1441.88758	79.2067
Error	9	163.837	18.20411	
Total	10	1605.72459		

Table B.7 ANOVA for linear regression of strength loss vs. crack index with normal median.

Source	DF	Sum of Squares	Mean Square	F value
Model	1	1414.51706	1414.51706	66.58029
Error	9	191.20753	21.24528	
Total	10	1605.72459		